Numerical Simulation of Blast Interaction with the Human Body:

Primary Blast Brain Injury Prediction

By

Tyler Haladuick

A thesis
presented to the University of Waterloo
in fulfillment of the
thesis requirement for the degree of
Master of Applied Science
in
Mechanical Engineering

Waterloo, Ontario, Canada, 2014

Authors Declaration

I hereby declare that I am the sole author of this thesis. This is a true copy of the thesis, including any required final revisions, as accepted by my examiners.

I understand that this thesis may be made electronically available to the public.

Abstract

In Operations Enduring Freedom and Iraqi Freedom, explosions accounted for 81% of all injuries; this is a higher casualty percentage than in any previous wars. Blast wave overpressure has recently been associated with varying levels of traumatic brain injury in soldiers exposed to blast loading. Presently, the injury mechanism behind primary blast brain injury is not well understood due to the complex interactions between the blast wave and the human body. Despite these limitations in the understanding of head injury thresholds, head kinematics are often used to predict the overall potential for head injury. The purpose of this study was to investigate head kinematics, and predict injury from a range of simulated blast loads at varying standoff distances and differing heights of bursts.

The validated Generator of body data multi-body human surrogate model allows for numerical kinematic data simulation in explicit finite element method fluid structure interaction blast modeling. Two finite element methods were investigated to simulate blast interaction with humans, an enhanced blast uncoupled method, and an Arbitrary Lagrangian Eularian fully coupled method. The enhanced blast method defines an air blast function through the application of a blast pressure wave, including ground reflections, based on the explosives relative location to a target; the pressures curves are based on the Convention Weapons databases. LBE model is efficient for parametric numerical studies of blast interaction where the target response is the only necessary result. The ALE model, unlike classical Lagrangian methods, has a fixed finite element mesh that allows material to flow through it; this enables simulation of large deformation problems such as blast in an air medium and its subsequent interaction with structures. The ALE model should be used when research into a specific blast

scenario is of interest, since this method is more computationally expensive. The ALE method can evaluate a blast scenario in more detail including: explosive detonation, blast wave development and propagation, near-field fireball effects, blast wave reflection, as well as 3D blast wave interaction, reflection and refraction with a target.

Both approaches were validated against experimental blast tests performed by Defense Research and Development Valcartier and ConWep databases for peak pressure, arrival time, impulse, and curve shape. The models were in good agreement with one another and follow the experimental data trend showing an exponential reduction in peak acceleration with increasing standoff distance until the Mach stem effect reached head height. The Mach stem phenomenon is a shock front formed by the merging of the incident and reflected shock waves; it increases the applied peak pressure and duration of a blast wave thus expanding the potential head injury zone surrounding a raised explosive. The enhanced blast model was in good agreement with experimental data in the near-field, and mid-field; however, overestimated the peak acceleration, and head injury criteria values in the far-field due to an over predicted pressure impulse force. The ALE model also over predicted the response based on the head injury criteria at an increased standoff distance due to smearing of the blast wave over several finite elements leading to an increased duration loading.

According to the Abbreviated Injury Scale, the models predicted a maximal level 6 injury for all explosive sizes in the near-field, with a rapid acceleration of the head over approximately 1 ms. There is a drastic exponential reduction in the insult force and potential injury received with increasing standoff distance outside of the near-field region of an explosive charge.

Acknowledgements

First most I would like to thank my advisor Duane Cronin for his tireless help and guidance in this study; Duane was the professor who piqued my interest in Biomechanics, the excitement in which he regards his research made me re-evaluate my options leaving my undergrad and I am indebted to the well-honed knowledge that he was able to pass along.

The study would not have been possible without the help supplied by Defense Research and Development Valcartier, Med-Eng, and the National Sciences and Engineering Research Council of Canada. Specifically I would like to thank Amal Bouamoul, Jean Philippe Dionne, and Simon Ouellet for their assistance in this study, and for supporting this research at the University of Waterloo.

I would like to thank my family, for always encouraging me to pursue and excel in higher education. Thank you to my parents, Mitchell and Sharon, for pushing me to be a better person and always being there when I needed, my brother, Shane, for leading by example, and my little sister, Janna, for always believing in me. Finally to my wonderful wife, Kels without your love and support over the last 9 years who knows where I would be; may you always inspire me.

Table of Contents

Authors Declaration ii

Abstract iii

Acknowledgements v

Table of Contents vi

List of Figures ix

List of Tables xii

Abbreviations xiii

Nomenclature xiv

1 Introduction 1

2 Background: Blast Wave Physics and Explosive Loading on Structures 5

2.1 Shock Waves 5

2.2 Shock Tube Physics 8

2.3 Blast Waves 12

2.4 Cylindrical vs. Spherical Charge Shapes 19

2.5 Reflected Shock Waves 20

2.5.1 Normal Reflection 21

2.5.2 Oblique Reflection 22

2.5.3 Mach Stem Reflection 22

2.6 Blast Wave Interaction with Surrounding Structures 25

2.7 Improvised Explosive Device Characteristics 28

3 Background: Human Head Anatomy and Brain Injury 30

3.1 Overview and History 30

3.2 Anatomy of the Human Head 34

3.2.1 The Skull 35

3.2.2 The Brain 36
3.3 Head Injury 40
3.4 Traumatic Brain Injury from Primary Blast Exposure 42
3.5 Primary Blast Head Injury Metrics 44
3.5.1 Head Injury Criterion (HIC) 45
3.5.2 HIC Value with Expanded Prasad/Mertz Injury Probability Curves 46
3.5.3 Peak Incident Pressure vs Probability of Fatality 48
3.5.4 Dynamic Intracranial Pressure Threshold 51
4 Background: Explicit Finite Element Modelling Applied to Blast 52
4.1 Explicit Finite Element Modelling 53
4.2 Arbitrary Lagrangian Eularian Formulation 55
4.2.1 Hydrostatic Locking in Tetrahedral Meshes 57
4.3 Validation and Verification of Finite Element Models 58
4.3.1 Verifying Mesh Convergence 58
4.4 Anthropomorphic Test Dummies for Blast Loading and Their FEM Counterparts 61
5 Modelling Blast Events and Interaction with the Human Body 66
5.1 Enhanced Blast Uncoupled Method 67
5.2 Coupled ALE Modelling of an Explosive 69
5.2.1 Shock Tube Model 70
5.2.2 Spherical Mesh Geometry Development 77
5.2.3 Cylindrical Mesh Development 83
5.2.4 Important ALE Model Parameters 85
6 Results 87
6.1 Analytical Pressure Calculations 87

6.2 Defense Research and Development Canada Experimental Results 88
6.3 Model Validation: Static Pressure 90
6.3.1 LBE Model vs. DRDC Pressure Validation 91
6.3.2 Cylindrical ALE Model vs. DRDC Pressure Validation 93
6.3.3 Spherical Charge Shape Incident Pressure Scaled to Cylindrical Charge Shape 95
6.3.4 Spherical ALE Model vs. DRDC Pressure Validation 97
6.3.5 All Models Pressure Summary 101
6.3.6 Model Scalability 103
6.4 Global Head Kinematics Comparison 104
6.4.1 Parametric Study: Effect of Blast Load on Head Kinematics 107
6.4.2 Acceleration Results Spherical ALE Model Interaction with GEBOD 109
6.5 Head Injury Criteria 113
6.5.1 LBE Model HIC Results 114
6.5.2 HIC Comparison: Experimental vs. Spherical ALE Model and LBE Model 115
6.6 Extended Prasad Mertz Curves 116
6.6.1 LBE Average AIS Injury Level 117
6.6.2 Experimental vs. LBE and Spherical ALE Probability MAIS and Average AIS 119
7 Discussion 121
7.1 Study Limitations 125
8 Summary and Conclusions 126
9 Recommendations for Future Work 129
References 130
Appendix A – The American Society of Mechanical Engineers (ASME) Design Process 136
Appendix B – Pressure Comparison 5 kg C4: 3.5 m, 4 m, 5 m Standoff 137

List of Figures

Figure 2-1 – Shock tube setup diagram. 9
Figure 2-2 – x-t diagram of a simple shock tube. Subscripts denote: (1) initial low pressure test gas, (2) shocked gas, (3) driver gas behind contact surface, (4) initial driver gas, and (5) test gas subjected to reflected shock front. [Bhaskaran et al., 2002; Salisbury et al., 2004] 10
Figure 2-3 – Standoff distance between an explosive charge and target [Adapted from Ouellet et al., 2012]. 14
Figure 2-4 – Friedlander Curve [Adapted from TM5-1300, 1991]. 15
Figure 2-5 – Qualitative differences in maximum distance of threat propagation [adapted from Thom et al., 2009]. 17
Figure 2-6 – Ratio of peak overpressure as a function of distance for end-initiated cylindrical vs spherical TNT charges of equivalent mass [Petes, 1986]. Throughout the domain plotted here, any particular blast record would have the appearance of being from a spherical charge although in fact that 'equivalent' charge is changing with distance. Transverse wave systems are still equilibrating the non-uniform near-field flow created by the non-central initiation and charge shape [Ritzel et al., 2011]. 20
Figure 2-7 – Air blast ground interaction, (adapted from [Baker, 1973]). 23
Figure 2-8 – Air blast and the subsequent path of the Mach stem triple point, ([Haladuick et al., 2012], adapted from [Baker 1973]). 24
Figure 2-9 – Scaled height of triple point [TM5-1300, 1991]. 24
Figure 2-10 – Pressure history versus time of target locations above and below the Mach stem triple point [Haladuick et al., 2012]. 25
Figure 2-11 – Material and geometric impedance adapted from [Meyers, 1994] 27
Figure 2-12 – Complex blast wave form inside an armoured vehicle [Richmond, 1985] 28
Figure 2-13 – IED material evolution in Afghanistan. [Flynn, 2009] 29
Figure 2-14 – The percentage of IEDs over the weight of 25 lbs has drastically increased [Flynn, 2009] 29
Figure 3-1 – Survival curves predicted for 70 kg man applicable to free-stream situations where the long axis of the body is perpindicular to the direction of propagation of the shocked wave [Bowen et al. 1968] 31
Figure 3-2 – Comparison of Incident Overpressure / Duration Blast Injury Criterion from Bowen, Bass, and Axelsson [Bass et al., 2008] 32
Figure 3-3 – Simplified Skull anatomy [Cowles, 2007] 35
Figure 3-4 – Structure of a neuron. [Creative Commons] 37
Figure 3-5 – Macrostructure of the brain. [Cheng, 2011] 38
Figure 3-6 – Protective systems of the brain displaying CSF, ventricles, and the protective meninges [National Cancer Institute, 2013]. 40

Figure 3-7 – Department of Defense (DoD) numbers for Traumatic Brain injury, worldwide totals.[DVBIC] 42
Figure 3-8 - Prasad/Mertz expanded probability curves used to determine injury probability, based on HIC value calculated from head acceleration traces. [Adapted from Dionne et al., 1997] 47
Figure 3-9 – AIS Severity vs Mean Survival Rate [Adapted from Gennarelli et al. AIS 2005]. 48
Figure 3-10 – Logistic risk functions for survival of both brain and pulmonary injuries caused by primary blast waves. The solid lines represent the risk of injury for the pressures on the x-axis. The dashed lines highlight the overpressures needed for a 50% probability of fatality. The risk function for brain injury was determined using the experimental data. The risk function for pulmonary injury was determined by applying the risk from Bass et al. 2008 with the blast parameters in this study [Rafaels et al., 2011]. 49
Figure 3-11 – Brain and pulmonary injury criteria across various overpressures and durations. The area in the lower left-hand side of the figure has a low risk of injury, and the area in the upper right-hand side of the figure has a high risk of injury. The risk of fatality from brain injuries requires higher pressures and longer durations than pulmonary injuries [Rafaels et al., 2011]. 50
Figure 4-1 – Example of a meshed sphere using hexahedral and tetrahedral geometric element types. [Panzer et al., 2012] 52
Figure 4-2 – Explicit finite element modelling problem solving steps. 54
Figure 4-3 – ALE steps (A) Original mesh, (B) After Lagrangian Time Step, (C) Advection [Adapted from Greer, 2006] 55
Figure 4-4 – Isometric advection of state variables in ALE algorithm: A) Initial configuration; B) After Lagrangian time step; C) After ALE advection and remapping [Greer, 2006] 57
Figure 4-5 – Hybrid III family [National Highway Traffic Safety Administration, 2013] 62
Figure 4-6 – BI^{2}PED Headform [Ouellet et al., 2012] 63
Figure 4-7 – The LS-Dyna GEnerator Of Body Data (GEBOD) multi-body model. 65
Figure 5-1 – LBE model initial setup with GEBOD. 69
Figure 5-2 – Initial conditions of 1 m shock tube showing the high pressure driver gas and the and low pressure driven gas for the 1D, 2D, and 3D cases of the 1cm mesh and the 2D 1.25 mm mesh. 72
Figure 5-3 – Numerical model showing shock tube shock wave (right) and expansion wave (left). 73
Figure 5-4 – Pressure vs. Distance for 1 m shock tube at time = 0.0005 s after diaphragm rupture. 73
Figure 5-5 – Pressure vs Distance for 1 m shock tube at time=0.0005 s after diaphragm rupture [Salisbury et al., 2004]. 74
Figure 5-6 – Expansion wave pressure profile at t=0.0005 s. 75

Figure 5-7 – Shock wave pressure profile at t=0.0005 s. 75
Figure 5-8 – Spherical mesh diverging from the center of mass of the explosive charge. 78
Figure 5-9 – ALE model geometry including ground mesh. 79
Figure 5-10 – Non spherically divergent mesh used to meet the ground in a planer fashion. 80
Figure 5-11 – Mesh refinement of a 5 kg C4 charge at 3.5 m and 4 m standoff (SO) distances. . 82
Figure 5-12 – Cylindrical mesh diverging from the axis of symmetry of the cylindrical charge... 84
Figure 5-13 – Full view of cylindrical 1/8th model. 84
Figure 6-1 – Experimental peak overpressure vs. distance for 5 kg C4 charge [DRDC – Valcartier] 89
Figure 6-2 – Experimental peak overpressure vs. distance for 10 kg C4 charge [DRDC – Valcartier]. 90
Figure 6-3 – Validation of LBE incident pressure at 3.5 m standoff from a 5 kg C4 charge with a 1.5 m HOB and a 1.5 m sensor height versus experimental data. 91
Figure 6-4 – Validation of LBE incident pressure at 4 m standoff from a 5 kg C4 charge with a 1.5 m HOB and a 1.5 m sensor height versus experimental data. 92
Figure 6-5 – Validation of LBE incident pressure at 5 m standoff from a 5 kg C4 charge with a 1.5 m HOB and a 1.5 m sensor height versus experimental data. 92
Figure 6-6 – Validation of Cylindrical ALE pressure with no ground reflection at 3.5 m standoff from 5 kg C4 charge, 1.5 m HOB and a 1.5 m sensor height versus experimental data. 94
Figure 6-7 – Validation of Cylindrical ALE pressure with no ground reflection at 4 m standoff from 5 kg C4 charge, 1.5 m HOB and a 1.5 m sensor height versus experimental data. 95
Figure 6-8 – Pressure ratio of a cylindrical charge over spherical charge vs. Overpressure from a spherical charge explosion [Adapted from Petes, 1986]. 96
Figure 6-9 – Shock wave pressure composition of spherical ALE model at detonation, 3.5 m, 4 m and 5 m. 98
Figure 6-10 – Validation of Spherical ALE incident pressure at 3.5 m standoff from a 5 kg C4 charge with a 1.5 m HOB and a 1.5 m sensor height versus experimental data. 99
Figure 6-11 – Validation of Spherical ALE incident pressure at 4 m standoff from a 5 kg C4 charge with a 1.5 m HOB and a 1.5 m sensor height versus experimental data. 100
Figure 6-12 – Validation of Spherical ALE incident pressure at 5 m standoff from a 5 kg C4 charge with a 1.5 m HOB and a 1.5 m sensor height versus experimental data. 100
Figure 6-13 – Peak overpressure vs. distance for 5 kg C4 charge for all models compared to DRDC Results and ConWep. 103
Figure 6-14 – Peak overpressure vs. distance for 10 kg C4 charge for LBE and Spherical ALE models compared to multiple DRDC tests and ConWep. 104
Figure 6-15 – GEBOD peak linear acceleration for LBE and Spherical ALE models against DRDC experimentally collected data at various standoff distances 106

Figure 6-16 –Example of a GEBOD acceleration trace for a 5 kg explosive with a 3.5 m standoff for the Spherical ALE and LBE models, showing the effect of filtering on the data signal..... 107
Figure 6-17 – Load Blast Enhanced parametric GEBOD study, peak acceleration vs. standoff distance for varying HOB. 108
Figure 6-18 – 3D plot of peak acceleration vs. standoff for all three charges at 1.5 m HOB. 108
Figure 6-19 – Beginning of blast shock wave interaction with the GEBOD at 3.5 m..... 110
Figure 6-20 – Finish of blast shock wave interaction with the GEBOD at 3.5 m. 111
Figure 6-21 – Blast wave interaction with GEBOD at 5 m. 112
Figure 6-22 – Spherical ALE acceleration traces for 3.5 m, 4 m and 5 m standoff from 5 kg C4 explosive at 1.5 m HOB. 113
Figure 6-23 – LBE HIC_{15} versus standoff distance, for all explosive sizes and HOB..... 114
Figure 6-24 – Experimental vs. LBE and Spherical ALE HIC_{15} comparison..... 115
Figure 6-25 – Extended Prasad/Mertz Curves with an average AIS level injury curve vs. HIC... 117
Figure 6-26 – Average AIS head acceleration injury from Load Blast Enhanced model vs. standoff distance. 118
Figure 6-27 – Average AIS head acceleration injury vs. Scaled Distance Factor ($Z = m/kg^{1/3}$). .. 119
Figure A-0-1 – Verification and Validation activities and outcome [ASME, 2007]. 136

List of Tables

Table 3-1 – Possible injuries to unprotected victims (high explosive detonation in open air) [Adapted from Wightman et al, 2001] 34
Table 3-2 – Abbreviated Injury Scale for concussive injuries including severity level and associated human injury [Gennarelli et al. AIS 2005]. 47
Table 5-1 – Material properties and mesh conditions for initial shock tube setup. 71
Table 5-2 – Mesh density and resultant shock wave smearing. 77
Table 5-3 – GCI calculation for peak pressure and arrival time..... 82
*Table 5-4 – Material properties for C4 explosive [*Dobratz, 1981*].* 86
Table 5-5 – JWL EOS coefficient values for C4 [Dobratz, 1981]..... 86
Table 6-1 – ConWep and analytical Results at different standoffs. 88
Table 6-2 – CORA quantitative cross-correlation ratings for LBE vs. DRDC experimental data. .. 93
Table 6-3 – CORA cross-correlation rations for Cylindrical ALE vs. DRDC Experimental data, incident wave only. 95
Table 6-4 – Peak Pressure comparison of spherical ALE charge with no E0 increase scaled to cylindrical charge shape vs. DRDC and ConWep. 96
Table 6-5 – CORA cross-correlation rations for Spherical ALE vs. DRDC Experimental data..... 101
Table 6-6 –Peak pressure and arrival time for models compared to DRDC and ConWep. 102
Table 6-7 – Impulse for incident wave and blast wave including Mach stem. 102
Table 6-8 – Experimental vs. LBE and spherical ALE probability of MAIS and average AIS..... 120

Abbreviations

AIS	Abbreviated Injury Scale
ALE	Arbitrary Lagrangian Eularian
ASME	American Society of Mechanical Engineers
ATDs	Anthropomorphic Test Dummies
BI^2PED	Blast-Induced Brain Injury Protection Evaluation Device
CG	Center of Gravity
ConWep	Conventional Weapons database
CSF	Cerebral Spinal Fluid
DAI	Diffuse Axonal Injury
DRDC	Defense Research and Development Canada
DVBIC	Defense and Veterans Brain Injury Center
EOS	Equation of State
FEM	Finite Element Method
FSI	Fluid Structure Interaction
GCI	Grid Convergence Index
GEBOD	Generator of Body Data multi-body model
HIC	Head Injury Criterion
HIII	Hybrid III Anthropomorphic Test Dummy
HOB	Height of Burst
IEDs	Improvised Explosive Devices
JWL	Jones Wilkons Lee Equation of State
kPa	Kilopascals
LBE	Load Blast Enhanced (Enhanced Blast Model)
MAIS	Probability percentage of Maximum Abbreviated Injury Scale
mTBI	Mild Traumatic Brain Injury
OEF	Operation Enduring Freedom (Afghanistan)
OIF	Operation Iraqi Freedom (Iraq)
Pa	Pascals
PBI	Primary Blast Injury
PMHS	Post Mortem Human Subjects
PTSD	Post-Traumatic Stress Disorder
SO	Stand Off distance
STP	Standard Temperature and Pressure
TBI	Traumatic Brain Injury
TNT	Trinitrotoluene

Nomenclature

General:

K = *Bulk Modulus*
P = *Pressure*
V = *Volume*
R = Ideal gas constant
T = Temperature
ρ = Density
γ = Heat capacity ratio C_P/C_V
C_P = Heat capacity at a constant pressure
C_V = Heat capacity at a constant volume
Z = Scaled Distance Factor
W = Mass in kg
R = Standoff distance in m
a^* = Ideal gas speed of sound
M = Mach number

Conservation Equations:

$\dot{m}$ = *Mass rate of flow*
A = *Cross sectional area*
u = *Flow velocity*
H = *Enthalpy*
e = *Internal energy*
Subscript 1 = *Flow before shock*
Subscript 2 = *Flow after shock*

Shock Tube Equations:

Subscript 1 = *Initial low pressure test gas*
Subscript 2 = *Shocked gas*
Subscript 3 = *Driver gas behind contact surface*
Subscript 4 = *Initial driver gas*
Subscript x = *Properties in expansion fan that vary with x*
u = *Local flow velocity*
x = *Distance from diaphragm*

Friedlander Curve:

P = *Static pressure at any time t*

P_{SO} = *Maximum static overpressure*

b = *Experimentally determined waveform parameter*

t_s = *Total time of the positive phase*

I_{max} = *Friedlander Curve Impulse*

Johns Wilkons Lee Equation of State:

A, B = *Linear coefficients*

R_1, R_2 and ω = *Nonlinear coefficients*

$V=v/v_0$ = The volume of detonation products / volumes of undetonated High Explosive

P = *Pressure*

E = *Detonation energy per unit volume of the high explosive*

Reflected Pressure in Air:

P_R = *Reflected peak pressure*

P_{SO} = *Pressure of incident wave*

P_0 = *Ambient pressure*

q_s = Dynamic pressure

u_s = Particle velocity behind the incident wave front

ρ_s = density behind the incident wave front

Speed of Sound in Solid Material:

a^* = *Speed of sound*

K = *Bulk modulus*

G = *Shear modulus*

E = *Young's modulus*

Stress Transmission and Reflection:

σ_I = *Amplitude of incident wave*

σ_R = *Amplitude of reflected wave*

σ_T = *Amplitude of transmitted wave*

A = *Area*

Subscript 1 = *Material 1*

Subscript 2 = *Material 2*

Pulmonary Blast Scaling:

Δt_{Scaled} = *Scaled Duration: Related positive phase duration on human*

M_{human} = *Mass human*

Δt_{animal} = *Amplitude of Transmitted wave*

M_{animal} = *Mass of exposed animal*

Head Injury Criterion:

HIC = *Head Injury Criterion: dimensionless number*

t_1, t_2 = *Initial and final times during which the HIC obtains a maximum value*

$a(t)$ = *The resultant acceleration measured at the center of gravity of the head*

Courant Condition Minimum Time Step:

Δt = *Minimum time step*

L = *Characteristic element Length*

C = *Wave speed in element medium*

ALE Advection Transport Phase:

φ = *Mass, momentum, or energy*

$\vec{x}$ = *ALE coordinate*

$\vec{c}$ = $\vec{v} - \vec{w}$: *Convective velocity*

$\vec{v}$= *Fluid velocity*

$\vec{w}$= *Mesh velocity*

$\varphi_0(x)$= *Initial condition of advection step from the solution of the Lagrangian step*

Grid Convergence Index:

p = *Order of convergence*

f_3, f_2, f_1 = *Results for coarse, medium and fine meshes respectively*

r = *The grid refinement ratio* $r = h_2/h_1$*; which, relates the two mesh sizes; for example: r = 2 when an element size is reduced by half globally from medium to fine meshes, and coarse to medium*

E_{12} = *Error of the fine mesh*

GCI_{12} = *Grid Convergence Index fine to medium*

GCI_{23} = *Grid Convergence Index medium to coarse*

$f_{h=0}$ = *Zero mesh error estimate*

Linear Polynomial Equation of State for Air:

μ= $\dfrac{\rho}{\rho_0} - 1$

E = *Specific internal energy (units of pressure)*

Coefficients $C_0 = C_1 = C_2 = C_3 = C_6 = 0 \; and \; C_4 = C_5 = \gamma - 1$

1 Introduction

In the recent Operation Enduring Freedom (OEF, Afghanistan), 1477 out of 3340 NATO fatalities were attributed to Improvised Explosive Devices (IEDs) [icasulaties.org, 2013] as of June 2013. In the OEF and Operation Iraqi Freedom conflicts explosions accounted for 81% of all injuries, this was a higher casualty percentage than any previous wars [Owens et al., 2008]. The increase in casualty percentage is attributed to the increased size and prevalence of IEDs used on the battlefield.

Symptoms of injuries from blast have been noted from as early as the Napoleonic Wars [Hinricsson, 1970]; however, large scale prolonged explosive attacks and artillery barrages were not a major aspect of warfare until World War I. During this time head injury from blast became known as shell shock: relating to a non-external head injury after an explosive incident. Recently, reports have established a link between soldiers that had been exposed to blast and symptoms of post-traumatic stress disorder (PTSD) [Cernak et al., 1999]. These PTSD studies as well as research completed by the automotive industry into closed head injuries have brought blast induced traumatic brain injury to the forefront of military medicine research.

Blast injuries attributed to overpressure (primary blast injury) were historically related to injuries of air filled organs including: pulmonary barotrauma (blast lung), tympanic membrane (eardrum) rupture, gastrointestinal tract hemorrhage [Cooper and Dudley 1997]. Recently blast overpressure impingement has been linked to varying levels of traumatic brain injury (TBI) in casualties who were exposed to blast loading [Saatman et al., 2008].

In modern conflicts there has been an increase in survivability from pulmonary injury due to more effective body armour [Wood et al., 2012], this combined with the increase in size and usage of enemy explosives, and the increased awareness in the medical field of diagnosing mild traumatic brain injury (mTBI) has caused an increase in the prevalence of primary brain injury attributed to blast. The Defense and Veterans Brain Injury Center (DVBIC) reports that 280,734 US service personnel were diagnosed with TBI between 2000 and 2013, with the majority (82.4%) of those affected suffering from mild traumatic brain injury (mTBI) [DVBIC]. Symptoms of traumatic brain injury include unconsciousness, amnesia, severe headaches, insomnia, vertigo, tinnitus, sensitivity to light and noise, memory deficits, and difficulty with decision making.

The mechanism corresponding to primary brain blast injury at present is not well understood [Gupta et al., 2013]. This difficulty stems from the inability to measure intracranial phenomena in living subjects, the high accelerations of the head experienced over very short time duration, and the complex interactions between a blast wave and the human body. Recently it is believed that mTBI may result from primary interaction with the blast wave leading to some damage or change in function at the tissue or cellular level [Schmitt et al., 2014]; however, there currently exists no injury criterion by which the extent of these injuries can be predicted.

When blast waves, which travel faster than the speed of sound in air, interact with the body the large pressure differential results in rapid accelerations of the body creating a high-frequency stress wave that propagates through tissue. Experimental models to evaluate head response and the potential for brain injury have included a variety of techniques and test species in order

to develop a reproducible model of trauma that exhibits anatomic, physiologic, and functional responses similar to those described clinically [Nahum et al., 2002]. Applying these models to blast-induced traumatic brain injury produces significant difficulties in determining the measureable parameters that are associated with a specific physical or psychological symptom as these symptoms often do not become apparent for some time following the insult. Thus explosive-related head injuries have been the subject of many previous studies; however, the mechanisms and thresholds pertaining to head injuries from blast are still under investigation.

These difficulties are prompting further research using Finite Element Method (FEM) models to determine the effect of overpressure on the kinematics of the human head, and the internal response of the brain [Haladuick et al., 2012; Singh et al., 2013; Panzer et al., 2012; Ganpule et al. 2013; Lockhart et al., 2011].

This study is part of a multi-scale modelling approach to predict head injury from blast, and is working in parallel to a study using slice models of the human head to visualize internal brain response to blast [Singh et al., 2013].

This thesis includes a literature review of the required background information to understand numerical simulation of blast interaction with the human body including: Blast Wave Physics and Explosive Loading (Chapter 2), Blast Injury and Brain Anatomy (Chapter 3), as well as Explicit Finite Element Modelling (Chapter 4). This thesis follows with an explanation of the methods used for Modelling Blast Events and Interaction with the Human Body (Chapter 5), the Results of this study (Chapter 6), Discussion of the results (Chapter 7), Conclusions (Chapter 8) and Recommendations (Chapter 9).

The purpose of this thesis was to numerically simulate blast wave interaction with the human body using a variety of methods to predict head kinematics resulting from a range of simulated blast scenarios.

2 Background: Blast Wave Physics and Explosive Loading on Structures

This background section focuses on the physics of a blast event, specifically how a blast wave is formed, and how the resulting shock wave propagates through a medium interacting with the ground and surrounding structures. It is important to understand blast dynamics when discussing human injury from blast events as the injury mechanisms of blast overpressure differ from those of other high impact scenarios. This section also details shock tube physics and the effect that an explosives shape has on the resultant blast wave.

2.1 Shock Waves

A shock wave is defined as a discontinuity in pressure, density, and temperature across a surface that is assumed to have negligible thickness. This non-linear phenomenon propagates faster than the speed of sound in the medium which it is travelling and produces a large acceleration of the material it is traveling through. [Cronin, 2012] For a shock wave to form in a material the material's bulk modulus, which is the measure of a substances resistance to uniform compression, must increase with an increase in pressure, i.e. the compressibility of the material must decrease with an increase in pressure:

Bulk Modulus

$$K = -V\frac{dP}{dV};\ must\ increase\ with\ increasing\ pressure \qquad \textit{Equation 2-1}$$

Where:

P = *Pressure*
V = *Volume*

When regarding a shock wave in an ideal gas such as air, one can use ideal gas relations on either side of the shock discontinuity, these relationships are considered isentropic in nature and thus compression or expansion of an ideal gas is a reversible adiabatic process:

Ideal gas law $$PV = nRT;\ P = \rho RT$$ *Equation 2-2*

Heat capacity ratio $$\gamma = \frac{C_P}{C_V}$$ *Equation 2-3*

Differentiation $$\frac{dP}{dV} = -\gamma \frac{P}{V}$$ *Equation 2-4*

Isentropic $$\frac{P_2}{P_1} = \left(\frac{T_2}{T_1}\right)^{\frac{\gamma}{\gamma-1}} = \left(\frac{\rho_2}{\rho_1}\right)^{\gamma} = \left(\frac{V_1}{V_2}\right)^{\gamma}$$ *Equation 2-5*

Adiabatic Bulk Modulus $$K = \gamma P$$ *Equation 2-6*

Where:

R = Ideal gas constant
T = Temperature
ρ = Density
C_P = Heat capacity at a constant pressure
C_V = Heat capacity at a constant volume

These equations represent the ideal gas equation of state (EOS), which is a constitutive relationship describing the state of matter under a given set of physical conditions. An EOS is required when calculations are to be performed if a material's compressibility is an important factor, such as in shock problems.

The speed of sound of a material is an important factor for shock wave propagation. In ideal gases the speed of sound is only dependant on temperature.

Ideal gas speed of sound $$a^* = \sqrt{\gamma RT} = \sqrt{\gamma \frac{P}{\rho}} = \sqrt{\frac{K}{\rho}}$$ *Equation 2-7*

The above isentropic ideal gas equations only apply on each side of the shock discontinuity, in order to describe the jump discontinuity Rankine-Hugoniot shock relations are used. These relations are derived from Euler conservation equations:

Conservation of mass $$\frac{\dot{m}}{A} = \rho_1 u_1 = \rho_2 u_2$$ *Equation 2-8*

Conservation of momentum $$\rho_1 u_1^2 + P_1 = \rho_2 u_2^2 + P_2$$ *Equation 2-9*

Conservation of Energy $$\frac{1}{2}u_1^2 + H_1 = \frac{1}{2}u_2^2 + H_2$$ *Equation 2-10*

Enthalpy $$H = e + RT$$ *Equation 2-11*

Where:

$\dot{m}$ = *Mass rate of flow*
A = *Cross sectional area*
u = *Flow velocity*
H = *Enthalpy*
e = *Internal energy*
Subscript 1 = *Flow before shock*
Subscript 2 = *Flow after shock*

For an ideal gas with a constant $\gamma = \frac{C_P}{C_V}$, the Rankine-Hugoniot conditions are as follows:

$$\frac{P_2}{P_1} = \frac{1 - \left(\frac{\gamma - 1}{\gamma + 1}\right)\frac{\rho_1}{\rho_2}}{\frac{\rho_1}{\rho_2} - \frac{\gamma - 1}{\gamma + 1}}$$ *Equation 2-12*

Rankine - Hugoniot equations

$$\frac{\rho_2}{\rho_1} = \frac{\left(\frac{\gamma - 1}{\gamma + 1}\right) + \frac{P_2}{P_1}}{\left(\frac{\gamma - 1}{\gamma + 1}\right)\frac{P_2}{P_1} + 1} = \frac{u_1}{u_2}$$ *Equation 2-13*

$$e_2 - e_1 = \frac{P_1 + P_2}{2}\left(\frac{1}{\rho_1} - \frac{1}{\rho_2}\right) \qquad \textit{Equation 2-14}$$

The Mach number of a gas flow is the ratio of the velocity of a flow to the local speed of sound in the gas:

Mach number $$M = \frac{u}{a^*} \qquad \textit{Equation 2-15}$$

2.2 Shock Tube Physics

Shock tubes are used in laboratory testing as a safe and economic method of simulating blast environment. The input variables can be carefully controlled to give desired results in a laboratory setting when applying a shock to a target material or animal. A limitation of shock tubes is that they lack the ability to simulate temperature, shrapnel, fireball or other explosive effects that may be of interest. In the course of this thesis, the analytical calculations describing a shock tubes material were used to validate 1D, 2D, and 3D Arbitrary Lagrangian Eularian mesh sizing and control parameters.

A shock tube is long tube of either circular or rectangular cross section with a diaphragm separating two sides of the tube filled with gases at different states of temperature and pressure. One side of the tube is filled with a test gas often at atmospheric or low pressure conditions, and the other side is filled with a high pressure driver gas (Figure 2-1). The shock tube is usually several meters long with a target set in place in the low pressure gas that should

only take up approximately ten percent of the cross-sectional area.

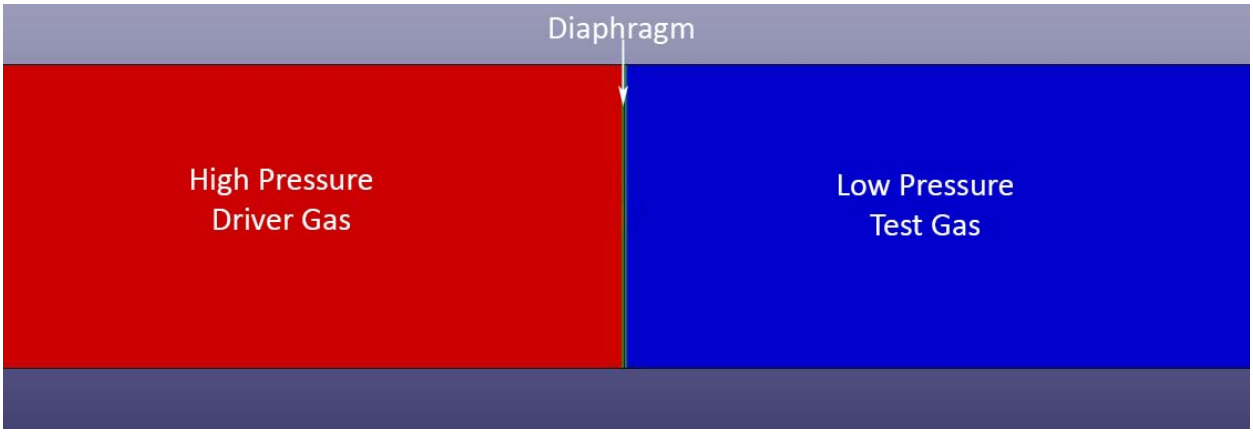

Figure 2-1 – Shock tube setup diagram.

When the diaphragm is intentionally ruptured, the high pressure compressed driver gas flows into the test gas. A shock wave is produced and propagated through the low pressure gas as a rarefaction or release wave travels in the opposite direction through the driver gas. The pressure and temperature behind the shock wave increase sharply, but the rarefaction wave leads to a more gradual change in the driver pressure through the high pressure gas being expanded by the expansion fan (Figure 2-2).

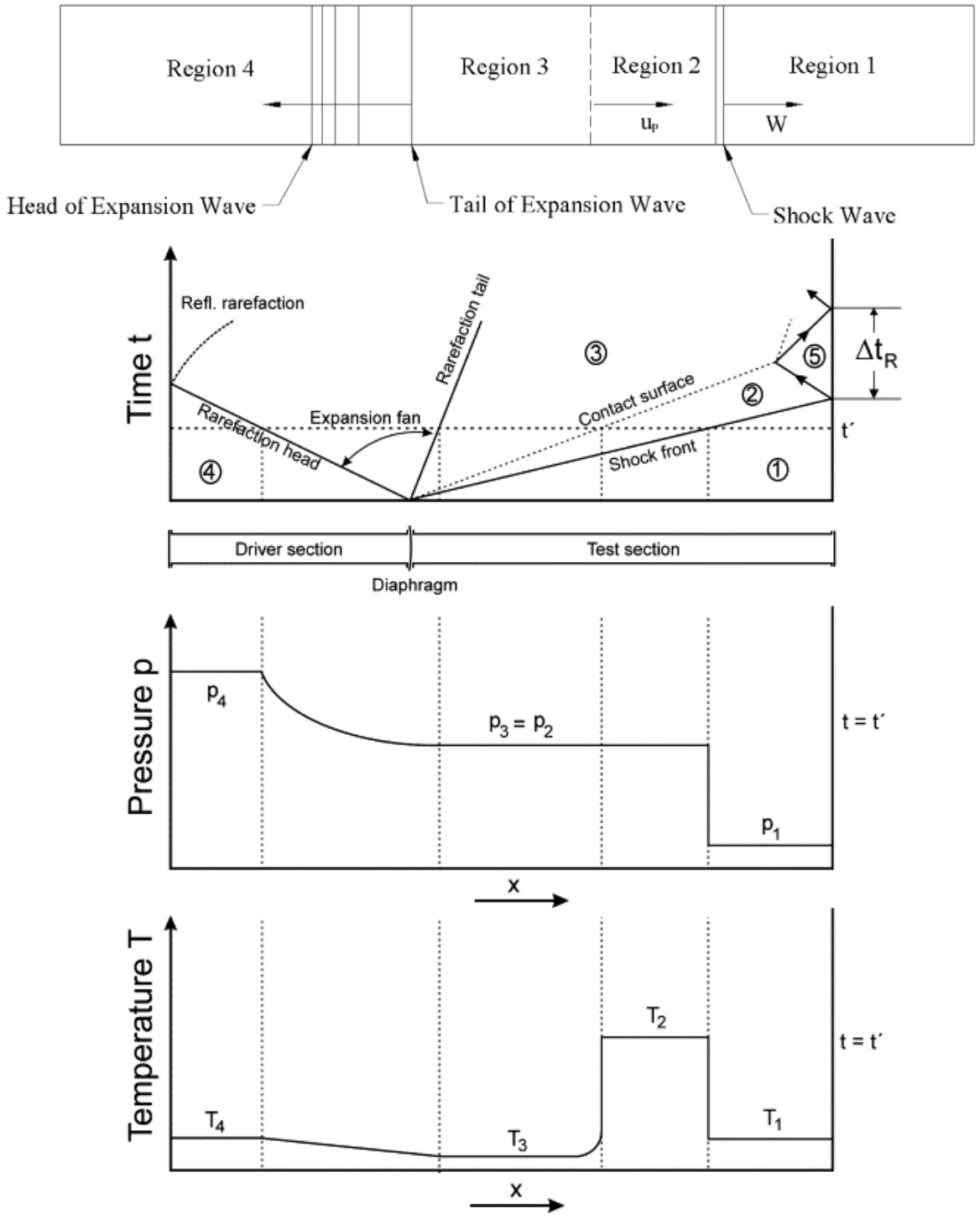

Figure 2-2 – x-t diagram of a simple shock tube. Subscripts denote: (1) initial low pressure test gas, (2) shocked gas, (3) driver gas behind contact surface, (4) initial driver gas, and (5) test gas subjected to reflected shock front. [Bhaskaran et al., 2002; Salisbury et al., 2004]

To validate the numerical simulation results against experimental data analytical calculations for a shock tube must be defined and solved using the same conditions as the experimental and numerical models. Using isentropic relationships of Equation 2-2 - Equation 2-6, the following relationships can be developed [Rinku, 2013].

Incident shock strength

$$\frac{P_2}{P_1} \qquad \textit{Equation 2-16}$$

Diaphragm pressure (initial conditions)

$$\frac{P_4}{P_1} \qquad \textit{Equation 2-17}$$

$$\frac{P_4}{P_1} = \frac{P_2}{P_1}\left\{1 - \frac{(\gamma-1)\left(\frac{a^*_1}{a^*_4}\right)\left(\frac{P_2}{P_1}-1\right)}{\sqrt{2\gamma\left(2\gamma\left[2\gamma+(\gamma+1)\left(\frac{P_2}{P_1}-1\right)\right]\right)}}\right\}^{-\frac{2\gamma}{\gamma-1}} \qquad \textit{Equation 2-18}$$

Expansion fan strength

$$\frac{P_3}{P_4} = \frac{P_3}{P_1}\cdot\frac{P_1}{P_4} = \left(\frac{\rho_2}{\rho_1}\right)^{\gamma} = \frac{P_2}{P_1}\cdot\frac{P_1}{P_4} \qquad \textit{Equation 2-19}$$

From Equation 2-5

$$\frac{P_3}{P_4} = \left(\frac{T_3}{T_4}\right)^{\frac{\gamma}{\gamma-1}} = \left(\frac{\rho_3}{\rho_4}\right)^{\gamma}$$

From Equation 2-7

$$a^* = \sqrt{\gamma RT}$$

Properties within the expansion fan

$$\frac{a^*}{a^*_4} = \frac{T_x}{T_4} = \left(1 - \left(\frac{\gamma-1}{2}\right)\frac{u_x}{a^*_4}\right)^2 \qquad \textit{Equation 2-20}$$

$$\frac{P_x}{P_4} = \left(\frac{T_x}{T_4}\right)^{\frac{\gamma}{\gamma-1}} = \left[1 - \left(\frac{\gamma-1}{2}\right)\frac{u_x}{a^*_4}\right]^{\frac{2\gamma}{\gamma-1}} \qquad \textit{Equation 2-21}$$

$$\frac{\rho_x}{\rho_4} = \left[1 - \left(\frac{\gamma-1}{2}\right)\frac{u_x}{a^*_4}\right]^{\frac{2}{\gamma-1}} \qquad \textit{Equation 2-22}$$

$$x = (u_x - a)t; \frac{dx}{dt} = u_x - a \qquad \textit{Equation 2-23}$$

Flow velocity within expansion fan $$u_x = \frac{2}{1+\gamma}\left(a_4^* + \frac{x}{t}\right)$$ *Equation 2-24*

Boundaries of expansion fan $$-a_4 \leq \frac{x}{t} \leq u_3 - a_3$$ *Equation 2-25*

Continuity $$u_2 = u_3; P_2 = P_3; \rho_2 = \rho_3$$ *Equation 2-26*

Where:

Subscript 1 = *Initial low pressure test gas*
Subscript 2 = *Shocked gas*
Subscript 3 = *Driver gas behind contact surface*
Subscript 4 = *Initial driver gas*
Subscript x = *Properties in expansion fan that vary with x*
u = *Local flow velocity*
x = *Distance from diaphragm*

Using Equation 2-18 for a given diaphragm pressure $\left(\frac{P_4}{P_1}\right)$ one can calculate the incident shock strength $\left(\frac{P_2}{P_1}\right)$ for a given initial pressure ratio, and one can determine all shock properties of the shock wave propagating through the test gas. Then using Equation 2-19 the expansion fan strength can be found to determine the remaining properties of the expansion fan. The expansion fan is bounded on its rarefaction head by $-a_4$ and on its tail by a_3-u_3. The location of the shock wave in the test gas can be found by multiplying the speed of sound in the gas by the amount of time since the diaphragm burst.

2.3 Blast Waves

A blast sequence is initiated when a detonation wave is triggered by a primary explosive detonation such as Lead azide ($Pb(N_3)_2$) [Smith et al., 1994] and shocks a secondary explosive material such as Trinitrotoluene (TNT) or C4 a type of plastic explosive. This detonation wave travels through the secondary explosive faster than the speed of sound of the explosive

material, in C4 the detonation velocity is 8193 m/s [Dobratz, 1981]. This detonation wave causes a violent decomposition of the explosive material producing heat and combustion gases and is typically adiabatic over the short duration of the explosion. The rapid expansion of these gases produces a high pressure, high temperature state; when this state occurs in a medium such as air a supersonic blast wave results [Smith et al., 1994]. Some important characteristics for defining a blast wave include arrival time, positive phase duration, and peak pressure. The pressure wave from an explosive blast is defined using static, incident or side on pressure that corresponds to the pressure that would be observed in the flow field with no fluid structure interaction. When the shock wave interacts with a structure, such as the human body, the pressure is described as dynamic or reflected pressure, which includes the static pressure and the interaction of the flow field with a structure.

The standoff distance (R) is defined as the distance from the center of gravity of an explosive charge to the center of gravity of the target (Figure 2-3). The incident and reflected pressures decay exponentially with increasing standoff distance proportional to the scaled distance factor given by:

Scaled Distance Factor: $$Z = \frac{R}{W^{\frac{1}{3}}}$$ *Equation 2-27*

[Smith et al., 1994]

Where:

W = Mass in kg

R = Standoff distance in m

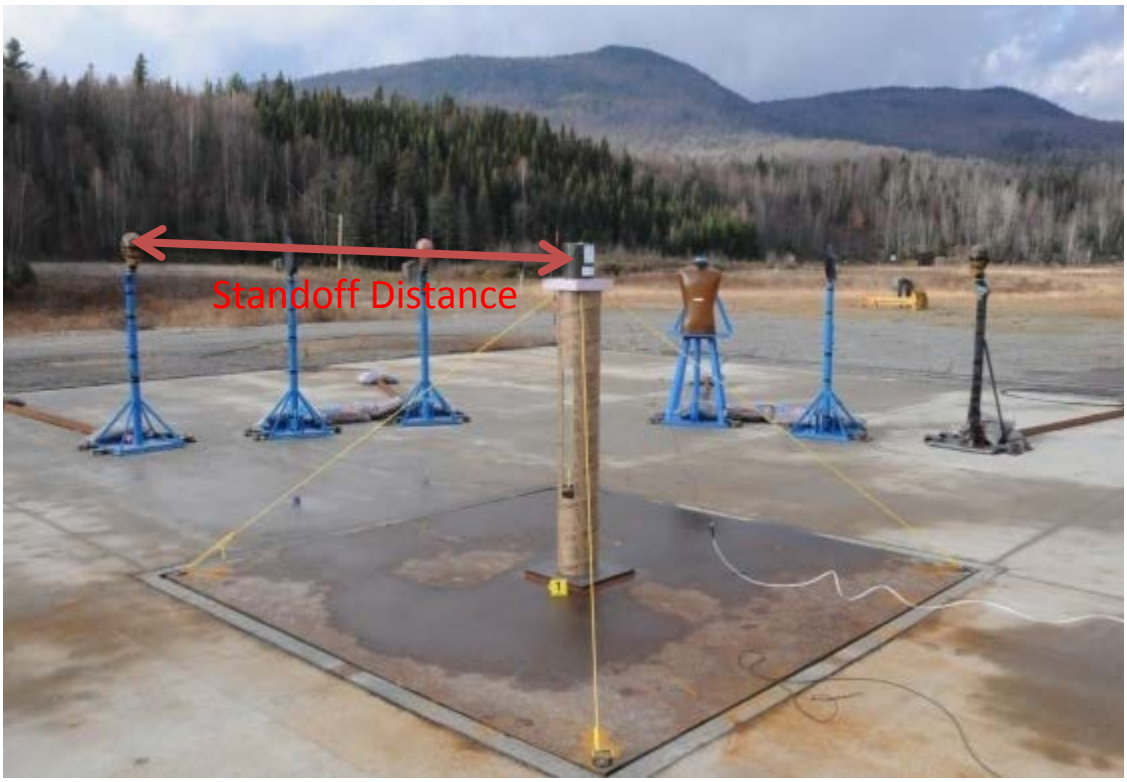

Figure 2-3 – Standoff distance between an explosive charge and target [Adapted from Ouellet et al., 2012].

After an explosive reaction from a solid explosive to high pressure, high temperature gas, the blast wave and corresponding gases move radially outwards from the detonation point producing a sharp rise or discontinuity in pressure, temperature, and density across the shock front. The gases subsequently expand and the pressure falls to atmospheric conditions. As the gases have mass the momentum of the wave front takes longer to attenuate. This momentum causes the gases to over expand and the pressure behind the blast wave to drop below atmospheric, creating a negative pressure phase that will eventually return to atmospheric pressure. In an ideal case, an explosive pressure curve follows a Friedlander Curve, (Figure 2-4), and described by the following function:

Friedlander Curve: $$P = P_{SO}\left(1 - \frac{t}{t_s}\right)e^{-\frac{bt}{t_s}}$$ *Equation 2-28*

[Smith et al., 1994]

Where:

P = *Static pressure at any time t*

P_{SO} = *Maximum static overpressure*

b = *Experimentally determined waveform parameter*

t_s = *Total time of the positive phase*

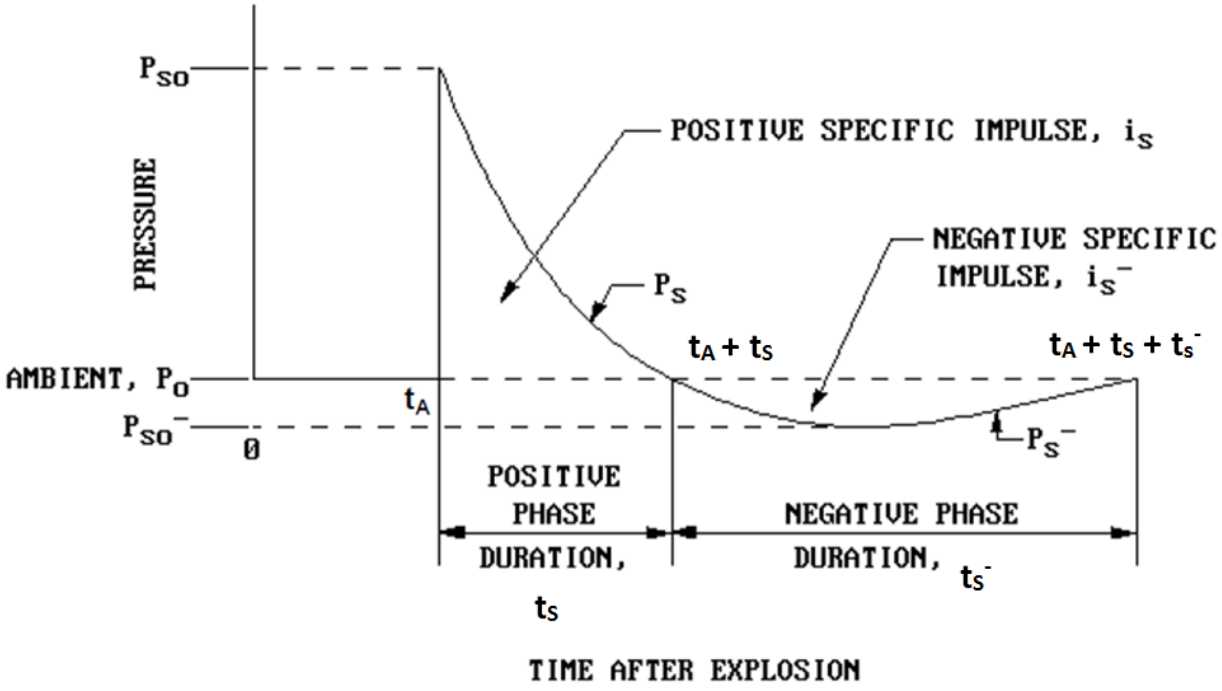

Figure 2-4 – Friedlander Curve [Adapted from TM5-1300, 1991].

The ideal impulse created by a Friedlander curve can be determined by integrating the pressure over the positive phase duration, this is seen in the above figure labeled positive specific impulse is:

Friedlander Curve Impulse: $$I_{max} = P_{SO}t_s\left[\frac{1}{b} - \frac{1}{b^2}(1 - e^{-b})\right]$$ *Equation 2-29*

[Kinney, 1962]

The positive specific impulse is the maximum impulse applied to a single standoff distance; the impulse of a blast wave will also diminish with increasing standoff.

The surroundings that are impinged upon by an explosive blast can be split into three distance regimes: near-field, mid-field, and far-field as described by Reitzel et al [Ritzel et al., 2011]:

In the near-field to an explosive blast objects are exposed to a blast overpressure greater than about 1 MPa, and are typically within the extent of the maximum fireball expansion. In the near-field assessment of target interactions must include the following conditions:

- Impingement of detonation products.
- Non-uniform wave-dynamics within the early expansion of the fireball.
- The ratio of static and dynamic pressures changes, and is not spatially constant.
- There is a large change in density and temperature across the contact surface of the fireball.

Actual Improvised Explosive Devices (IEDs) have far more complicated reactions in the near-field due to non-ideal explosive combustion, charge shape, initiation, orientation, and the variable amount of explosive energy transferred to kinetic energy through case fragmentation and expulsion.

The mid-field is defined as the zone beyond the expansion of the fireball where the static over pressures range from 1 to 10 atmospheres and still have strong non-uniform wave dynamics due to charge shape and the energy re-partitioning due to fragmentation in the flow field. In

this regime the wave follows an exponential decay; however, due to non-linear effects such as afterburning the negative phase as depicted in *Figure 2-4* may not be correctly predicted.

The far-field refers to a zone where the wave-dynamics have equilibrated to a quasi-steady spherical decay, and any irregularities or aspects of physics from the near and mid-field will be transferred to the far-field observations.

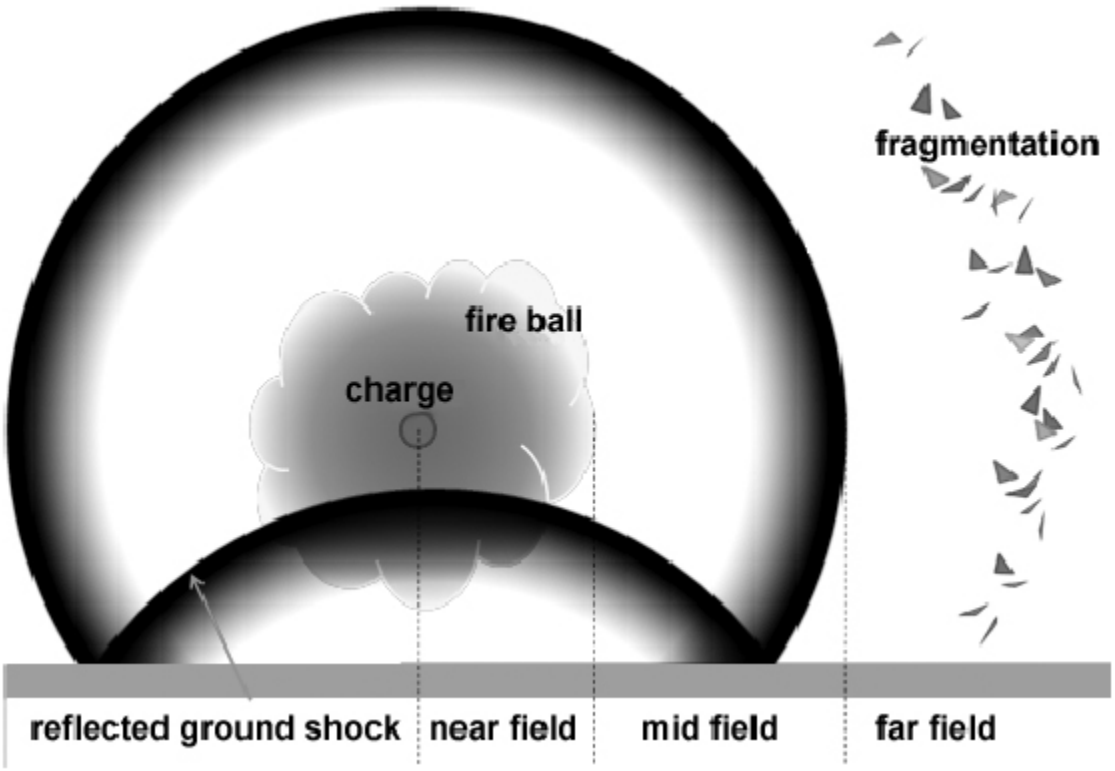

Figure 2-5 – Qualitative differences in maximum distance of threat propagation [adapted from Thom et al., 2009].

To determine the ideal maximum static over pressure of the blast wave (P_{SO} in *Figure 2-4*), the equations given by Henrych [Baker, 1973] are based on the scaled distance factor:

$$P_{SO} = \frac{14.072}{Z} + \frac{5.540}{Z^2} + \frac{0.357}{Z^3} + \frac{0.00625}{Z^3}\ bar \qquad (0.05 \leq Z < 0.3)$$

Henrych Over Pressure:

$$P_{SO} = \frac{6.194}{Z} + \frac{0.326}{Z^2} + \frac{2.132}{Z^3}\ bar \qquad (0.3 \leq Z \leq 1)$$

$$P_{SO} = \frac{0.662}{Z} + \frac{4.05}{Z^2} + \frac{3.288}{Z^3}\ bar \qquad (1 \leq Z \leq 10) \qquad \textit{Equation 2-30}$$

The accuracy of the above equations is lower for near-field blast than far field blasts due to the complex flow processes of the blast wave formation proximal to the explosive charge where there is heavy influence from the explosive gases and other effects.

The magnitude of an explosion is determined by the amount of energy released; explosives are generally evaluated by a relative rather than absolute energy metric to the amount of energy released by an explosion of TNT, which is measured to have an explosive yield based on specific energy of 4520 kJ/kg [Dobratz, 1981]. For this thesis, C4 was the explosive used in order to be validated against experimental tests carried out at Defense Research and Development Canada (DRDC), C4 has a TNT pressure equivalent factor of 1.34 [Dobratz, 1981].

The detonation products of an explosive can be defined using a Jones Wilkons Lee (JWL) EOS that relates energy, pressure and density; this EOS is used to define the characteristics of explosive materials in a computer simulation environment [Dobratz, 1981].

JWL EOS:
$$P = A\left(1 - \frac{\omega}{R_1 V}\right)e^{-R_1 V} + B\left(1 - \frac{\omega}{R_2 V}\right)e^{-R_2 V} + \frac{\omega}{V}E \qquad \textit{Equation 2-31}$$

Where:

A, B = *Linear coefficients*

R_1, R_2 and ω = *Nonlinear coefficients*

$V=v/v_0$ = The volume of detonation products / volumes of undetonated high explosive

P = *Pressure*

E = *Detonation energy per unit volume of the high explosive*

2.4 Cylindrical vs. Spherical Charge Shapes

The shape of an explosive charge can drastically change the wave-dynamics in the near-field and mid-field regimes of a blast incident. Many experiments are carried out using cylindrical charges with a scaled height to diameter ratio typical of the explosive munitions threat the researchers are interested in. Figure 2-6 shows that blast from cylindrical charges never truly converges on the results for a spherical charge of equivalent mass.

As explained by Ritzel et al., the blast wave propagating perpendicular to the axis of cylindrical shaped charge is governed by the physics of cylindrical expansion including: the decay rate behind the shock, the development of the negative phase and the secondary shock. The flat ends of the cylinder have quasi-planar flow and these two wave expansion flow-fields become bridged and then merged by ground reflections to ultimately evolve to a semi-spherical expansion [Ritzel et al., 2011]. Therefore along a particular direction the blast wave may evolve from a quasi-cylindrical to a quasi-spherical expansion and the fractional ratios, (Figure 2-6), become meaningful in describing the blast-wave flow.

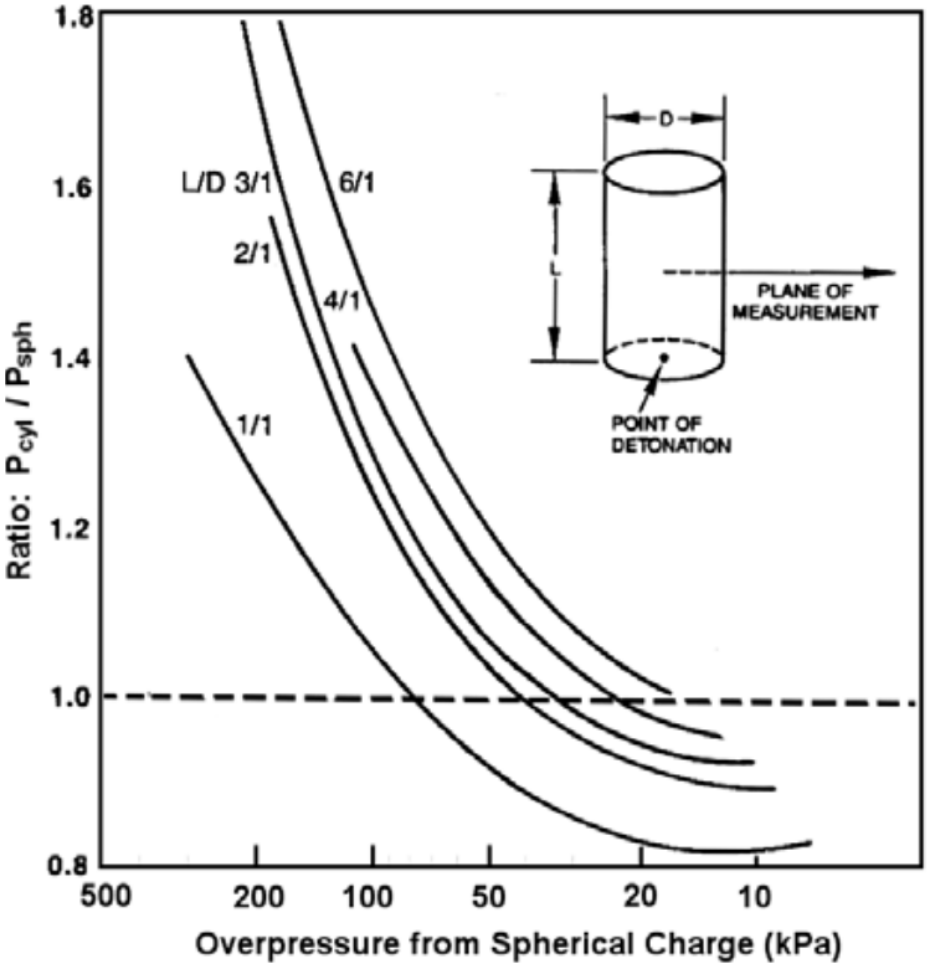

Figure 2-6 – Ratio of peak overpressure as a function of distance for end-initiated cylindrical vs spherical TNT charges of equivalent mass [Petes, 1986]. Throughout the domain plotted here, any particular blast record would have the appearance of being from a spherical charge although in fact that 'equivalent' charge is changing with distance. Transverse wave systems are still equilibrating the non-uniform near-field flow created by the non-central initiation and charge shape [Ritzel et al., 2011].

2.5 Reflected Shock Waves

When a shock encounters a solid object or a surface made of a medium denser than the medium transmitting the wave, the shock will reflect from the object or surface, and depending on its geometry and size, possibly diffract around it. There are three types of blast wave

reflection: (1) normal reflection where a shock wave impinges directly perpendicular to an unyielding surface, (2) oblique reflection where a shock encounters a surface at a small angle of incidence between the shock plane and the plane of the reflecting surface, (3) Mach stem formation where a blast wave glances off a reflected plane and rejoins the shock medium creating a triple point phenomenon.

2.5.1 Normal Reflection

When a shock wave traveling through ambient conditions impinges on an unyielding infinitely rigid wall at an angle of 0 degrees the shock is terminated nearly instantaneously. As a result the moving particles at the front of the shock wave that have impacted the wall are brought to rest and further compressed producing a reflected overpressure that is greater than the incident shocks overpressure. The fluid particles that were brought to rest now have a relative velocity to the impinging shock front of equal magnitude but opposite in direction. As a result a new shock propagates back through the medium. Although these two shocks have the same velocity, they have different characteristic properties as the reflected shock is moving through a pre-compressed medium.

For a zero degree incidence on an unyielding wall, the following equations have been developed:

Reflected Peak Pressure $$P_R = 2P_s + (\gamma + 1)q_s$$ *Equation 2-32* *[Smith et al., 1994]*

Dynamic Pressure $$q_s = \frac{1}{2}\rho_s u_s^2$$ *Equation 2-33* *[Smith et al., 1994]*

Reflected Pressure in Air $$P_R = 2P_{SO}\left[\frac{7P_0 + 4P_{SO}}{7P_0 + P_{SO}}\right]$$ *Equation 2-34*

[Smith et al., 1994]

Where:

P_R = *Reflected peak pressure*
P_{SO} = *Pressure of incident wave*
P_0 = *Ambient pressure*
q_s = Dynamic pressure
u_s = Particle velocity behind the incident wave front
ρ_s = density behind the incident wave front

Upon inspection of Equation 2-34

[Smith et al., 1994], the minimum reflected pressure when P_{SO} is much smaller than the ambient pressure, or a small explosive charge at far field distance is $P_R = 2P_{SO}$; and the max reflected pressure when P_{SO} is much larger than P_0, or a large charge at a small standoff, or near field explosion $P_R = 8P_{SO}$.

2.5.2 Oblique Reflection

Oblique reflection occurs when a blast wave encounters a surface at near head-on incidence. Up to a critical angle of incidence based on incident pressure, approximately 40^o in air, an oblique reflection will be formed. The reflection has similar characteristics to a normal reflection but a slightly lower reflection coefficient that reaches a minimum value at 40^o before the Mach Stem regime is entered.

2.5.3 Mach Stem Reflection

When an above ground blast incident wave skims off the ground with an angle of incidence greater than 40^o (Figure 2-7), it produces a reflected wave front. This reflected wave accelerates through the pre-compressed hot gases from the incident wave enabling the

reflected wave to catch and join the incident wave producing a Mach stem. The Mach stem is the shock front formed by the merging of the incident and reflected shock waves from an explosion. The moving point of intersection between the incident wave, ground reflected wave, and the Mach stem is called the triple point phenomenon.

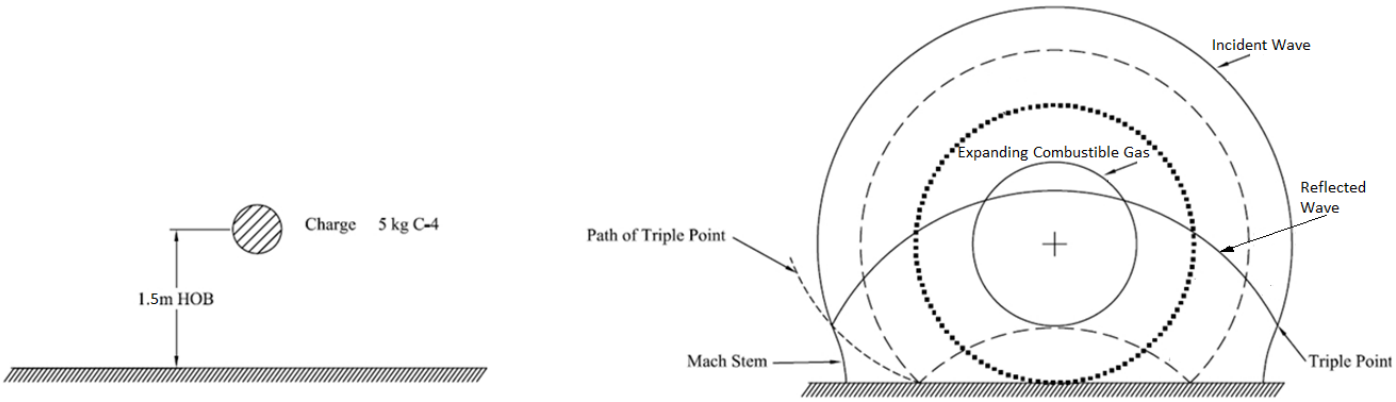

Figure 2-7 – Air blast ground interaction, (adapted from [Baker, 1973]).

The path of the triple point and the size and relative height of the Mach stem is a function of the charge size, standoff distance, and the explosive Height of Burst (HOB), (Figure 2-9). The Mach front increases the pressure observed by the target from the blast and once formed the triple point height increases with increasing standoff distance (Figure 2-8) [Baker, 1973].

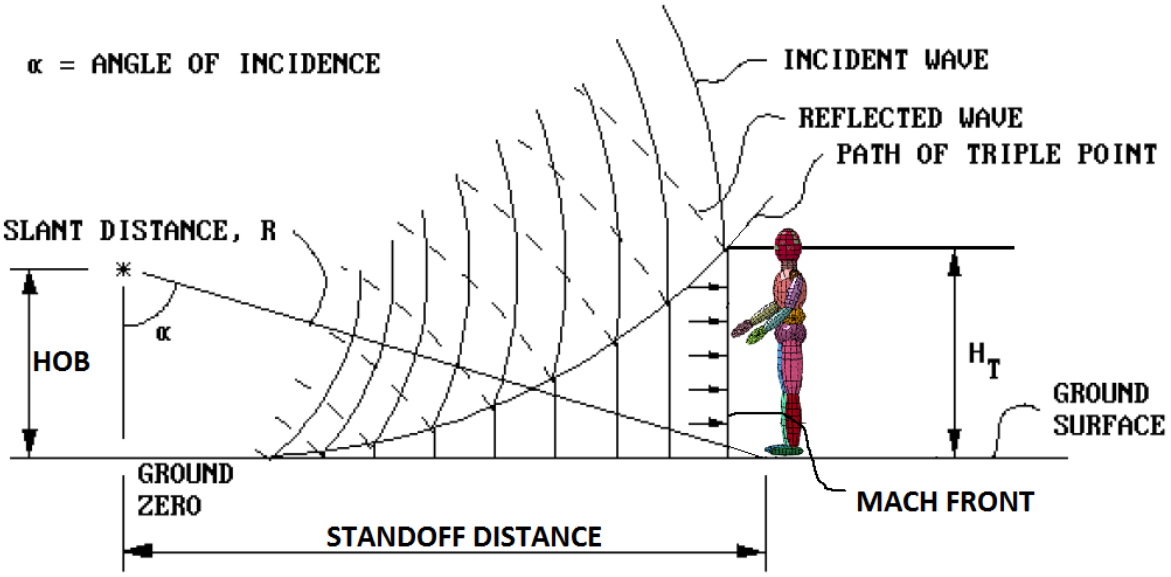

Figure 2-8 – Air blast and the subsequent path of the Mach stem triple point, ([Haladuick et al., 2012], adapted from [Baker 1973]).

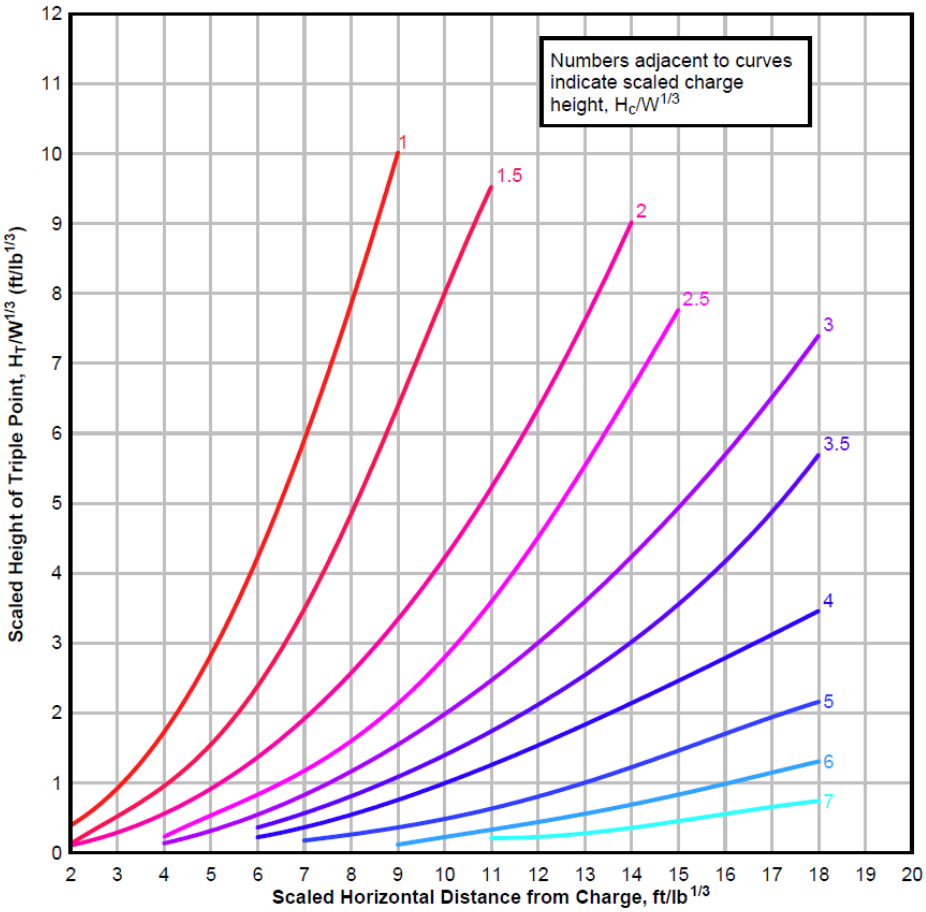

Figure 2-9 – Scaled height of triple point [TM5-1300, 1991].

Above the triple point one will observe dual pressure peaks created by the incident and reflected waves respectively. In contrast below the triple point the blast waves converge into a single pressure peak with a higher maximum pressure than that of the incident wave (Figure 2-10) [Haladuick et al., 2012].

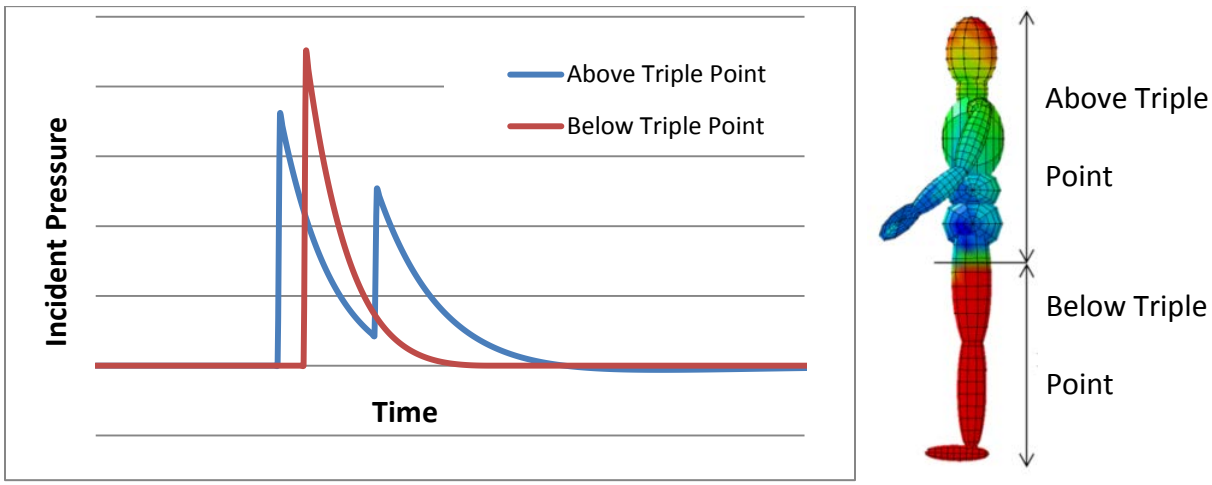

Figure 2-10 – Pressure history versus time of target locations above and below the Mach stem triple point [Haladuick et al., 2012].

2.6 Blast Wave Interaction with Surrounding Structures

Blast wave interaction with structures is complex due to the short time durations of a blast wave coupled with the high transient pressures present. Reflected pressure is defined as the maximum pressure at a wall or other rigid surface placed normal to the blast flow. In a large scale blast an object will exact a normal squashing compression effect on every exposed surface as the blast wave diffracts around the structure, as well as a drag loading effect where the structure is pushed on the incident wave side followed by suction on the contre coup side as the blast wave dynamic pressure passes over the target. [Smith et al., 1994]

When a blast wave interacts with a surface, the surface is subject to a large pressure discontinuity, and the impacted region creates a transient compressive stress wave in the material. This compressive wave will travel through the material until it reaches the rear surface, where the wave will reflect. This reflected wave will be in tension and add itself algebraically to the trailing edge of the incoming compressive wave [Cronin, 2012] If the stress at the impact point (or any point) exceeds the materials tolerance levels the material will plastically deform and a plastic stress wave will propagate along the material eventually dispersing enough energy through plastic deformation to disperse into an elastic wave. Elastic waves travel much faster and last for a longer period making them easier to observe. In a non-fluid medium the speed of sound is dependent on its bulk modulus and its shear modulus, whereas the shear modulus is zero for fluids.

Solid material speed of sound

$$a^* = \sqrt{\frac{K + \frac{4}{3}G}{\rho}}$$

Equation 2-35

Solid material speed of sound neglecting radial inertia

$$a^* = \sqrt{\frac{E}{\rho}}$$

Equation 2-36

Where:

- a^* = *Speed of sound*
- K = *Bulk modulus*
- G = *Shear modulus*
- E = *Young's modulus*

If the compressive stress wave encounters an interface between two constituents with dissimilar material impedance (ρa^*) or geometric impedance part of the wave will be

transmitted to the second material and part will be reflected. This is important when considering the interface between two tissues with impedance differences in the human body.

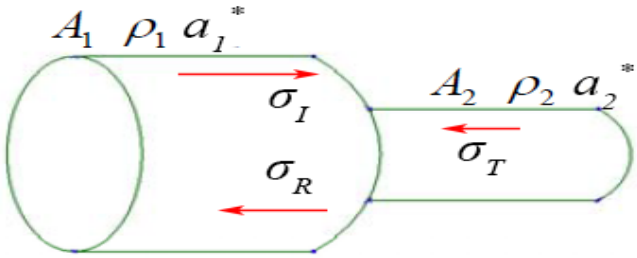

Figure 2-11 – Material and geometric impedance adapted from [Meyers, 1994]

Stress Transmitted

$$\frac{\sigma_T}{\sigma_I} = \frac{2A_2\rho_2 a_2^*}{A_2\rho_2 a_2^* + A_1\rho_1 a_1^*} \qquad \textit{Equation 2-37}$$

Stress Reflected

$$\frac{\sigma_R}{\sigma_I} = \frac{A_2\rho_2 a_2^* - A_1\rho_1 a_1^*}{A_2\rho_2 a_2^* + A_1\rho_1 a_1^*} \qquad \textit{Equation 2-38}$$

Where:

σ_I = *Amplitude of incident wave*
σ_R = *Amplitude of reflected wave*
σ_T = *Amplitude of transmitted wave*
A = *Area*
Subscript 1 = *Material 1*
Subscript 2 = *Material 2*

When $\rho_2 a_2^*$ is greater than $\rho_1 a_1^*$ a wave is transmitted of the same stress type (compressive or tensile) as the incident wave, whereas when $\rho_2 a_2^*$ is less than $\rho_1 a_1^*$ a wave of opposite type is transmitted.

Subsequent blast interaction with a human subject is extremely complex due to the multifaceted shapes and material properties of the human body. These complexities compound with an already complicated physical system and will be further investigated in the Injury Mechanisms section of this thesis.

Complex blast loading is created by the blast wave impinging and reflecting off surfaces in urban environments, enclosed areas, and inside armoured vehicles. This wave reflection has the potential to increase the blast loading on a subject resulting in higher levels of injury through wave superposition, and longer duration loading, (Figure 2-12). There is also potential for injury from the proximity of the surrounding structures [Stuhmiller et al., 1991].

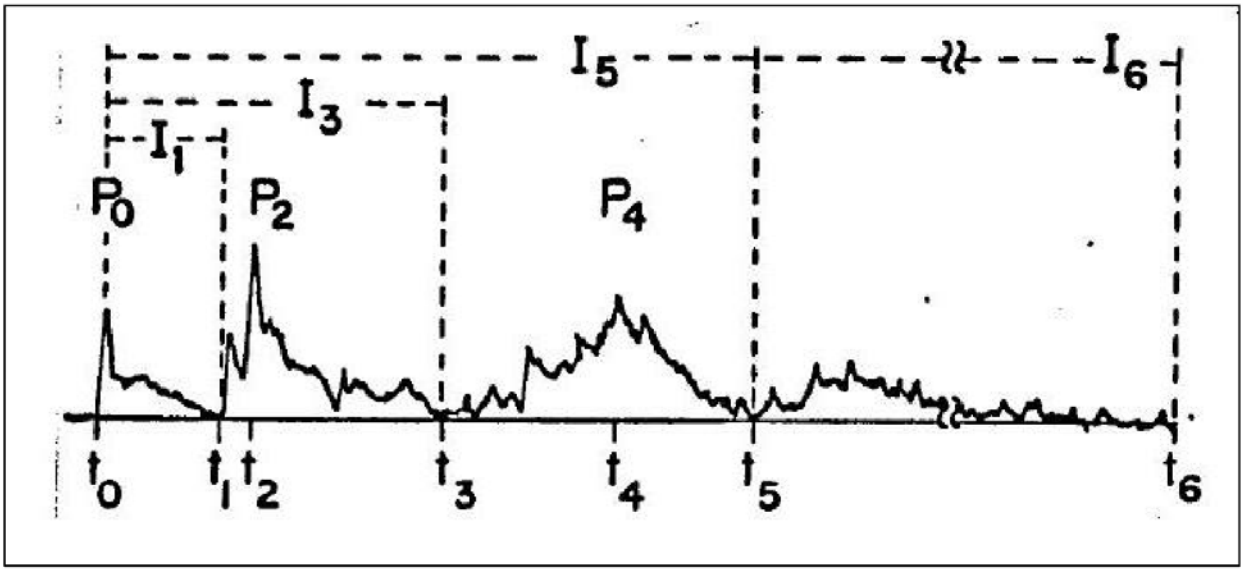

Figure 2-12 – Complex blast wave form inside an armoured vehicle [Richmond, 1985]

2.7 Improvised Explosive Device Characteristics

As of June 2013 in Operation Enduring Freedom, 1477 out of 3340 NATO fatalities were attributed to IEDs [icasulaties.org, 2013]. These weapons can be detonated with remote controls, command wires, pressure sensors, temperature sensors, trip wires, and suicide incidents. Recently IEDs have been primarily produced using homemade ammonium nitrate fuel oil material, (Figure 2-13), and not only have they become more prevalent but also they have increased drastically in size (Figure 2-14).

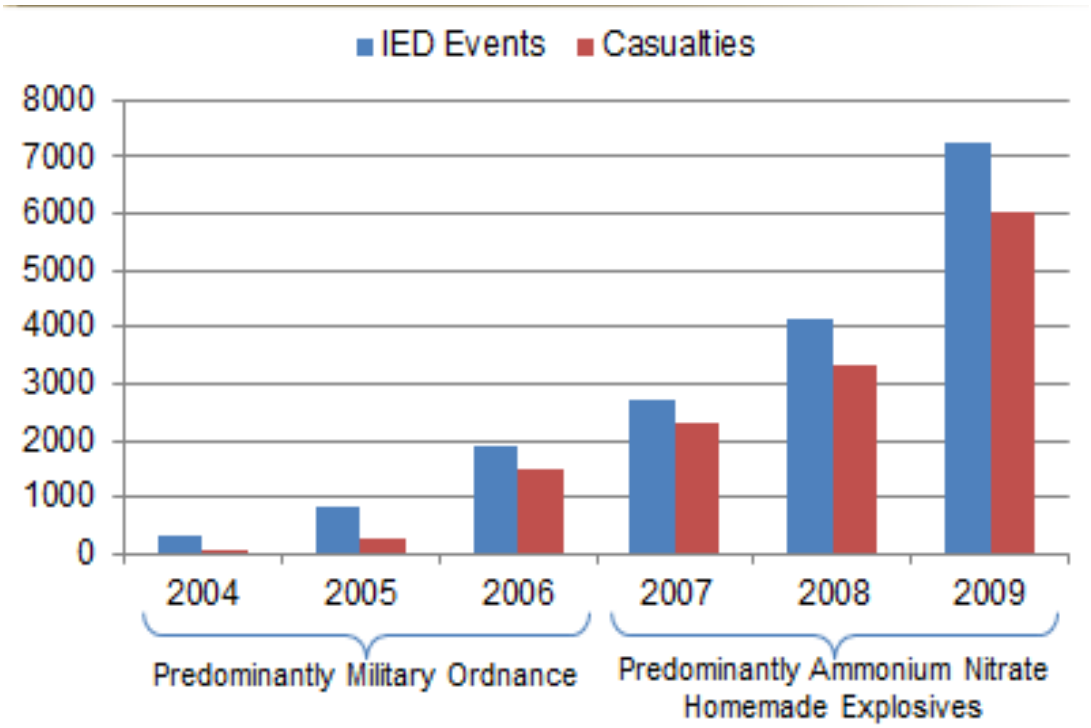

Figure 2-13 – IED material evolution in Afghanistan. [Flynn, 2009]

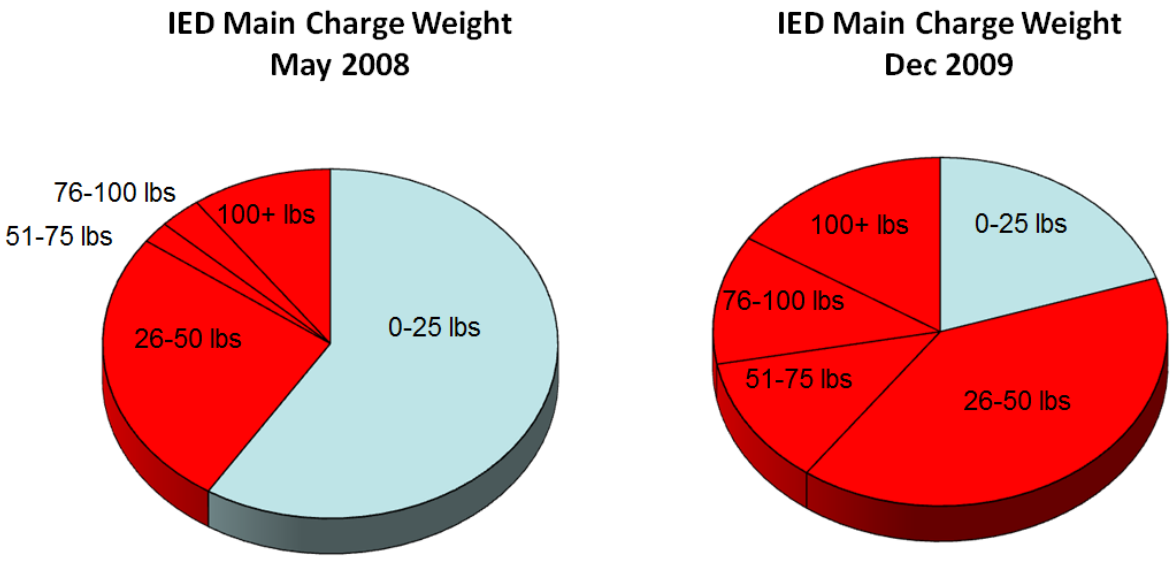

Figure 2-14 – The percentage of IEDs over the weight of 25 lbs has drastically increased [Flynn, 2009]

3 Background: Human Head Anatomy and Brain Injury

Blast injury is often defined using four categories of injury: primary, secondary, tertiary and quaternary. Primary blast injury is associated with the interaction between an explosive pressure wave and the body that can damage air-filled organs. Common primary blast injuries include: pulmonary barotrauma (blast lung), tympanic membrane (eardrum) rupture, gastrointestinal tract haemorrhage [Cooper and Dudley 1997]. Recently, primary blast injury has been linked to varying levels of traumatic brain injury (TBI) in soldiers exposed to blast loading [Saatman et al., 2008]. Secondary blast injury results from high velocity explosive debris or fragmentation impacting the body, creating penetrating trauma with external and internal bleeding. Tertiary blast injury is caused by the displacement of the body due to impulse force of the blast wave and the subsequent decelerative impact with surrounding obstacles or the ground. Crushing and blunt impact injuries are characteristic of tertiary blast injuries. Quaternary injury is the result of other factors during a blast including asphyxiation, burns, radiation poisoning, and inhalation of dust and gas particles. [Lockhart et al., 2011]

3.1 Overview and History

Understanding blast injury requires detailed knowledge of the blast loading conditions and the resulting injury mechanism. The occurrence of blast injury has been widely recognized and documented for many years [Bowen et al. 1968, Axelsson et al. 1994]; particular focus has been on air-filled organs and fragmentation injuries. Bowen is one of the most referenced sources in blast research; he derived three curves based on the position of a human relative to the incoming blast wave to predict lethality from lung damage due to free field blast overpressure vs. duration. The curves empirically predicted lethality from exposing different species of

animals to blast waves and observing whether the animal survived a 24 hour period following the incident. A total of 2097 experiments on 13 different species were performed giving estimates for 50% probability of a lethal dose or LD50. These in vivo animal responses were then scaled to the expected response of a 70 kg human male. The scaling was accomplished though dimensional scaling for the positive-phase overpressure duration based on the cube root of the ratio between body masses:

Pulmonary blast scaling $\Delta t_{Scaled} = \lambda \Delta t_{animal}\,; where\ \lambda = \left(\frac{M_{human}}{M_{animal}}\right)^{\frac{1}{3}}$ *Equation 3-1*

[Bowen, 1968]

Where:

Δt_{Scaled} = *Scaled Duration: Related positive phase duration on human*
M_{human} = *Mass human*
Δt_{animal} = *Amplitude of Transmitted wave*
M_{animal} = *Mass of exposed animal*

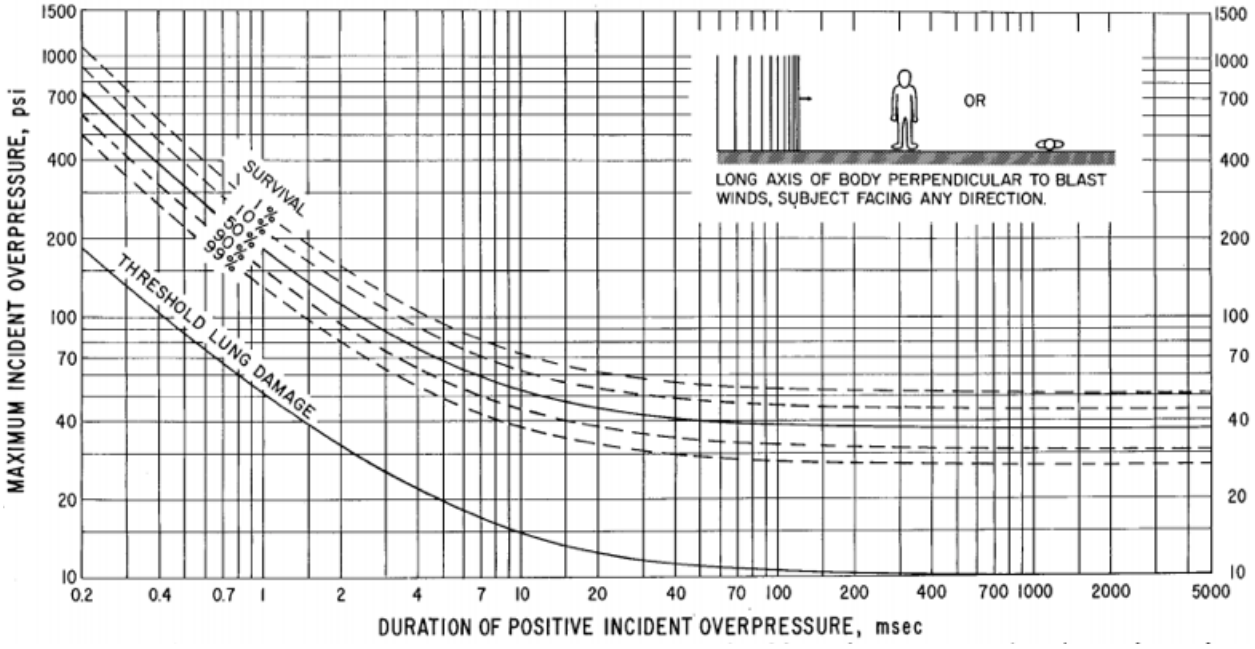

Figure 3-1 – Survival curves predicted for 70 kg man applicable to free-stream situations where the long axis of the body is perpindicular to the direction of propagation of the shocked wave [Bowen et al. 1968]

Both previous to and following Bowens research much of the blast injury field focused on pulmonary injury [Bogo et al. 1971; Clemedson, 1949; Hooker, 1924; Richmond and White, 1962], and this additional research enabled modifications to Bowens curves (Figure 3-2 [Bass et al. 2008]) and was used to better understand thoracic injury fuelling further research into improved blast mitigation techniques.

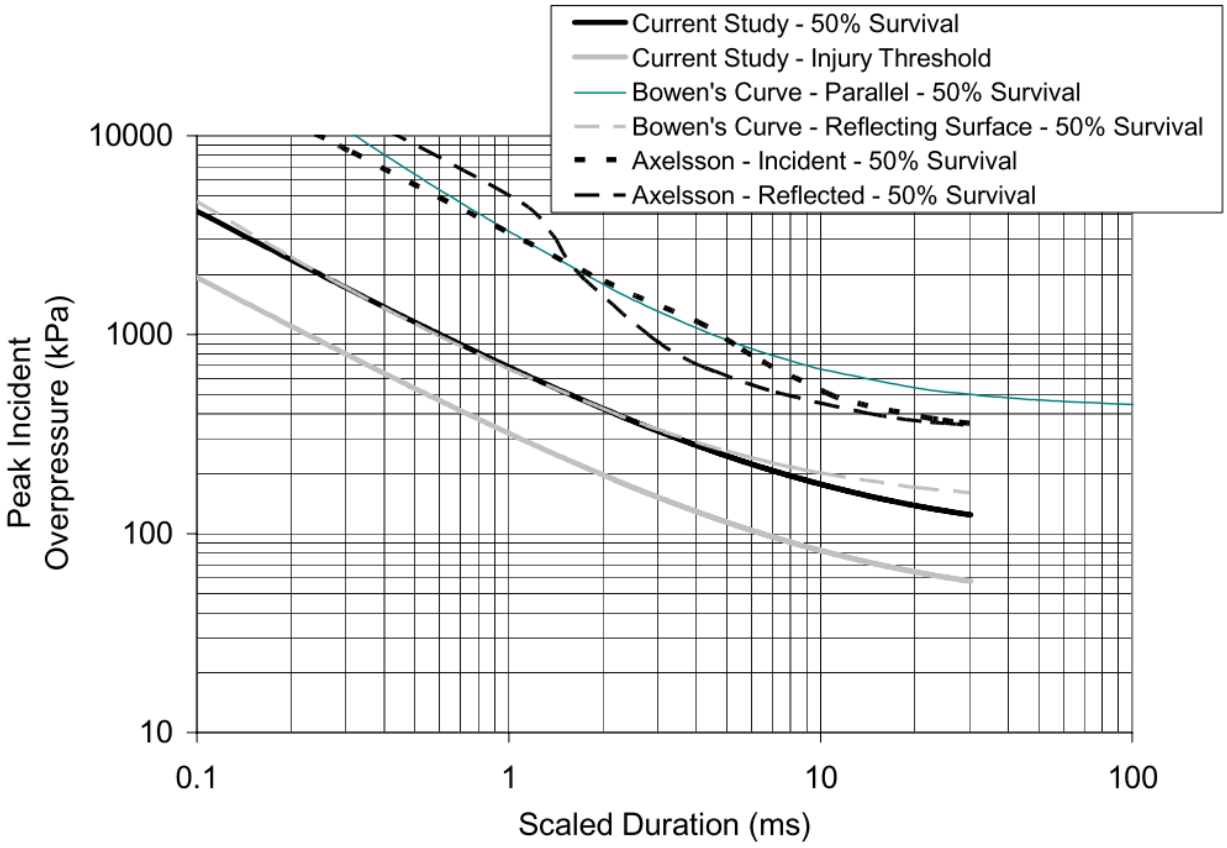

Figure 3-2 – Comparison of Incident Overpressure / Duration Blast Injury Criterion from Bowen, Bass, and Axelsson [Bass et al., 2008]

Symptoms of injuries from blast have been noted from as early as the Napoleonic Wars [Hinricsson, 1970], and American Civil war [Mitchell et al., 1864]; however, large scale prolonged explosive attacks and artillery barrages were not a major aspect of warfare until

World War I, where the head injury from blast phenomenon became known as shell shock: relating to a non-external head injury after an explosive incident. Recently reports began linking soldiers that had been previously exposed to blast with symptoms of post-traumatic stress disorder; Cernak et al. reported that up to 30% of 665 patients exposed to blast and treated during the 1990's Yugoslavia Wars had some form of central nervous system disorder [Cernak et al., 1999]. Based on these and other similar PTSD studies as well as parallel research into closed head injuries in automobile sector, blast induced mild traumatic brain injury became a major field for military medicine research in the early 2000's.

Blast exposure injuries are much more apparent in recent and ongoing conflicts including Operations Enduring Freedom (Afghanistan) and Iraqi Freedom. In these conflicts the percentage of casualties inflicted by blast related incidences has increased to 81% compared to previous wars (9% for US Civil War, 35% for WWI, 73% for WWII, 69% for Korean War, 65% for Vietnam War) [Owens et al., 2008]. This increased rate of injury percentage due to explosives is due to the increase in the size and prevalence of Improvised Explosive Devices (IEDs) used on the battlefield [icasualties.org, 2013; Flynn, 2009] (Figure 2-13).

Blast injury can also be qualitatively organized into categories based of the standoff distance and surrounding regime where the subject was located (Table 3-1).

Table 3-1 – Possible injuries to unprotected victims (high explosive detonation in open air) [Adapted from Wightman et al, 2001]

Injury	Near-Field						Far-Field
Total body disruption							
Burns & inhalation injuries							
Toxic inhalations							
Traumatic amputations							
PBI of the lung & bowel							
Tertiary blast injury							
PBI of the ear							
Secondary blast injury							
mTBI							

With the increase in survivability from pulmonary injuries due to more effective modern body armour [Wood et al., 2012], the increase in size and usage of enemy explosives, and the increased awareness in the medical field of diagnosing mild traumatic brain injury (mTBI) (Warden et al., 2005) there has been an increase in blast related brain injuries.

The remainder of this chapter will focus on the cause and effect primary blast injury (PBI) and its relevance to Traumatic Brain Injury (TBI).

3.2 Anatomy of the Human Head

The human head comprises of the skull, face, teeth, scalp, connective tissue, brain, three meninges, cranial nerves, sense organs, and other elements including cerebral spinal fluid, blood vessels, lymphatic system and fat [Moore et al., 1999]. Though this thesis does not involve detailed models of the human head, the interaction and injury response of the different parts of the head during a blast scenario is of upmost importance when discussing potential insults and their subsequent injury mechanisms.

3.2.1 The Skull

The skull is supported on the summit of the cerebral spine at the C1 vertebrae. It is made out of 22 bones, 14 facial and 8 cranial which (Figure 3-3); these bones are connected via sutures that are fibrous at birth but ossify over a few years [Cronin, 2012]. The cranial bones make up the main protective layer for the brain, and have attachment sites for jaw, head and neck muscles. The skull is covered with 5-7 mm of scalp which contains hair bearing skin, connective tissue, muscle and fascial layer.

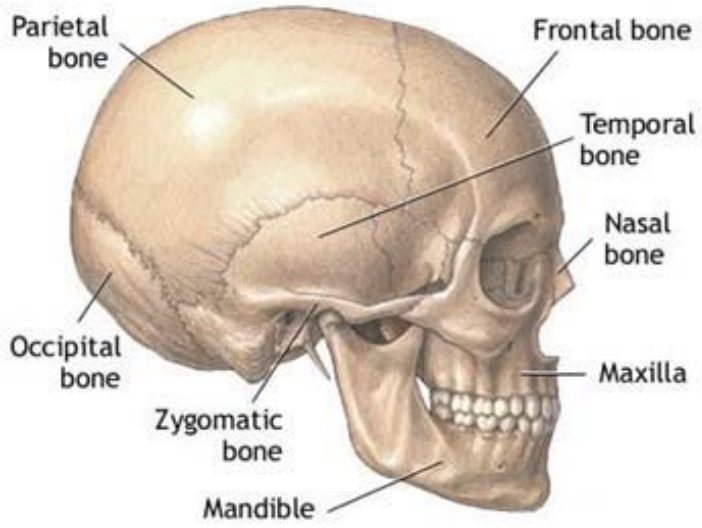

Figure 3-3 – Simplified Skull anatomy [Cowles, 2007].

The skull is 4-7mm thick with its thinner sections in areas with well-developed muscle tissue such as the temporal region, and the cranial cavity has an approximate volume of 0.0013 to 0.0015 cubic meters [Moore et al., 1999]. The brain stem connects the spinal cord to the brain through the posterior foramen magnum which is a large opening in the base of the skull.

The bones of the skull are made up of an inner and outer cortical bone layer (the tables) with a thin cancellous bone layer (the diploe). The outer table is thick and tough whereas the inner table is thin, dense, brittle, concave, and smooth. These cortical layers withstand greater stress than the diploe, have a higher degree of stiffness, but will fracture with low amounts of strain. In contrast, the diploe is porous bone with similar properties to vertebral cancellous bone and has a greater ability to withstand strain but a low stiffness [Nahum et al., 2002].

3.2.2 The Brain

The brain is the largest and most complex component of the nervous system. It contains between 85 and 100 billion neurons and glial cells [Hole, 1984; Azevedo et al., 2009] that control: sensory systems, movement, behaviour, higher mental functions such as memory and learning, and homeostatic functions. The neurons are specialized for rapid communication and consist of a cell body, dendrites, and axons. Dendrites receive electrical impulses from other neurons, and axons transmit electrical impulses away from the cell body to other neurons or to muscle and gland systems. Axons can reach lengths up to thousands of times the length of the cell body [Hollinshead et al., 1985] (Figure 3-4). When the brain or spinal cord is injured, the axons are unable to recover to convey electric impulse or biochemicals from the cell through to the neurons destination and permanent disability can occur.

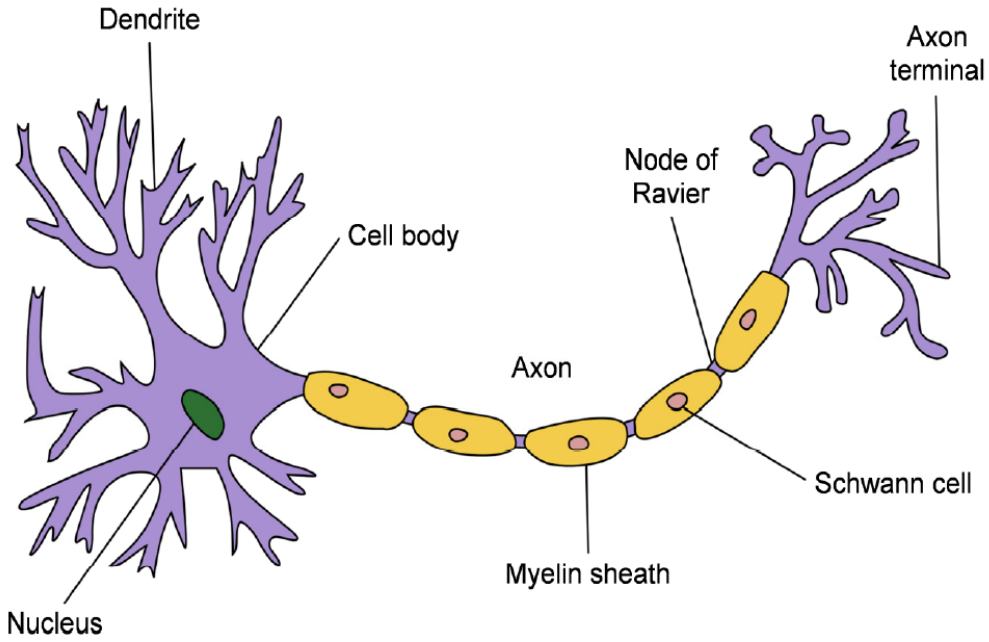

Figure 3-4 – Structure of a neuron. [Creative Commons]

3.2.2.1 Macrostructure of the Brain

The brain is divided into the cerebrum, cerebellum, brain stem, and diencephalon (Figure 3-5). The cerebrum makes up 7/8 of the brains mass and is made up of two paired hemispheres connected by the corpus callosum, which is a flat neural selection of fibres that act as a communication bridge between the right and left sides of the cerebrum. Each hemisphere of the cerebrum is further subdivided into four lobes named after the anatomical name of the skull bones that they lay inferior to. Each lobe has several functions for which they are responsible: O*ccipital Lobe*: visual processing, *Temporal Lobe*: language, memory and formation of emotions, *Parietal Lobe*: sensory control and abstract reasoning, *Frontal Lobe:* intellectual functions such as reasoning, decision making, integration of sensory function, and the voluntary

execution of movement [Kapit et al., 1993].

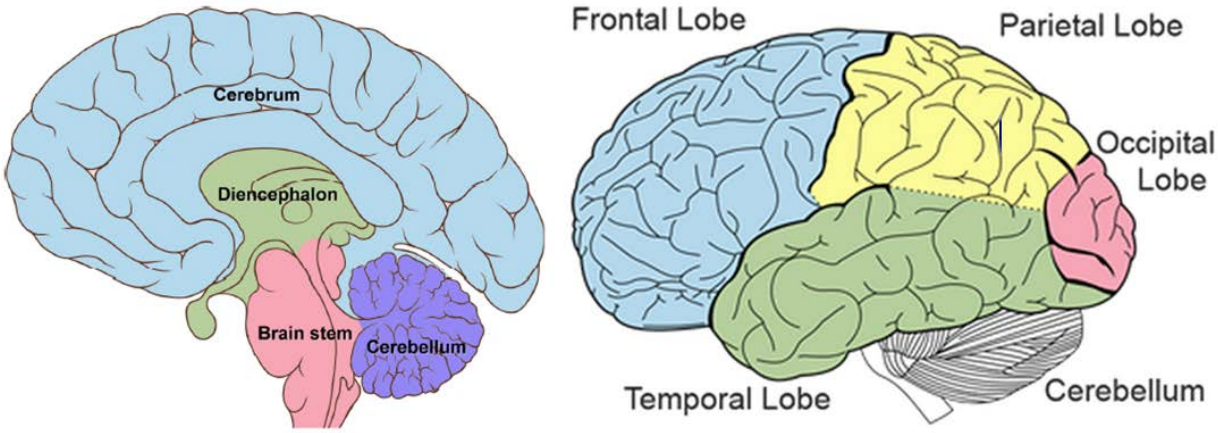

Figure 3-5 – Macrostructure of the brain. [Cheng, 2011]

The surface of the brain has a series of folds or convolutions and is covered in a 2-5 mm layer of cerebral cortex grey matter; grey matter consists of neuronal cell bodies and is generally responsible for processing and cognition. The underlying white matter is arranged into tracts that serve to connect to other lobes or other parts of the central nervous system acting as a relay and communicating network, these white matter axons are often damaged in the case of diffuse axonal injury [Karami et al., 2009].

The cerebellum contains approximately 80% of the brains neuronal cells, but makes up only 10% of its weight. It is also separated into left and right hemispheres and is separated by a falx cerebelli. The cerebellum is responsible for motor control, and coordination of different sensory systems

The brain stem connects the spinal cord to the brain through the diencephalon which contains the thalamus and hypothalamus. The thalamus integrates all incoming impulses from sensory

pathways producing an appropriate motor response. The hypothalamus maintains the body's homeostasis functions.

3.2.2.2 Protective Systems of the Brain

In addition to the skull, the brain is protected by three meninges and cerebral spinal fluid (Figure 3-6). Cerebral spinal fluid (CSF) is a colorless liquid that bathes the exposed surfaces of the central nervous system, filling the subarachnoidal space completely surrounding the brain and spinal cord. CSF supports 95% of the brains weight and prevents the brain from being crushed by its own bulk [McKinley et al., 2008]. The CSF also provides a liquid cushion to protect neural surfaces from sudden movements of the brain relative to the skull. The CSF is a Newtonian fluid with a dynamic viscosity and density similar to plasma ($\mu = 0.01$ and $\rho = 1.0$ g/cm3) [Loth et al., 2001]. Each cerebral hemisphere contains a CSF cistern from where the fluid is secreted (at a rate of 0.3 to 0.7 mL/min) and reabsorbed approximately 3 times a day continuously, resulting in a relatively constant volume of 130-140 mL which applies a fluid pressure of about 1.33 kPa [Hole, 1984].

The three meninges are made up of mostly connective tissue. The three meninges protect and support the brain and spinal cord from surrounding bones, form part of the walls of blood vessels, and the sheathes of nerves as they enter the skull [Nahum et al., 2002]. The *Dura matter* is tough fibrous membrane that surrounds the spinal cord, the *Arachnoid* is a spider like membrane that occupies the subdural space, and the *Pia matter* covers the surface of the brain and dips well into each fissure. Under trauma, the Dura matter can separate producing an

epidural hematoma and/or veins crossing between the Arachnoid and Dura may tear filling the subdural space with fluid or blood known as a subdural hematoma.

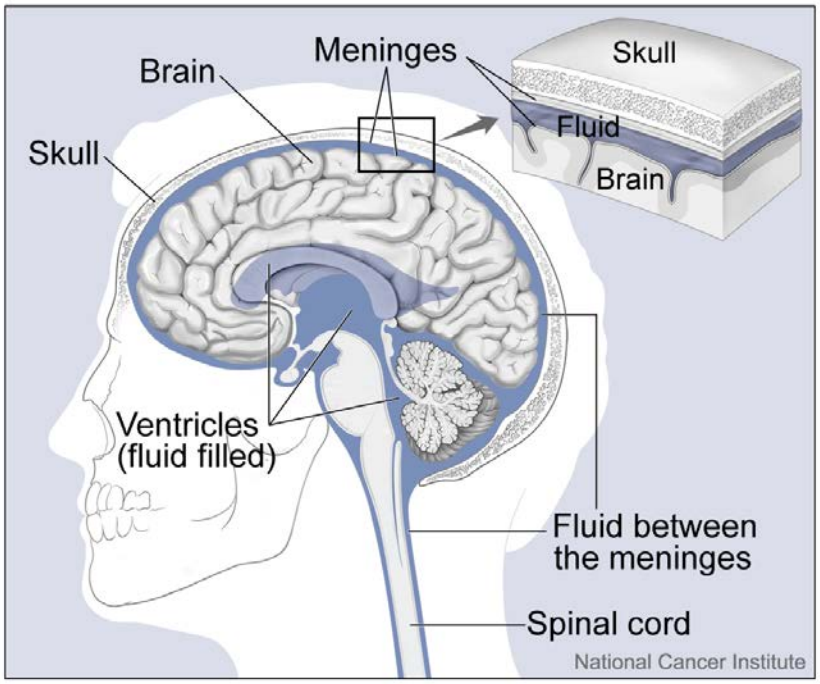

Figure 3-6 – Protective systems of the brain displaying CSF, ventricles, and the protective meninges [National Cancer Institute, 2013].

3.3 Head Injury

Head injury can be separated in to focal and diffuse injuries both of which could be the result of a blast event. Below is a list of common head injuries as defined by Nahum et al. [Nahum et al., 2002]:

- **Focal Injuries**: Caused by soft brain tissue impacting the hard inner cranial table.
    - Acute subdural hematoma: Direct lacerations of cortical veins and arteries by penetrating wounds, large contusion bleeding into the subdural space, tearing of veins that bridge the subdural space as they travel from the brains surface to the various Dural sinuses, 60% mortality.

- Extradural Hematoma: Trauma to skull and underlying meningeal vessels, 15- infrequently occurring, 43% mortality.
- Cerebral contusion: Most frequently found lesion following head injury. Consists of heterogeneous areas of necrosis, pulping, infarction, haemorrhage, and edema (brain swell).
- Contusions: coup and contrecoup (occurring predominately at the frontal and temporal lobes when the brain is impacted against the inner table) 25-50% mortality.
- Intracerebral hematomas: Homogeneous collections of blood within the cerebral parenchyma. Most commonly caused by sudden acceleration/deceleration of the head. Haemorrhages begin superficially and extend deeply into the white matter; 6-72% mortality rate that varies with the amount of loss of consciousness of the patient.
- Skull Fractures:
  - Linear fracture: caused by large distributed loads to the skull, doesn't necessarily cause brain damage.
  - Depressed fracture: depending on contact area could be either: pierced or caved in, often then combined with internal brain injuries.

- **Diffuse Injuries**: Caused by shear forces damaging connective tissue between the brain and the skull from extreme accelerations.
  - Mild concussion: Fully reversible no loss of consciousness, issues with diagnosis due to the inability to image the injury mechanism, and the potential for symptoms to cross over with psychological disorders.
  - Cerebral concussion: Loss of consciousness, most good recovery (95%).
  - The longer the loss of consciousness the higher the severity of the injury and the less likely the patient is to fully recover.
  - Diffuse Axonal Injury (DAI): Mechanical disruption of many axons in cerebral hemispheres and subcortical white matter. Axonal disruptions extend below the midbrain and into brainstem to a variable degree giving abnormal brainstem

signs from the degeneration of white matter tracts. DAI involves loss of consciousness for days to weeks, high mortality and disability rate. Brain swelling may superimpose on DAI furthering the effects of primary brain injury. Mortality rate with brain swelling 33 to 55%.

3.4 Traumatic Brain Injury from Primary Blast Exposure

Recently, primary blast injury has been linked to varying levels of traumatic brain injury in casualties who were exposed to blast loading [Saatman et al., 2008]. The Defense and Veterans Brain Injury Center (DVBIC) estimates that 280734 US service personnel were diagnosed with TBI between 2000 and 2013. The majority (82.4%) of those affected by TBI are suffering from mild traumatic brain injury (mTBI) (Figure 3-7) [DVBIC].

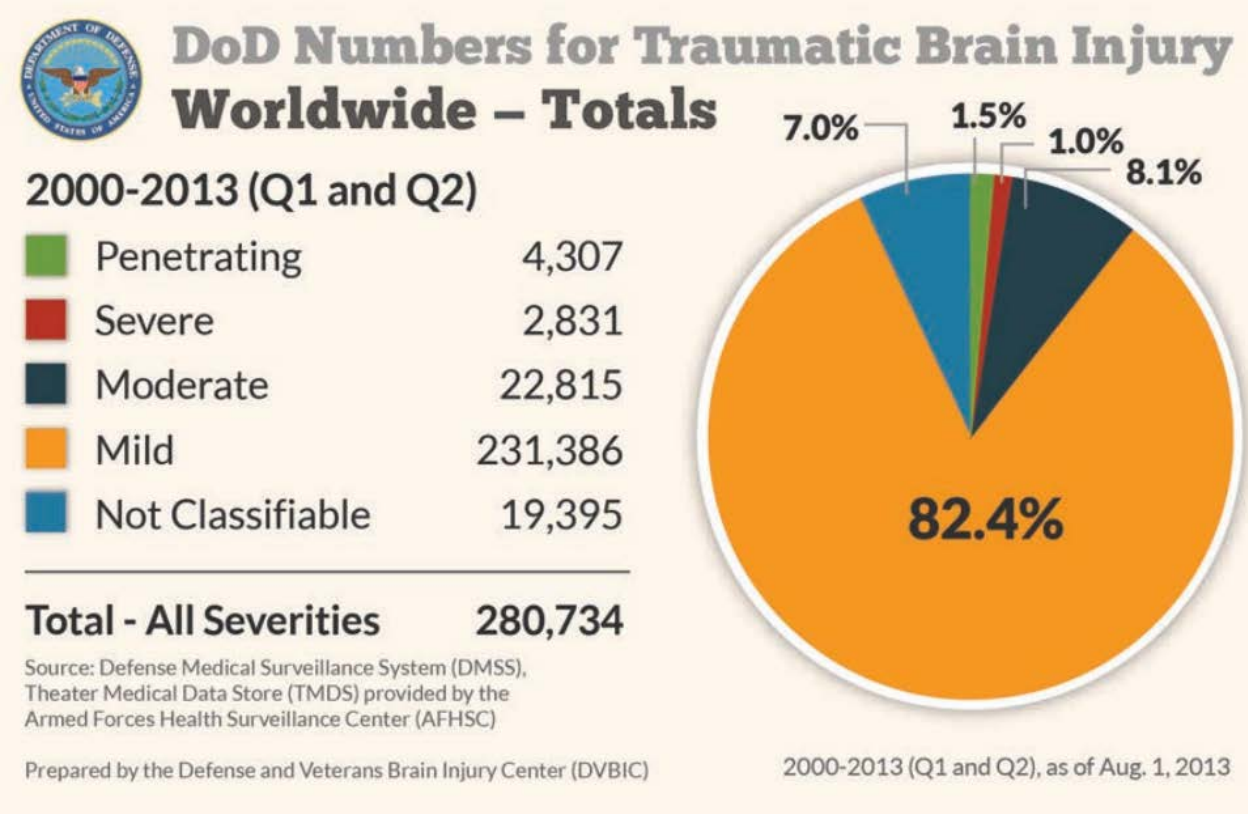

Figure 3-7 – Department of Defense (DoD) numbers for Traumatic Brain injury, worldwide totals.[DVBIC]

Though summary casualty numbers like these are often controversial and many of these injuries occur in non-deployed incidents, there is no doubt that many service members are returning from conflict suffering from some form of TBI. The head injury mechanism corresponding to blast exposure is not well understood at present. This difficulty in understanding stems from the inability to measure intracranial phenomena in living subjects, the high accelerations of the head experienced over very short time duration, and the complex interactions between a blast wave and the human body. Although the injury mechanism is not well understood it is believed that mTBI may result from primary interaction with the blast wave leading to some damage or change in function at the tissue or cellular level. [Schmitt et al., 2014]

When blast waves, which travel faster than the speed of sound in air, interact with the body the large pressure differential results in rapid accelerations of the body creating a high-frequency stress wave that propagates through tissue. Experimental models to evaluate head response and the potential for brain injury have included a variety of techniques and test species in order to develop a reproducible model of trauma that exhibits anatomic, physiologic, and functional responses similar to those described clinically [Nahum et al., 2002]. Applying these models to blast-induced traumatic brain injury produces significant difficulties in determining the measureable parameters that are associated with a specific physical or psychological symptom as these symptoms often do not become apparent for some time following the insult.

Traditional injuries relating to non-impact acceleration of the head include: diffuse axonal injury (DAI), indirect contrecoup contusions, tissue stresses produced by motions of the brain

hemispheres relative to the skull and each other, as well as subdural hematomas produced by a rupture of bridging vessels between the brain and the dura matter [Hurley, 2006]. Symptoms of severe TBI include: unconsciousness, amnesia and severe headaches while symptoms pertaining to mTBI include: insomnia, vertigo and memory deficits [Cernak, 2011]. There is often no visible injury pattern associated with blast inflicted TBI, and thus it cannot be identified through direct observation or medical imaging. Furthermore, the symptoms inflicted by mTBI resemble to those of to PTSD, and thus a patient may be misdiagnosed or suffer from comorbidity [Najavits, 2011].

3.5 Primary Blast Head Injury Metrics

A brain injury threshold is the level above which structures of the head may fail or stop functioning normally. Currently, there are no validated head injury metrics to predict head injury resulting from a blast event due to: limited biomechanical details of living brain tissue, limited pathology of brain injuries, and the inability to measure loads or deformations of a living being [Margulies, 2011]. There are several common head injury metrics that provide a starting point for assessing the severity of a blast wave on the head. The metrics include: head Center of Gravity (CG) acceleration, incident pressure, and intracranial pressure [Singh et al., 2013]. It should be emphasized that the metrics used in this thesis are not being proposed to predict blast mTBI, but only to provide a frame of reference in this study for head kinematic response and the potential for injury.

3.5.1 Head Injury Criterion (HIC)

The Head Injury Criterion (HIC) is the most commonly used head injury metric for accelerative head injuries, developed for use in the automotive industry with a time integral of the resultant acceleration of the head over the duration of the insult.

Head Injury Criterion

$$\mathrm{HIC} = \left[\frac{1}{\tau_2 - \tau_1}\int_{\tau_1}^{\tau_2} a(t)dt\right]^{2.5}(t_2 - t_1)$$

Equation 3-2

[Hutchinson et al, 1998]

Where:

HIC = *Dimensionless number when using acceleration in terms of g's*

t_1, t_2 = *Initial and final times during which the HIC obtains a maximum value*

$a(t)$ = *The resultant acceleration in g's measured at the center of gravity of the head*

The HIC is based on the Wayne State University Cerebral Concussion Tolerance Curve (WSTC) which was developed over the period of a decade through measuring the effects of acceleration on intracranial pressure of dogs, monkeys, and human cadavers [Gurdjian et al., 1966]. The WSTC was an experimental correlation between effective acceleration of the head and the impact time duration, and indicates the estimated threshold values of human brain injury hazard.

This injury criterion has been criticized by some head injury researchers; however, there has been considerable difficulty encountered in developing a new head injury standard due to the lack of understanding regarding the response of the brain to exterior mechanical inputs. Detractors of the HIC note the several limitations to this metric. There is concern that a single criterion, based upon a single parameter, be extended to all types of head injury for all segments of the population [Goldsmith, 1981]. There is an assumed time dependence of the tolerable average acceleration which leads to predictions that short-duration / high

acceleration events and long-duration / low acceleration events yield equal risks of closed head injury [Newman et al., 2000]. It is generally defined for accelerations longer than 1 ms and some blast accelerations may be shorter [Newman et al., 2000]. Furthermore, the HIC is not injury specific and does not account for variation in brain mass or include a description of the internal brain kinematics associated with head injury.

In this thesis the HIC is not used as a Go / No-Go criterion but as a benchmark of potential injury from various levels of insult. The HIC metric of reference was HIC_{15}, this metric has a maximum time interval between t_1 and t_2 of 15 ms and was used with the corresponding Federal Motor Vehicle Safety Standards tolerance level of 700 [Hutchinson et al., 1998]. This tolerance level of 700 is a conservative estimate of the 5% risk to obtain an Abbreviated Injury Scale (AIS) level 4 injury, (Table 3-2), for a midsize male [National Highway Traffic Safety Administration]. The HIC is integrated over a time interval of the peak acceleration produced by blast wave interaction with the head.

3.5.2 HIC Value with Expanded Prasad/Mertz Injury Probability Curves

To relate the HIC_{15} values to potential injury severity the expanded Prasad/Mertz probability curves are utilized [Prasad et al., 1985]. These curves, (Figure 3-8), relate the HIC to the percentage of persons that would be at risk of a certain level of head injury based on the Abbreviated Injury Scale (Table 3-2); the AIS ranges form no injury (AIS0), to no loss of consciousness but headache and dizziness (AIS1), to different levels of unconsciousness (AIS2-5), and untreatable potentially lethal insult (AIS6). These curves inherently operate under the assumption that the HIC is an appropriate indicator of injury.

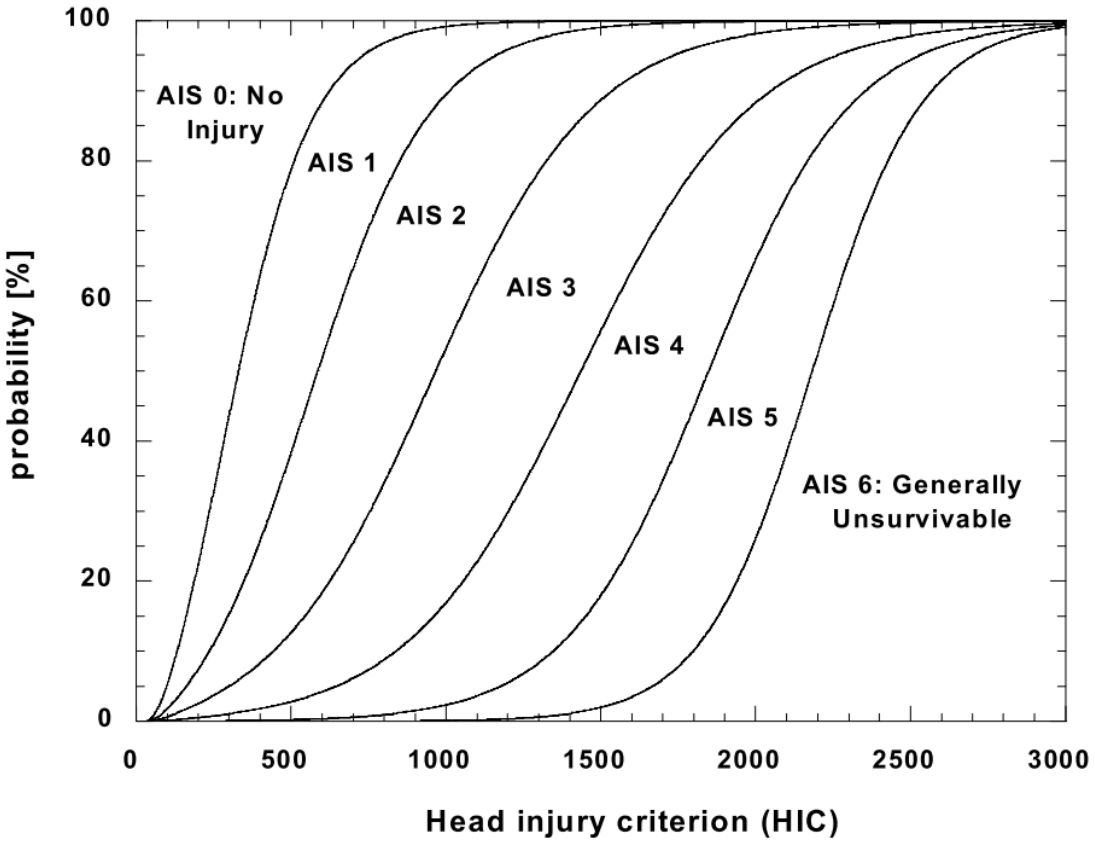

Figure 3-8 - Prasad/Mertz expanded probability curves used to determine injury probability, based on HIC value calculated from head acceleration traces. [Adapted from Dionne et al., 1997]

Table 3-2 – Abbreviated Injury Scale for concussive injuries including severity level and associated human injury [Gennarelli et al. AIS 2005].

AIS Severity Level	AIS Human Injury	Description of Severity
0	None	No Injury
1	Mild Concussion, Headache, Dizziness, No Loss of Consciousness	Minor
2	Loss of Consciousness < 1 hour	Moderate
3	Loss of Consciousness 1 – 6 Hours	Serious
4	Loss of Consciousness 6-24 Hours	Severe
5	Loss of Consciousness > 24 Hours	Critical
6	Lethal	Maximal (Currently Untreatable)

There is also a suburb correlation between AIS severity and survival / Mortality, (Figure 3-9).

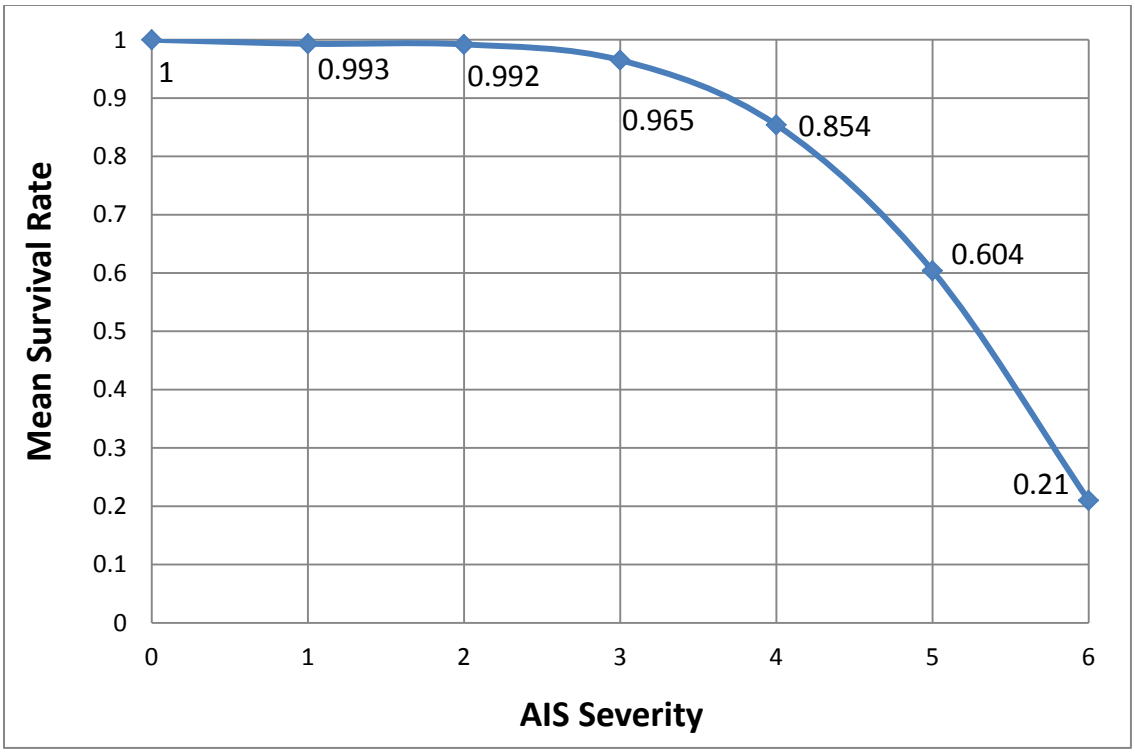

Figure 3-9 – AIS Severity vs Mean Survival Rate [Adapted from Gennarelli et al. AIS 2005].

3.5.3 Peak Incident Pressure vs Probability of Fatality

Incident pressure has been proposed as a potential brain injury metric by Rafaels et al. Rafaels et al. proposed that like the Bowen curves for lung based pulmonary injury the brain also has an injury threshold corridor which may correlate with incident pressure. Using rabbits as test subjects, exposing only their heads to blast and mass scaling the results using a similar method to how Bowen scaled rabbits to human subjects, the authors created a 50% probability of lethality curve (Figure 3-10). The most common site of hemorrhage was near the brainstem with the medulla oblongata or vagal nerve likely being affected, causing the resulting apnea.

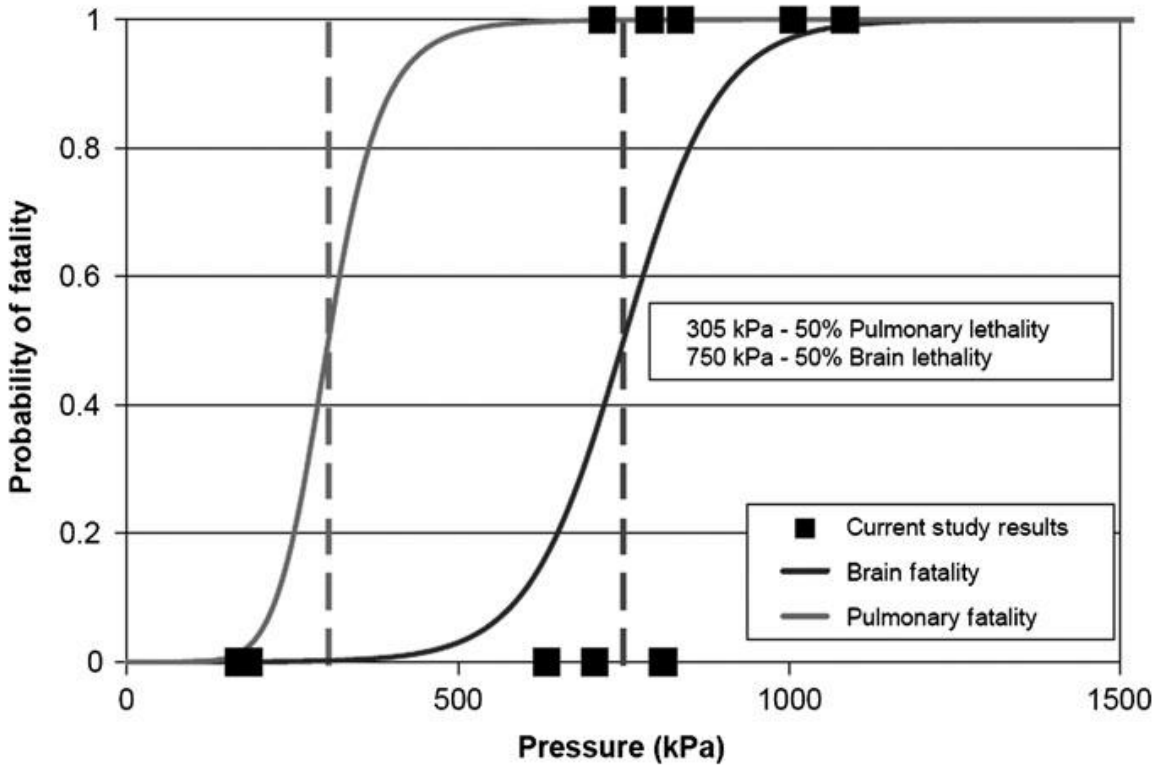

Figure 3-10 – Logistic risk functions for survival of both brain and pulmonary injuries caused by primary blast waves. The solid lines represent the risk of injury for the pressures on the x-axis. The dashed lines highlight the overpressures needed for a 50% probability of fatality. The risk function for brain injury was determined using the experimental data. The risk function for pulmonary injury was determined by applying the risk from Bass et al. 2008 with the blast parameters in this study [Rafaels et al., 2011].

The primary blast tolerance of the brain is higher than the primary blast tolerance of the lungs (Figure 3-10). This was an expected outcome as the prevalence of blast induced TBI has only become prevalent in recent times with better thoracic protection, and has been seen in previous studies [Bogo et al., 1971; Clemedson and Pettersson, 1953; Krohn et al., 1941]. As only 12 tests were performed the primary blast brain lethality risk curves were generated parallel to the pulmonary risk curves developed by Bass et al. [Bass et al. 2008].

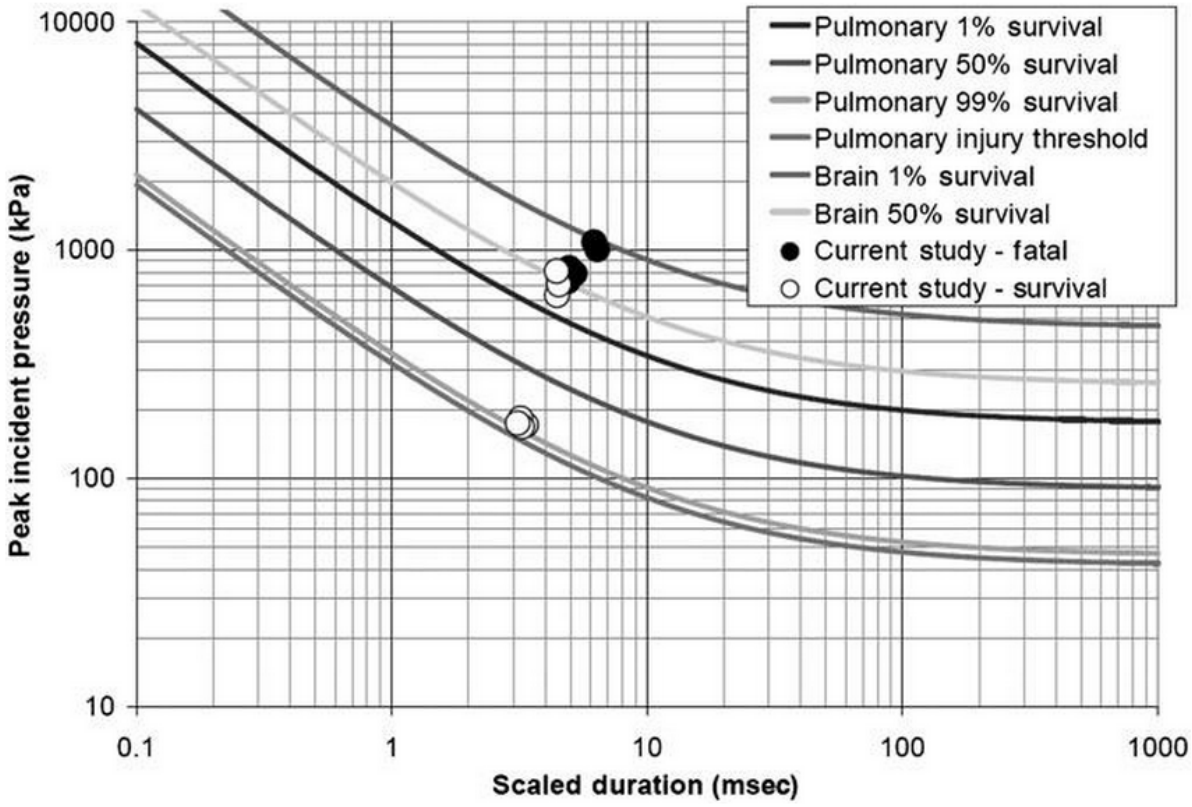

Figure 3-11 – Brain and pulmonary injury criteria across various overpressures and durations. The area in the lower left-hand side of the figure has a low risk of injury, and the area in the upper right-hand side of the figure has a high risk of injury. The risk of fatality from brain injuries requires higher pressures and longer durations than pulmonary injuries [Rafaels et al., 2011].

It is important to note that these results are for LD50, and are not directly relatable to mild traumatic brain injury. Limitations of this model include the small number of tests performed, and potential issues with mass scaling including: ratio of white matter to grey matter, brain geometry, brain organization and scale factor errors as none have been empirically tested for brain injuries. The peak incident pressure injury metric is not a definitive answer and will not be used in this thesis; however, it has the potential to be used as an estimation for brain injury.

The Rafeals et al. study also highlights the difficulty in establishing tolerance scales for blast injury to the head.

3.5.4 Dynamic Intracranial Pressure Threshold

Metrics based on dynamic intracranial pressure inherently include the severity of loading, and may hold promise as an injury metric [Singh et al., 2013]; however, this criteria is only available to numerical models, experimental tests using dummies, Post Mortem Human Subjects (PMHS), and properly configured in-vivo tests of animals. It is not possible to use this metric on a live human subject to determine injury, and no way to measure this variable using global kinematics, thus it will not be investigated in this thesis, but it is studied in a parallel study at the University of Waterloo [Singh et al., 2013].

4 Background: Explicit Finite Element Modelling Applied to Blast

The finite element method (FEM) divides a large complicated problem into a series or collection of smaller problems with a finite volume and time steps. The subdivision of a large problem into simpler parts enables an accurate representation of complex geometry, the inclusion of different material models, the capture of local effects, and the ability to view the total solution. Geometrically, the problem is discretized into simple geometric shapes called elements. Elements are triangles and quadrilaterals in two dimensions, and hexahedrons or tetrahedrons in three dimensions; when elements are grouped together to create a geometry it is known as a mesh (Figure 4-1). The accuracy of a FEM model is a function of the mesh resolution (element size), the element type, and shape of elements used to define the mesh.

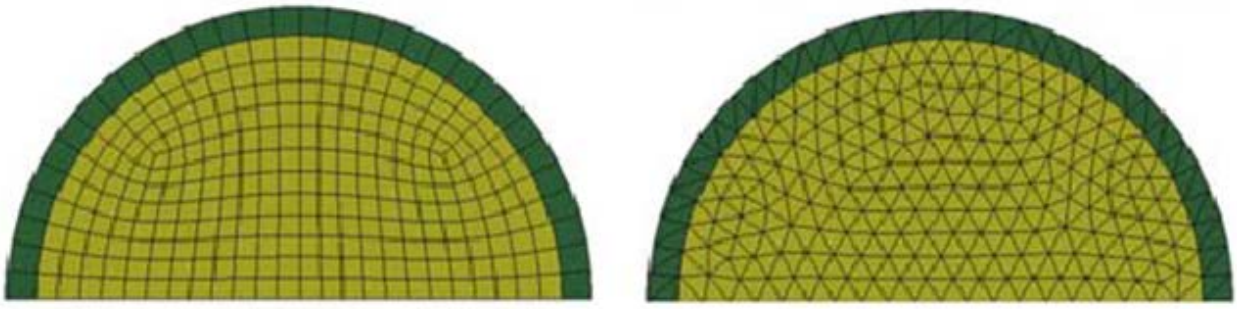

Figure 4-1 – Example of a meshed sphere using hexahedral and tetrahedral geometric element types. [Panzer et al., 2012]

Finite element analysis is traditionally described using Lagrangian or Eularian spatial referencing. In Lagrangian referencing the mesh distorts along with the material motion, and the material is not allowed to move between meshed elements. A Lagrangian reference can be considered a control mass problem in which the element distorts over time but the mass remains constant. Lagrangian referencing is most often used for solid mechanics problems with

small material deformation, and is not readily applied to blast problems due to the instability from large deformations of the mesh produced by the expansion of the explosive gases. In Eularian referencing the mesh is fixed in space and the material flows through the mesh from element to element, there can be two or more materials mixed within the same element. Eularian referencing utilizes a constant volume approach to problem solving. Eularian spatial referencing is most often used in fluid dynamic problems where the motion of the material is the major concern [Reddy, 2005]. This study used a mixture between the Lagrangian and Eularian frames of reference referred to as Arbitrary Lagrangian Eularian (ALE) formulation.

4.1 Explicit Finite Element Modelling

The explicit finite element approach provides a framework for detailed simulation of nonlinear impact biomechanics problems [Cronin, 2011]. LS-Dyna is an explicit finite element program, distributed by Livermore Software Technology Corporation. It is capable of solving dynamic or transient multi-physics problems. Applications include: impact and impact response, deformation, fluid structure interaction (FSI), and thermal analysis. This software is used to preprocess, post process and solve finite element problems using specified keywords to define part location, geometry, material properties, initial conditions, loading, boundary conditions, part to part interaction and contact detection. The explicit formulation requires many computational cycles over small time increments, allowing the equations to be solved at discrete time intervals using a central difference integration scheme. This formulation splits each large problem into small workable time steps that allow each individual finite element to solve a circular stress strain partial differential equation problem at its integration points

(Figure 4-2). The subdivision of a problem benefits from the use of multiple computer processors working simultaneously [Cronin, 2011].

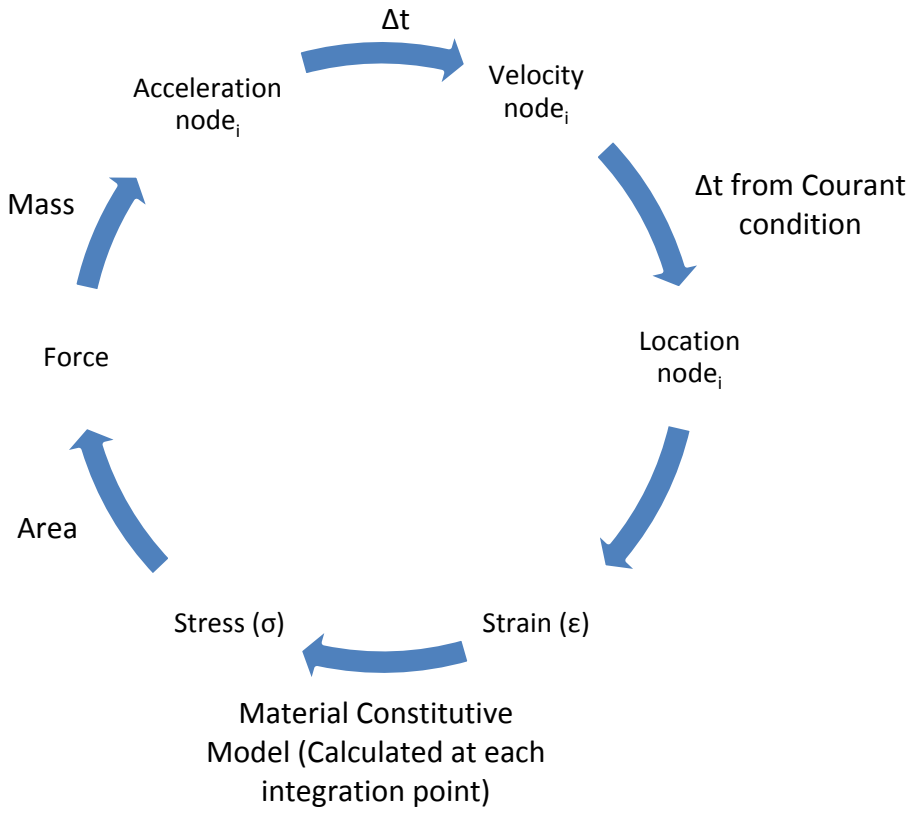

Figure 4-2 – Explicit finite element modelling problem solving steps.

The simplified minimum time step is determined by the Courant condition [Hallquist, 2006]:

Minimum time step $$\Delta t = \frac{L}{C}$$ *Equation 4-1*

Where:

Δt = *Minimum time step*
L = *Characteristic element Length*
C = *Wave speed in element medium*

4.2 Arbitrary Lagrangian Eularian Formulation

The Arbitrary Lagrangian Eularian (ALE) formulation combines the Lagrangian and Eularian frames of reference to resolve the technical difficulties that each experience through an advection step (Figure 4-3). First a Lagrangian step is taken where the mesh velocity is equal to that of the fluid material velocity [Souli, 2004]. Once the mesh is distorted an advection or remapping step is taken where the material is stationary and the mesh is incrementally rezoned by moving the nodes a small fraction of the characteristic length of the surrounding elements [Hallquist, 2006]. The distorted material state is then remapped onto the new rezoned mesh allowing the influx of new material into each new element. The ALE multi-material formulation is used to overcome the difficulties of large mesh distortion found in the Lagrangian reference and thus is appropriate to be used to simulate the detonation of a high explosive and the propagation of a shock wave.

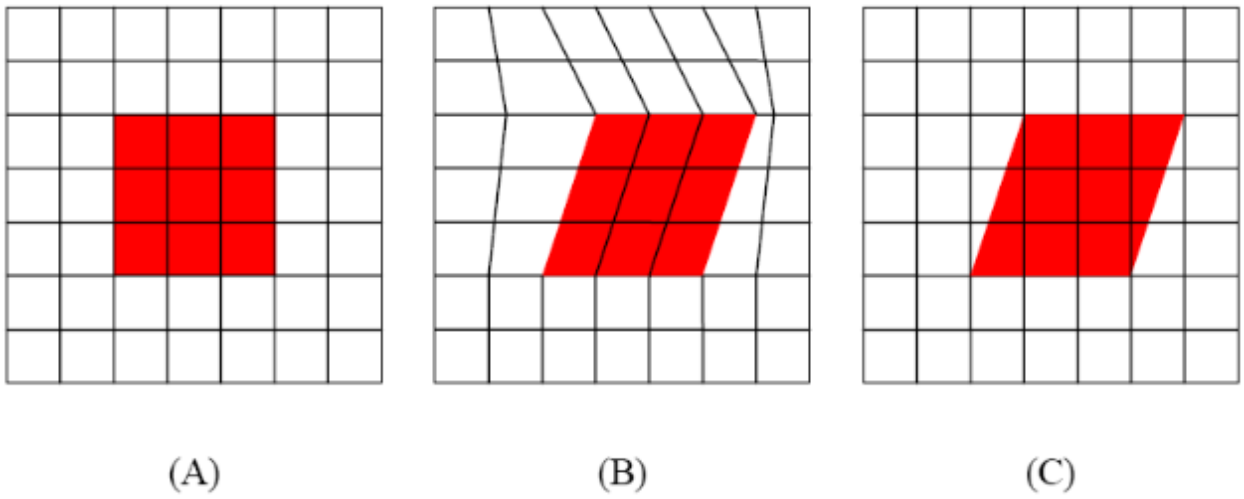

Figure 4-3 – ALE steps (A) Original mesh, (B) After Lagrangian Time Step, (C) Advection [Adapted from Greer, 2006]

In the advection phase the transportation of mass, momentum, and energy across the element boundaries computed using the following transport equations:

Advection transport phase $$\frac{\partial \varphi}{\partial t} + \vec{c} * grad(\varphi) = 0$$ *Equation 4-2 [Alia, 2006]*

$$\varphi(\vec{x}, 0) = \varphi_0(x)$$

Where:

φ = *Mass, momentum, or energy*
$\vec{x}$ = *ALE coordinate*
$\vec{c}$ = $\vec{v} - \vec{w}$: *Convective velocity*
$\vec{v}$= *Fluid velocity*
$\vec{w}$= *Mesh velocity*
$\varphi_0(x)$= *Initial condition of advection step from the solution of the Lagrangian step*

The hyperbolic Equation 4-2 can be solved at the face of an element using a second order Van Leer advection algorithm with the monotonicity condition relaxed to better preserve the explosive material interface [Hallquist, 2006].

In the ALE formulation material can only flow out the flat sides of the elements and cannot flow through the corners in a diagonal fashion, the diagonal flow is placed back into the original element (Figure 4-4), [Souli, 2004]. Consquently ALE meshes must be designed for the main flow of material to progress through the elements edges and not on a diagonal. Also the mesh size of any structure intended for fluid structure interaction with the ALE mesh must be of comparable size to that of the ALE mesh to properly transfer momentum and energy.

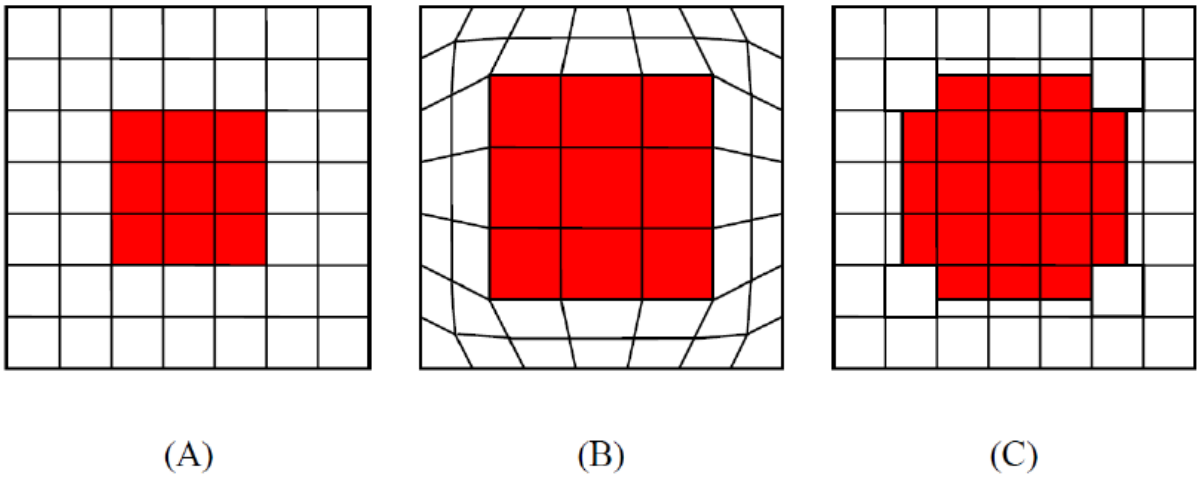

Figure 4-4 – Isometric advection of state variables in ALE algorithm: A) Initial configuration; B) After Lagrangian time step; C) After ALE advection and remapping [Greer, 2006]

4.2.1 Hydrostatic Locking in Tetrahedral Meshes

Using tetrahedral elements to mesh complex shapes allows for a less time consuming and less computationally expensive method of discretizing the problem compared to hexahedral elements; however, tetrahedral elements are well known to exhibit hydrostatic locking. Hydrostatic or volumetric locking incorrectly predicts pressure and therefore affects the blast wave transmission through the mesh [Singh et al., 2013; Panzer et al., 2011; Bonet et al., 1998]. This locking is due to the fact that the volume of each element is required to remain nearly constant, thereby enforcing constraints into the motion of a mesh with insufficient degrees of freedom caused by the ratio between number of elements and nodes being typically more than 5 to 1 for tetrahedral meshes [Bonet et al., 1998]. Thus in this thesis only hexahedral FE meshes were considered valid to model blast dynamics and wave physics.

4.3 Validation and Verification of Finite Element Models

Numerical simulations need to be validated against experimental test cases to build confidence in the predictive capability of a model as well as to ensure that the accuracy and precision of a model falls within the required error corridor. A robust numerical model has a high level of agreement with multiple experimental cases for the variables the model has a capability of measuring. Validation is limited by what can be measured experimentally and restricted by what the model was intended to be used for. Verification is required to ensure the modeller is using the numerical code correctly and the model is running as expected. For each development stage of the modelling process small steps must be taken with increasing complexity and the results thoroughly inspected using a sensitivity analysis to ensure continuous validation and verification of the models robustness over the whole useful life of the model. The American Society of Mechanical Engineers (ASME) outlines this process in a flow chart, (Appendix A [ASME, 2006]).

The results in this thesis were validated both qualitatively and quantitatively using CORA cross correlation software (Partnership for Dummy Technology and Biomechanics, Ingolstadt, Germany). CORA cross-correlates two time-history signals to evaluate curve shape correlation, and area under the curve to give an overall cross-correlation rating between 0 and 1 which can be considered a quantitative assessment of the shape of the signal [Gehre, 2009].

4.3.1 Verifying Mesh Convergence

In high frequency modelling scenarios, a mesh that is sized too coarsely will produce erroneous results. In blast modelling the explosive shock wave, which should be modelled as a

discontinuity of pressure, density, and temperature, will spread out over several elements, and depending on the thickness of those elements the resulting peak pressure observed could be much lower than that of its experimental counterparts. This smearing of the shock wave is caused by the artificial bulk viscosity which is implemented in the explicit finite element model to allow the resolution of discontinuities that can arise from the compression of a material that exhibits increasing stiffness with decreasing volume (i.e. shock waves in air). To determine if a mesh is discretized to an acceptable level of convergence, a Richardson extrapolation was performed to extrapolate the numerical results, calculate the Grid Convergence Index (GCI), and determine the error caused by mesh sizing issues at various mesh resolutions.

Either two or three mesh sizes / densities can be used to calculate the GCI, but three mesh sizes gives a higher level of confidence. In order to perform a Richardson extrapolation, the order of convergence, p, must be known:

Order of convergence

$$p = \frac{ln\left(\frac{f_3 - f_2}{f_2 - f_1}\right)}{\ln(r)}$$

Equation 4-3

[Roache, 1998]

Where:

p = *Order of convergence*

f_3, f_2, f_1 = *Results for coarse, medium and fine meshes respectively*

r = *The grid refinement ratio $r = h_2/h_1$ which relates the two mesh sizes; for example: r = 2 when an element size is reduced by half globally from medium to fine meshes, and coarse to medium*

The error of the Richardson extrapolation can then be calculated as:

Error of the fine mesh

$$E_{12}(Fine\ Mesh) = \left(\frac{f_2 - f_1}{f_1}\right)/(r^p - 1)$$

Equation 4-4

[Roache, 1998]

To calculate the GCI the error must be modified by a factor of safety, F_s, which is based on experience and the number of meshes tested. Roache suggests a $F_s = 3$ for a two mesh convergence study and a $F_s = 1.25$ for the higher confidence level of a three mesh comparison [Roache, 1998].

Grid Convergence Index

$$GCI_{12} = F_s E_{12}$$

Equation 4-5
[Roache, 1998]

Grid Convergence Index fine to medium

$$GCI_{12} = F_s \left(\frac{f_2 - f_1}{f_1}\right) / (r^p - 1)$$

Equation 4-6
[Roache, 1998]

Grid Convergence Index medium to coarse

$$GCI_{23} = F_s \left(\frac{f_3 - f_2}{f_2}\right) / (r^p - 1)$$

Equation 4-7
[Roache, 1998]

The Richardson extrapolation, and the GCI assumes that the results must all exist in the asymptotic regime, that is, the solution with reduced mesh size is asymptotically approaching a given value, the asymptotic regime is considered appropriate if the following condition is met:

Asymptotic regime condition

$$GCI_{23} \approx r^p GCI_{12}$$

Equation 4-8
[Roache, 1998]

The Richardson extrapolation also allows for the estimation of a "zero" element size error solution, i.e. the result that would be predicted by a model with zero mesh thickness. This error is found by estimating the error of the fine mesh solution using the order of convergence, and is then added to the fine mesh solution to provide an estimate of the solution at a grid spacing / element size of 0.

Zero Mesh Error Estimate

$$f_{h=0} = f_1 + \left(\frac{f_1 - f_2}{r^p - 1}\right)$$

Equation 4-9
[Roache, 1998]

The acceptable level of error is left up to the researcher, and is controlled by variables such as computational ability vs. requirements, and mesh complexity. A parameter must be chosen for the GCI that is appropriate and significant for the sought results. The GCI does not account for errors caused by erroneous assumptions, incorrect boundary or initial conditions, material property errors, and errors in the implementation of the code.

4.4 Anthropomorphic Test Dummies for Blast Loading and Their FEM Counterparts

Numerical models, in conjunction with physical surrogates, impact experiments, and tissue mechanical properties can provide important insights into impact phenomena that are not easily measured experimentally or are too complex for simple mathematical calculations [Cronin, 2011]. As discussed in Chapter 4 many *in vivo* animal models have been tested; however more recently these experimental tests have been isolated to smaller mammals and require large amounts of scaling to yield results suitable to human injury criteria. Anthropomorphic Test Dummies (ATDs) have often been used as semi biofidelic human surrogates (a surrogate that closely resembles the response of the human body) in high impact scenarios such as pilot ejections, car crashes, rocket sled tests, or blast testing.

ATDs are designed to mimic relevant human characteristics including average body mass, size, energy absorption and dissipation and in this regard they have a varying level of biofidelity and frangibility (a surrogate that sustains damage similar to human tissues); they can also be outfitted with a multitude of gauges in order to measure accelerations, forces, and loadings to correlate with existing injury criteria [Nahum et al., 2002]. The development of ATDs has gone

through several iterations in order to give improved human impact response; the current accepted test device for frontal impacts is the Hybrid III (HIII) ATD family. The HIII family consists of a 5th percentile female, a 50th percentile male, a 95th percentile male, and one, three, six, and ten year old child dummies (Figure 4-5). There are other available dummies used to predict different impact scenarios, such as the World Side Impact Dummy [WorldSID, 2013] and it is important to note that ATDs are only valid for loading type and loading direction for which it is designed i.e. the HIII ATD does not have a biofidelic response in a side impact scenario.

Figure 4-5 – Hybrid III family [National Highway Traffic Safety Administration, 2013]

There are currently no commercially available ATDs with heads that are biofidelically frangible in a blast scenario though some are currently under development including the Blast-Induced Brain Injury Protection Evaluation Device (BI^2PED) being developed by the DRDC-Valcartier Personal Protection group [Ouellet et al., 2012]. The BI^2PED (Figure 4-6), is an experimental anthropomorphic model of the human head that has been developed replicating the geometrical and mechanical properties of the head with focus on the relevant structures of the head injury mechanics including: skin, skull, brain, CSF, as well as the falx and tentorium membranes. While this model has potential to perform biofidelically and give reliable testing methodologies it is still under development and has yet to be fully validated for explosive loading.

Figure 4-6 – BI^2PED Headform [Ouellet et al., 2012]

The Hybrid III has previously been used in several explosive studies as a human surrogate to determine blast loading conditions on the human body [Manseau et al., 2006; Desmoulin et al., 2009]. The HIII is only valid for frontal crashes and as such it should only be used in frontal blast scenarios, with their necks mimicking the human bodies bending response and limitations in flexion and extension. The skull and skull cap are one piece cast aluminum parts with removable vinyl skins. The neck is a segmented rubber and aluminum construction with a center cable [Humanetics, 2013].

Numerical surrogates have become more common with increased speed and decreased cost of computing coupled with improved multi-physic modelling techniques and material models [Schmitt et al. 2010; Yang, 2001]. LS-Dyna incorporates 2 built in ATDs, the HIII and the multi-body GEnerator Of Body Data (GEBOD). Currently the standing HIII FEM dummies available through LS-Dyna are not conducive to blast physics as they have mesh irregularities around their legs due to being designed as a sitting model for car crash scenarios. The motivation of this thesis is to predict global head kinematics and potential resultant injury, thus the HIII does not offer additional results to the GEBOD model (Figure 4-7), and this FEM ATD was used in this thesis to determine global blast kinematics.

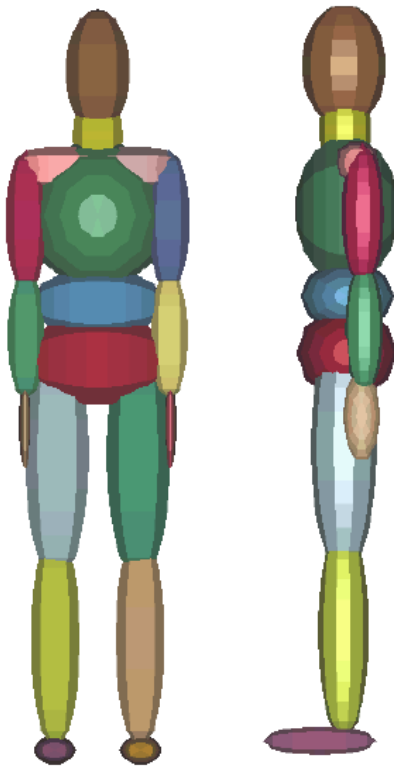

Figure 4-7 – The LS-Dyna GEnerator Of Body Data (GEBOD) multi-body model.

The GEBOD is made up of 17 rigid segments in the shapes of ellipsoids connected by fully articulated joints which are modelled as torsion springs with viscous stiffness and are representative of the joints in the human body [Cheng et al., 1994]. A major limitation to the GEBOD model is that the model is not frangible and thus parts will not fail or break under stress as the human body would.

5 Modelling Blast Events and Interaction with the Human Body

FEM has been used extensively in the automotive and sports injury fields, and with the introduction of multi-physics explicit formulations it is becoming an increasingly popular method for studying blast scenarios and human injury response. This method can provide important insights into impact phenomena allowing a researcher to see features of the problem that cannot be thoroughly observed in experimental tests. Some of the first FEM models used to study blast injury were developed at the University of Waterloo [Cronin et al. 2004], and were used specifically to study the injury response of a blast wave impinging upon an unprotected thorax. With the increase in survivability from pulmonary injuries due to more effective modern body armour [Wood et al., 2012], the increase in size and usage of enemy explosives, and the increased awareness in the medical field of diagnosing mild traumatic brain injury (mTBI) [Warden et al., 2005] there has been an increase in blast related brain injuries, prompting further research using FE models to determine the effect of overpressure on the kinematics of the human head, and the internal response of the brain [Haladuick et al., 2012; Singh et al., 2013; Panzer et al., 2012; Ganpule et al. 2013; Lockhart et al., 2011].

Blast modeling is an extremely complex fluid structure interaction problem; it is a high stress, high strain rate phenomenon that requires suitable mesh discretization to accurately represent the short wave lengths of a blast event. This chapter will focus on the different modeling approaches that were developed for this thesis to model blast events including how they were developed, initialized, controlled as well as the benefits and caveats of each.

5.1 Enhanced Blast Uncoupled Method

The finite element software LS-Dyna has a built in function to apply blast loading to structures using a *LOAD_BLAST_ENHANCED (LBE) keyword. This method utilizes a version of conventional weapons (ConWep) equations [Hyde, 1998] and applies the blast to the outward facing normals of a defined structure; this method was previously validated by Lockhart *et al.* [Lockhart et al., 2011]. ConWep is a database that creates pressure time histories at a given standoff distance from a defined charge by utilizing curve fits and calcualtions based on empirical blast data produced by the US Army [Kingery, 1966]. LBE defines an air blast function via application of pressure loads resulting from the detonation of a conventional explosive [LSTC, 2010], based on the equivalent mass of TNT, the coordinate of explosive charge center, and a defined ground plane. This approach utilizes incident pressure and simulates perfect reflective surfaces to give reflected pressure, ground reflection, as well as Mach stem effects to apply the blast shock wave to a target by simulating a rapid increase in pressure, and density. The ConWep databse is only valid for mid to far field distances and scaled HOB aove 100 $ft/lbm^{1/3}$; it determines values for free field blast and does not give values for ground reflection or Mach stem effects, thus is missing important modelling aspects in lower HOB scenrios which is why the LBE is used for simulation [Kingery, 1966].

Using an uncoupled fluid structure model offers computational time savings when compared to fully coupled solutions. The major disadvantage to using uncoupled FSI models is the reduced accuracy of loading due to the uncomplete modelling of the whole scenerio and lack of coupling between a fluid mesh and the structure. The LBE method assumes a planer blast wave which is inaccurate in the near field where a blast wave is spherical. There in no observatble 3D

interaction with the surronding air, expanding shockwave, or explosive fireball as there is no interaction between a fluid mesh and structure interface. Using this keyword one can only analyze the target subject, the explosive is simply defined as a point in space and the surronding environment is assumed to be air at Stnadard Temperature and Pressure (STP). The LBE method calculates how an ideal blast pressure force would be transmitted to the subject; however, one cannot visualize the interaction of the subject with the pressure wave or the interaction of the pressure wave and the ground. This model neglects the 3D effects of the pressure wave reflecting and wrapping around a subject and the importance that may bear in analyzing explosive damage. The enhanced blast function is also only valid for certain scaled heights of bursts (0.054 $m/kg^{1/3}$ to 40$m/kg^{1/3}$) [LSTC, 2008]; all simulations were performed within the valid range.

All models used in this thesis to calculate blast injury response use the GEnerator Of Body Data multi-body model (GEBOD) as their human surrogate to calcualte global head kinematics. Figure 5-1 shows the LBE model with the GEBOD in place with a defined standoff, lateral offset, ground plane, and explosive: center of mass, location, and size.

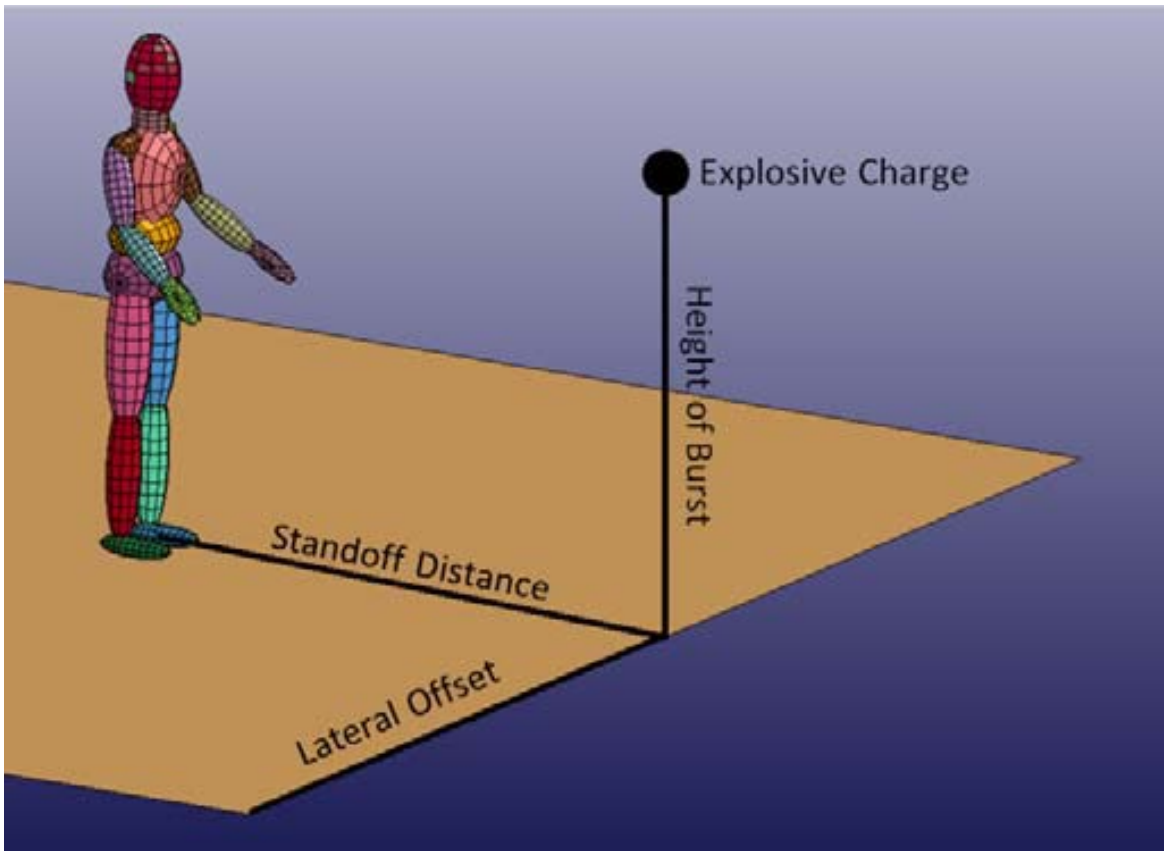

Figure 5-1 – LBE model initial setup with GEBOD.

5.2 Coupled ALE Modelling of an Explosive

An improved method of modelling an explosive incident is to model the entire event including: the detonation wave of the explosive material, the resultant shock wave expansion into the surrounding medium, and the interaction of the fluid structure interface. Using the JWL EOS to control the explosive material detonation and expansion, the ideal gas law EOS for the surrounding air, and Lagrangian-Eularian contact algorithms for the shock wave ground reflections and target interaction, an explosive incident can be comprehensively modelled from start to finish. To model an incident with a high level of accuracy there must be a high mesh resolution in and around the explosive charge to properly resolve the JWL equation of state and

control the explosive products expansion. The target and surrounding ALE mesh must also have a similar mesh size to allow for adequate coupling.

5.2.1 Shock Tube Model

A shock tube model was developed to verify the current version of LS-Dyna has appropriate ALE controls to model and resolve a shock wave problem, and to show the importance of mesh density (element size) on shock wave transmission modelling.

5.2.1.1 Model Geometry and Boundary Conditions

Mesh densities of (0.01 m, 0.005 m, 0.0025 m, 0.001 m) were investigated to determine the effect that element size has on shock transmission, tests were also performed to find the most stable version of control cards to use for ALE shock wave problems. 3d, 2d, and 1d models were tested and gave identical results for each respective mesh density scenario. The coupled ALE blast models are 3d cases using symmetry planes to reduce the required number of elements, for this reason it was important to ensure the results in the 1d, 2d, and 3d cases were indistinguishable and the symmetry planes resolved the problem accurately. In all simulations the model was constrained using single point constraints on each of the nodes on the outer surface of the mesh to stop out of plane motion; the constraints were set to stop any motion in the direction of the outer normal face of the element i.e. the nodes on top and bottom were not able to move in the Y direction but were free in the X and Z directions, and the nodes at the front and back were constrained in the Z direction but not in the Y and X. The nodes at each end were constrained in the X direction creating a reflecting surface, and as such the analysis was only valid until the shock or expansion waves reached either the left or right boundaries.

5.2.1.2 Model Initial Conditions

Table 5-1 – Material properties and mesh conditions for initial shock tube setup.

Material Properties	Element Size	Element Type	Number of Elements		
			1D	2D	3D
Initial *Driver* Gas - Air					
CV=718					
CP=1005					
γ=1.4					
ρ=3.879 kg/m^3	10 mm	Hex.	100	1000	10000
P=304 000 Pa	5 mm	Hex.	200	4000	80000
Initial *Driven* Gas - Air	2.5 mm	Hex.	400	16000	640000
CV=718	1.25 mm	Hex.	800	64000	5120000
CP=1005					
γ=1.4					
ρ=1.293 kg/m^3					
P=101 325 Pa					

Using Equation 2-16 to Equation 2-25 with the initial conditions described, (Table 5-1, Figure 5-2), analytical calculations were used to describe the shock tube pressure profile at any specific time after diaphragm rupture, these calculations can then be compared to the numerically simulated result at the same time step.

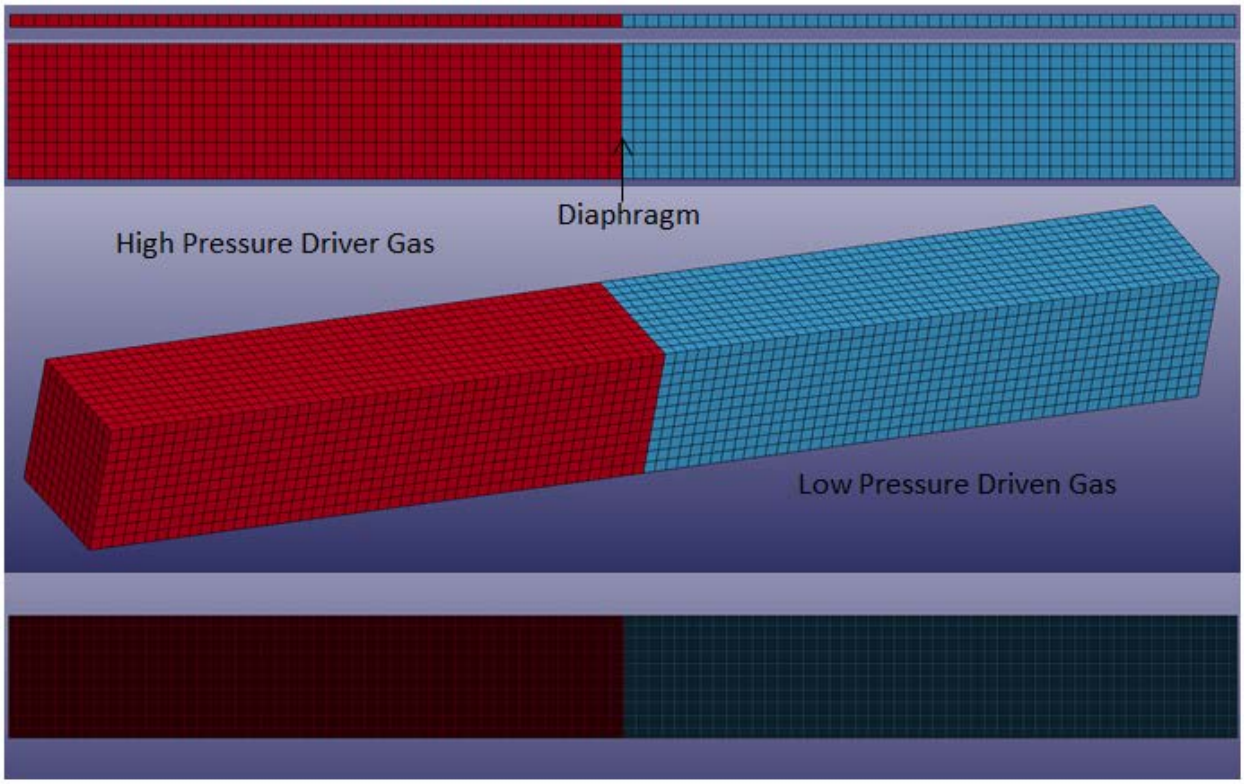

Figure 5-2 – Initial conditions of 1 m shock tube showing the high pressure driver gas and the and low pressure driven gas for the 1D, 2D, and 3D cases of the 1cm mesh and the 2D 1.25 mm mesh.

5.2.1.3 Model Results

Due to the fact that the shock tube model was used to develop the ALE formulation that was used in the blast model, the results found during the shock tube study will be presented here as a part of the model development. At a time of t=0.0005 s after diaphragm rupture the model has the following pressure distribution shown as a 2D numerical simulation model pressure composition, (Figure 5-3), and as a pressure vs. distance chart with the diaphragm placed at 0.5 m (center of shock tube) (Figure 5-4).

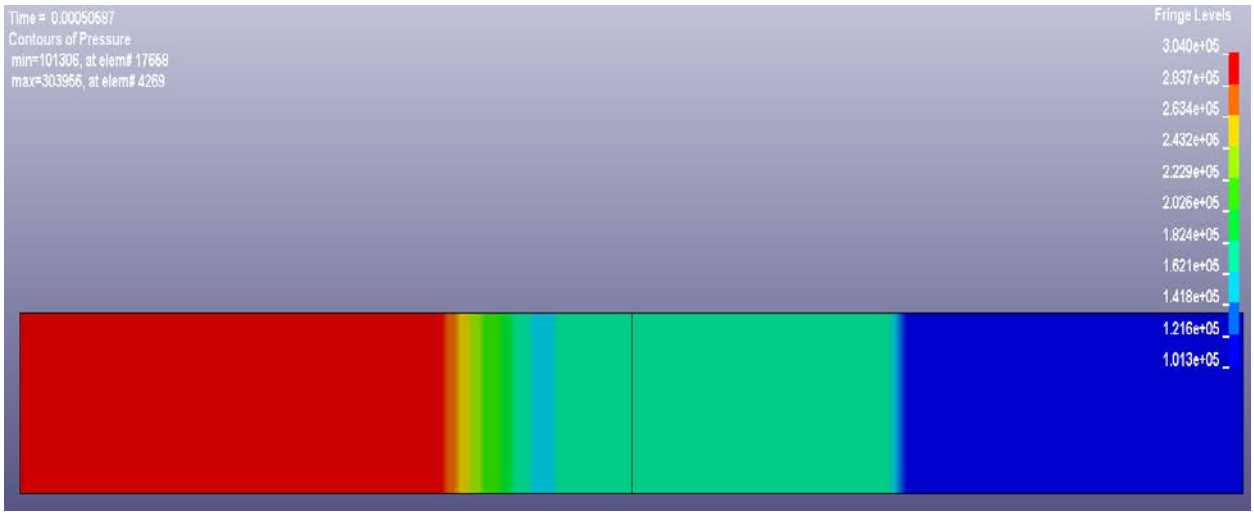

Figure 5-3 – Numerical model showing shock tube shock wave (right) and expansion wave (left).

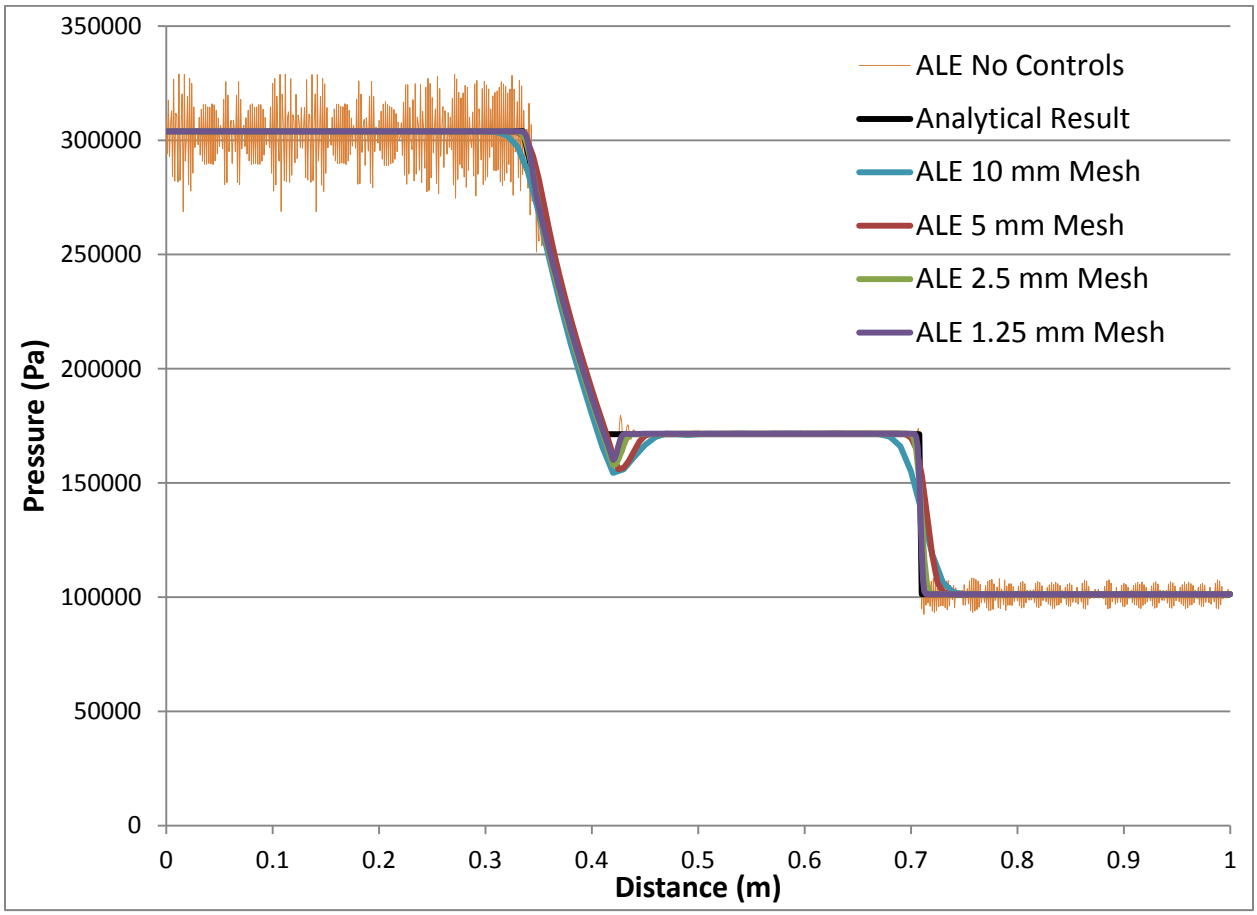

Figure 5-4 – Pressure vs. Distance for 1 m shock tube at time = 0.0005 s after diaphragm rupture.

Simulation of waves in a shock tube was previously investigated in a similar study by Salisbury et al. using a different LS-Dyna solver [Salisbury et al., 2004]. It was determined in this study that a hexagonal mesh size less than 5 mm is convergent in shock wave problems.

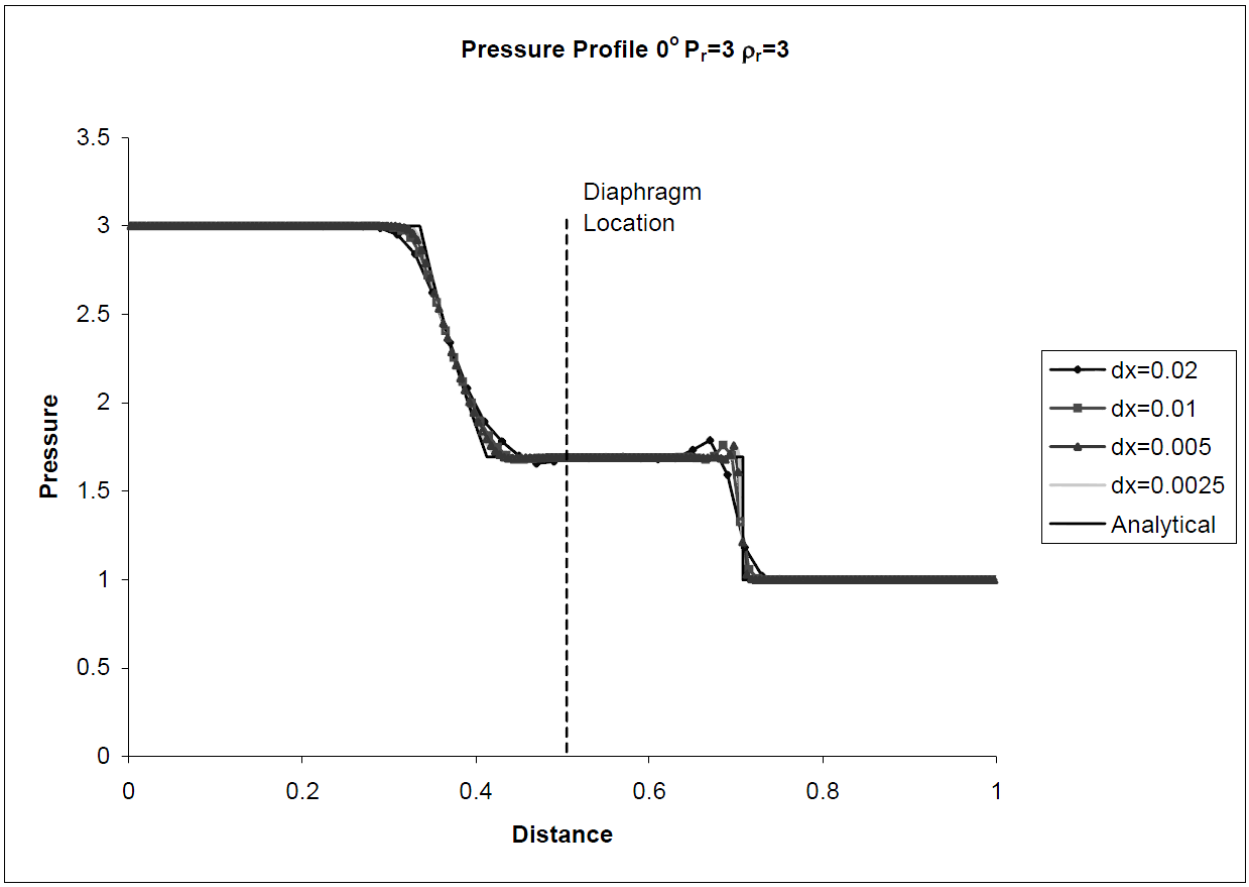

Figure 5-5 – Pressure vs Distance for 1 m shock tube at time=0.0005 s after diaphragm rupture [Salisbury et al., 2004].

It can be seen by the comparison with both the analytical calculation and with the research previously completed by Salisbury et al. that holistically LS-Dyna was able to resolve shock wave problems when the correct controls and mesh density were used. The following two figures show the expansion wave and shock wave in more detail and allow for further statements on the validity of using ALE in LS-Dyna to solve shock wave problems in air.

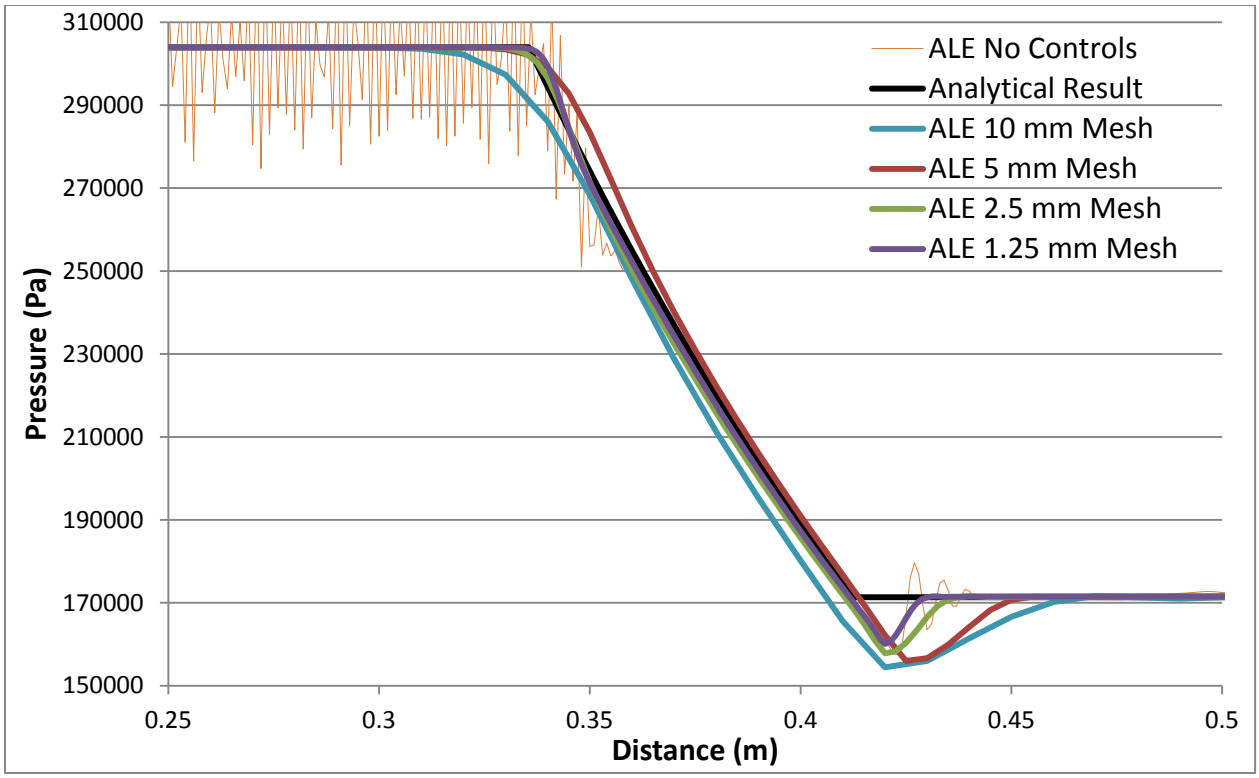

Figure 5-6 – Expansion wave pressure profile at t=0.0005 s.

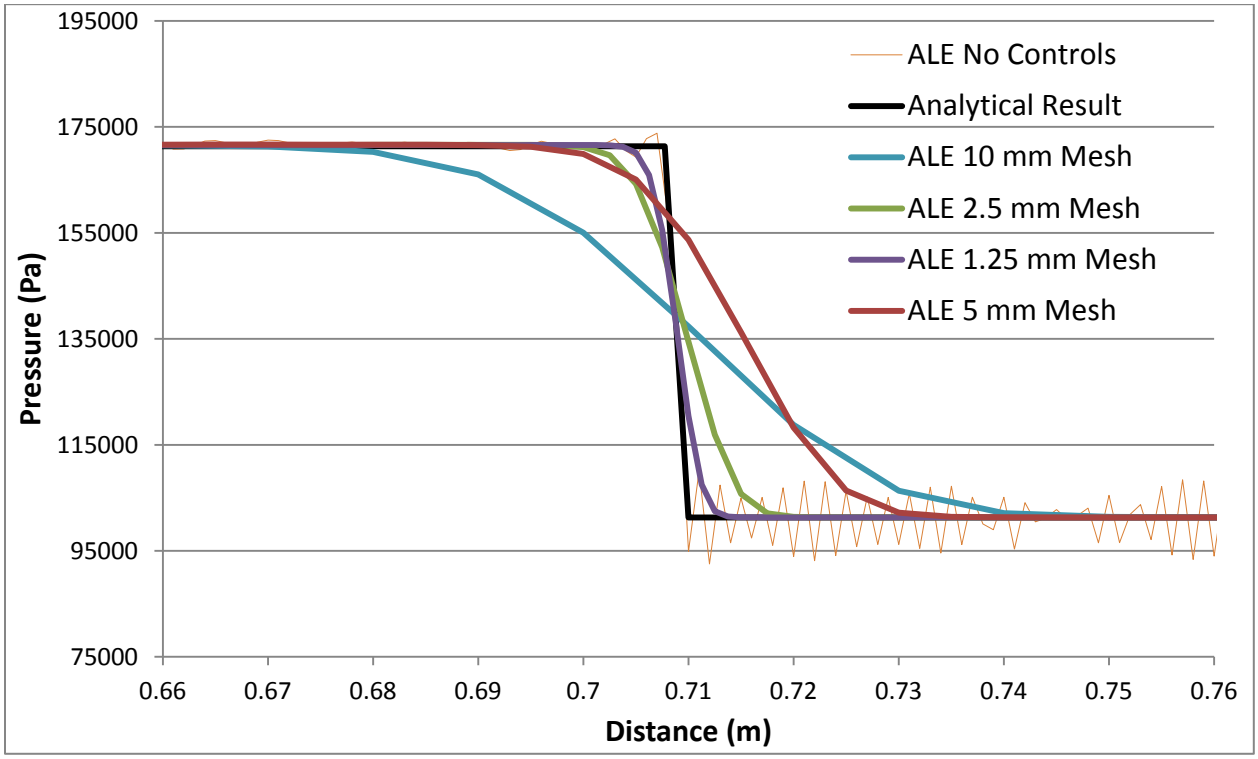

Figure 5-7 – Shock wave pressure profile at t=0.0005 s.

The above figures show that as the mesh resolution increases the accuracy of the model also increases, following the theoretical solution with higher precision. The mesh with no ALE control cards has a great degree of variation as the model is not properly stabilized using proper continuum treatment, (Van Leer second order advection and artificial bulk viscosity). Artificial bulk viscosity is implemented in explicit finite element code to allow the resolution of discontinuities that can arise from the compression of a material that exhibits increasing stiffness with decreasing volume (i.e. shock waves in air). The use of an artificial viscosity in numerical codes allows the solution of problems involving shock-waves without producing spurious, high frequency oscillations in the shocked region that can be seen in the above results [Meyers, 1994]. Unless otherwise stated the default bulk viscosity used in this thesis is 1.6 and 0.5, which are defaults in LS-Dyna [LSTC, 2010].

In all analyses the shock wave can be seen to spread out or smear over a finite distance, (Table 5-2), this distance is directly related to the mesh density; though realistic shock waves do have a finite distance associated with their wave dynamics it is relatively small compared to the mesh sizes tested and thus the shock front is generally treated as a discontinuity. With a higher mesh resolution the shock wave is smeared over a linearly smaller distance and would more accurately resolve the peak pressures of a blast wave when modelling blast dynamics in ALE.

Table 5-2 – Mesh density and resultant shock wave smearing.

Mesh density	Total Distance of Shock Wave Smearing	Number of Elements Shock Wave Smeared Across
10 mm	80 mm	8
5 mm	40 mm	8
2.5 mm	20 mm	8
1.25 mm	10 mm	8

5.2.1.4 Discussion

The difference in the results from the models with a mesh density less than 5 mm was minimal when analyzing the shock wave front and the expansion waves, this indicates convergence and thus meshed elements sized below 5 mm will converge and enable analysis of an ALE shock wave problem in air using LS-Dyna. Using smaller elements produced less shock wave smearing which garners higher accuracy in a blast physics model, thus in this thesis the smallest element size that can be utilized without being computationally prohibitive will be used to gain reliable results.

5.2.2 Spherical Mesh Geometry Development

In order to create a spherical shock front the mesh must have a spherical geometry and diverge from the center of mass of the explosive charge, (Figure 5-8). This is necessary to prevent the distortion of the ALE advection algorithm as material only moves normal to the element surface as described in Chapter 4.2. The detonation point is located at the center of mass of the explosive material, and the detonation wave propagates outward from that point at the detonation velocity of the explosive in accordance with the JWL EOS, as the explosive expands in the air medium it forms a shock wave.

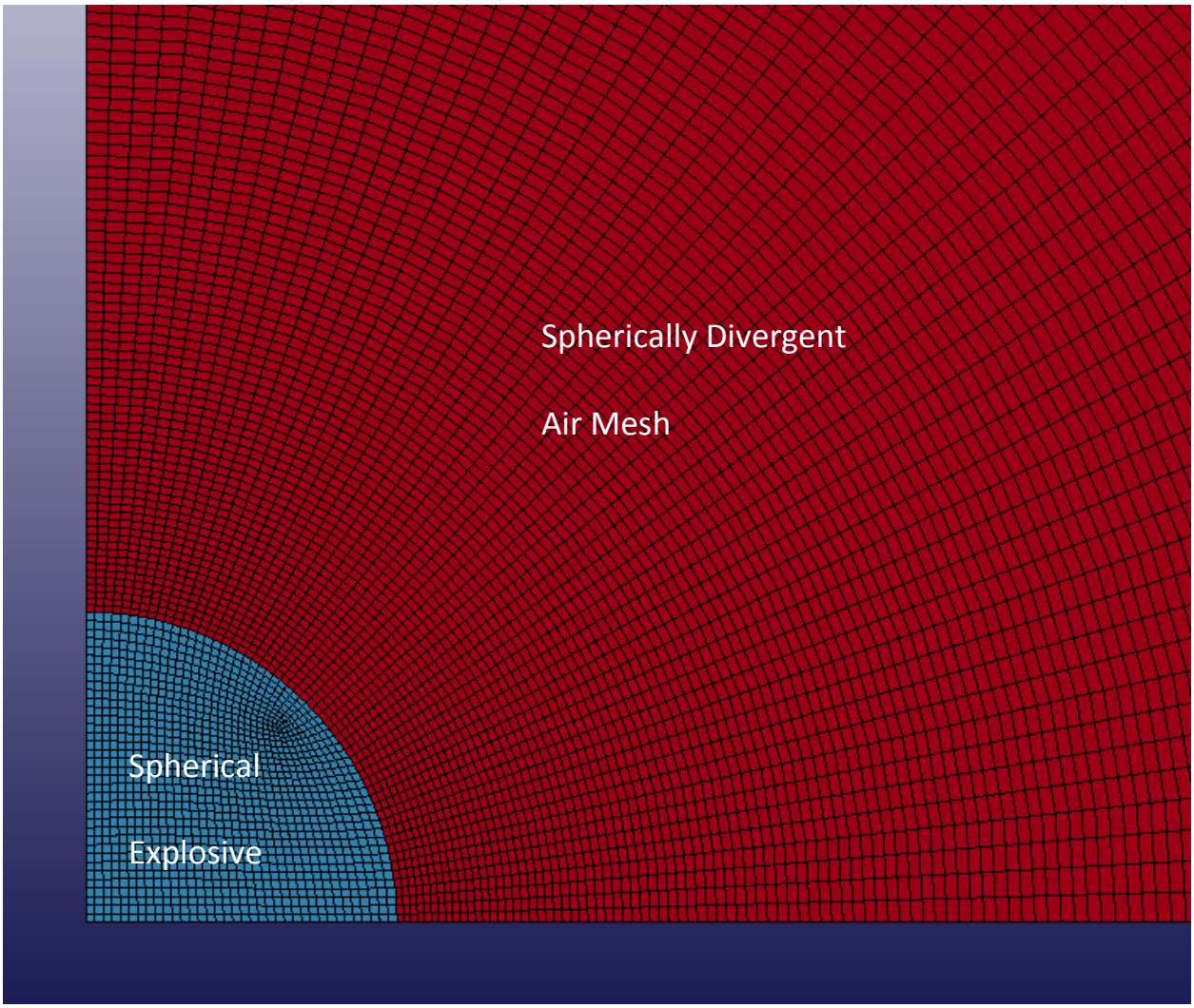

Figure 5-8 – Spherical mesh diverging from the center of mass of the explosive charge.

The nodes between the explosive charge and the air were shared to properly transfer the expansion energy of the explosive ALE material to the air. The mesh must not diverge in size too quickly or the accuracy of the model will suffer, thus only a small length bias (approximately 10%) can be used as the mesh diverges from the explosive, this model uses a length bias of 4%.

The ground was meshed as a rigid solid to reflect the blast wave. It was modelled using shell elements and constrained in the model as a Lagrangian part (Figure 5-9).

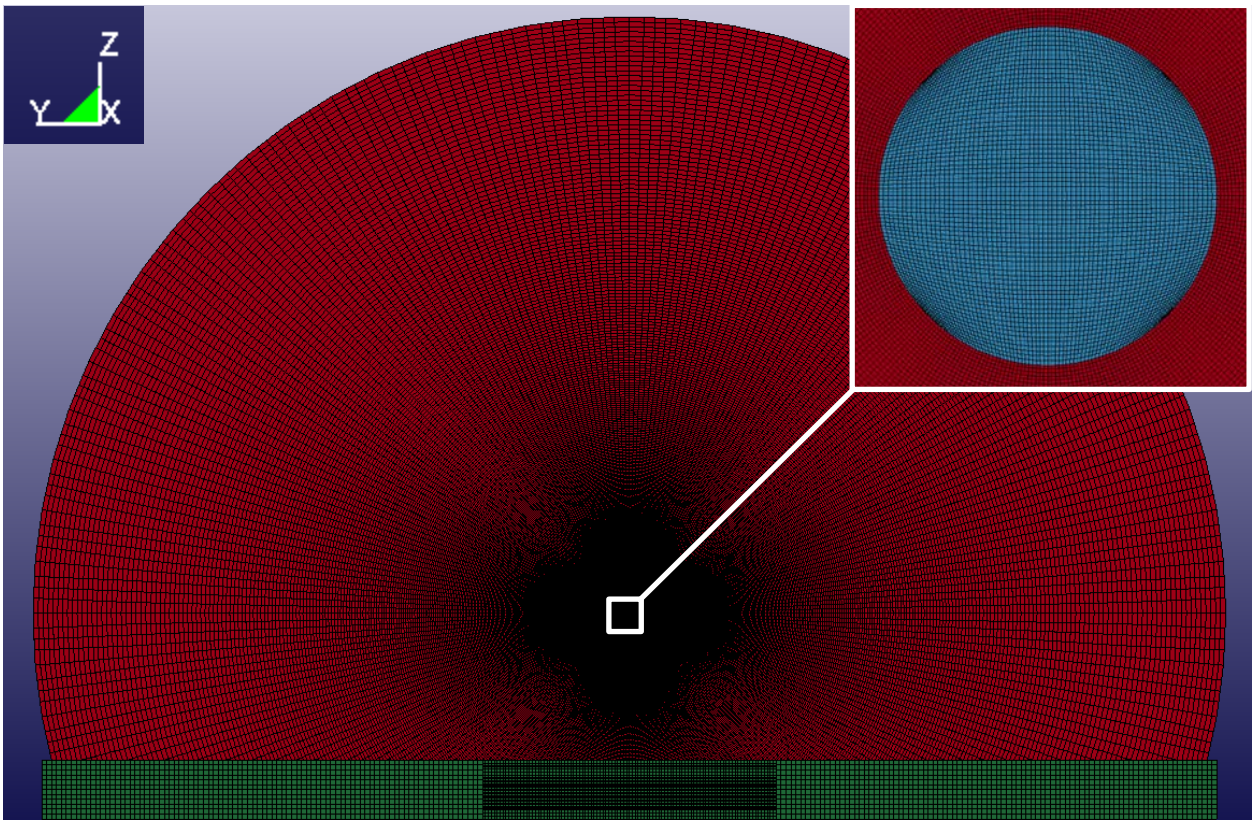

Figure 5-9 – ALE model geometry including ground mesh.

The spherical model had a plane of symmetry on the back edge of the explosive to form a half model. The mesh was constrained in the X direction using single point constraints in order to create a plane of symmetry and force the detonation propagation of half the mass of the explosive in the direction of the ALE mesh, the model could be expanded to a whole explosive, but would require twice the amount of elements and thus double the computational cost. The model had a radius of 6 m to enable fluid structure interaction within 5 m of the explosive without the pressure wave reaching the outer boundary of the mesh and reflecting.

To decrease the mass of explosive used in the ALE model the whole model would have to be scaled down to the required explosive volume size, this is required to maintain the accuracy of

the detonation across the explosive charge. Whereas to increase the size of the explosive the air elements directly surrounding the explosive charge should be changed from tehir air ALE part to the explosive ALE part to give the required charge size; the mesh should not be scaled up as this would increase the element size and thus decrease the model accuracy. If a larger air ALE mesh is required, the elements on the outside of the sphere have to be extruded via solid face offsetting.

A second geometry was attempted to try and produce better fluid structure interaction at the ground by sharing the nodes between the ALE air mesh and the ground, (Figure 5-10). This mesh produced a non-spherical shock wave expansion as the mesh flattened the shock wave leaving the bottom of the explosive charge, and as such this geometry was abandoned.

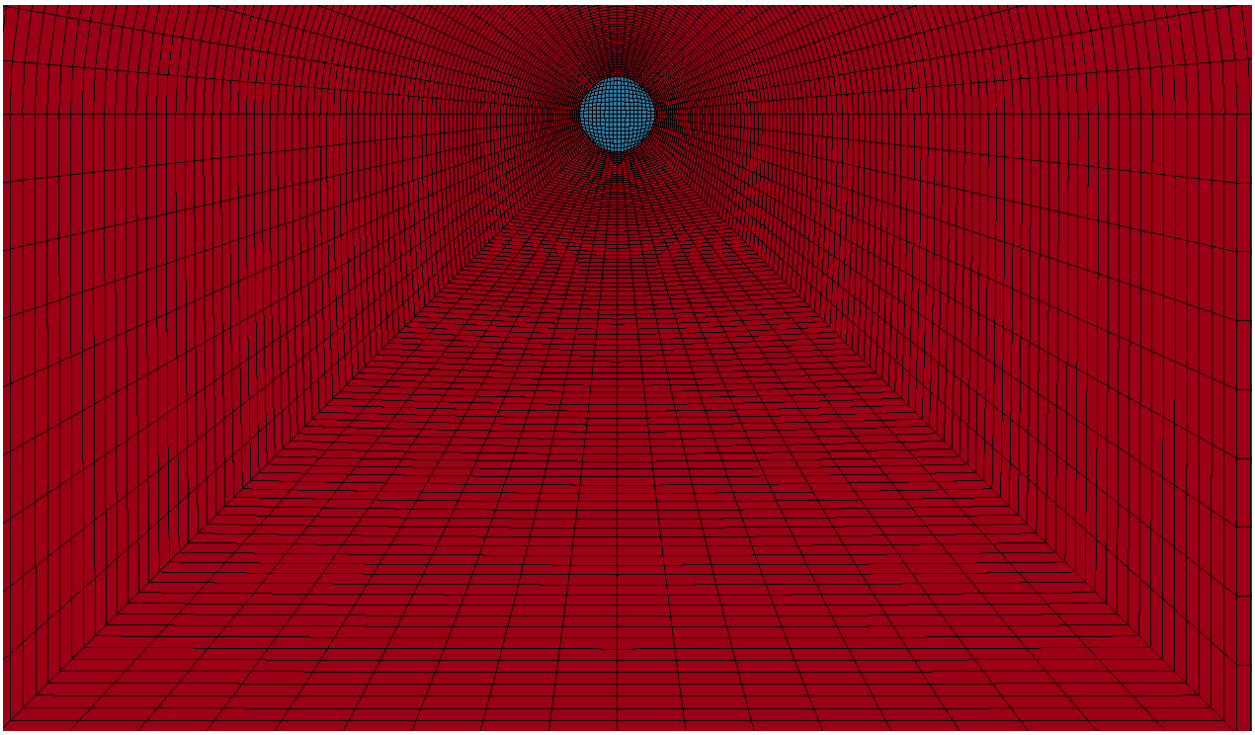

Figure 5-10 – Non spherically divergent mesh used to meet the ground in a planer fashion.

5.2.2.1 Mesh Refinement

To determine if the mesh density used in the ALE model was fine enough, a grid convergence study was undertaken using Richardson extrapolation to calculate the GCI as described in section 4.3.1 [Roache, 1998]. For this study the characteristic length of a side of an element in the center of the explosive charge was chosen to determine the mesh size ratio, the lengths were: 10 mm, 5 mm and 2.5 mm.The model was run under the same loading and boundary conditions, with the arrival time and peak pressure monitored at 3.5 m and 4 m. The peak pressure is an important parameter to measure, as previously described if a mesh is too coarse the peak of the shock wave will spread out over several elements and the peak pressure will be lower. This phenomenon can be seen in the Figure 5-11 with the 10 mm mesh having a similar impulse force but a much different peak overpressure value compared to the 2.5 mm mesh. The impulse force in all mesh sizes tended to stay relatively the same for the same applied loading conditions, this is due to the conservation of energy; in shock wave physics though the peak pressure is reduced in a coarse mesh the impulse force remains relatively the same due to the spreading of the shock front over a longer time interval. Thus although the impulse force of a blast wave is an important parameter in this study it is not appropriate measure to determine mesh convergence.

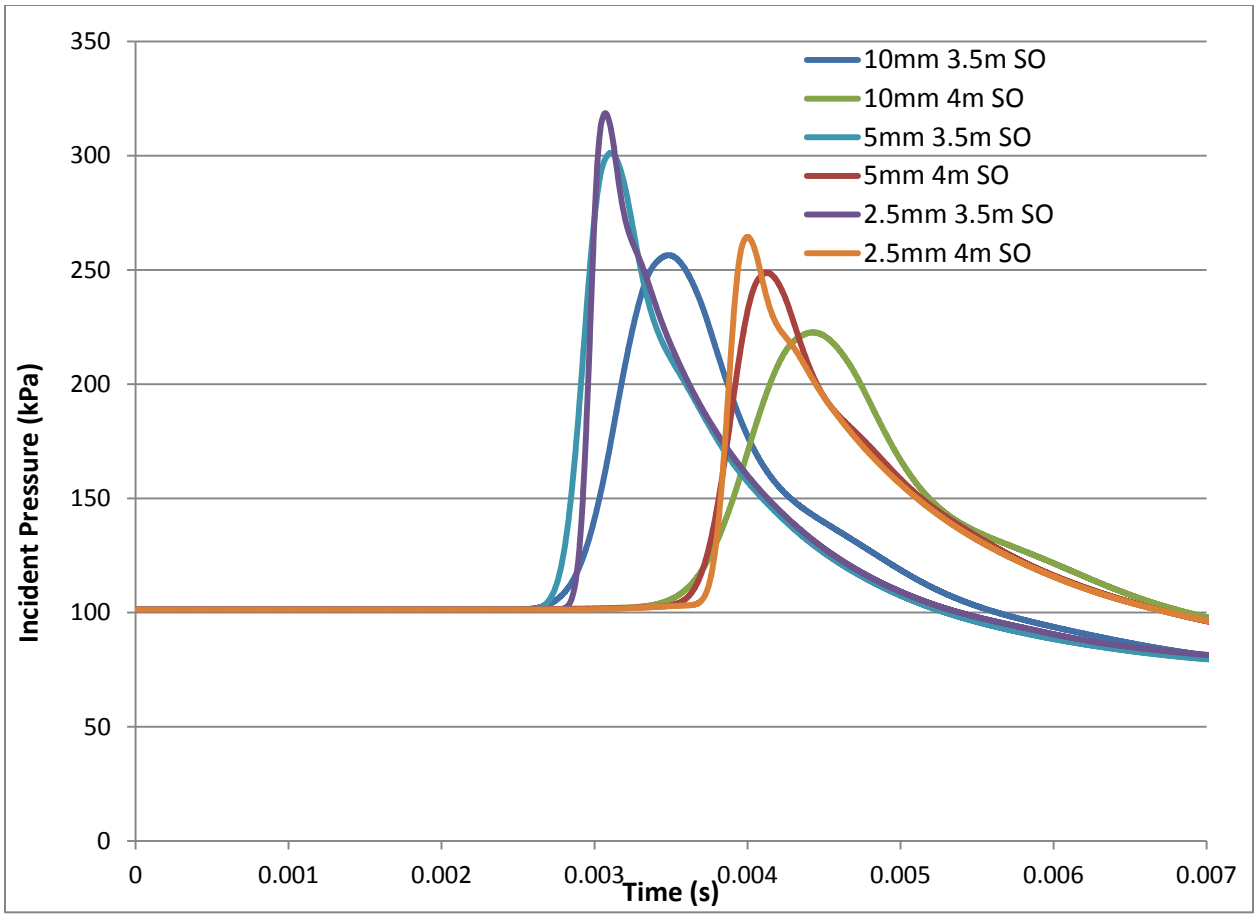

Figure 5-11 – Mesh refinement of a 5 kg C4 charge at 3.5 m and 4 m standoff (SO) distances.

Table 5-3 – GCI calculation for peak pressure and arrival time.

Mesh	*Total Number of Elements*	Peak Pressure (kPa)		Arrival Time (s)	
		3.5 m Standoff	*4 m Standoff*	*3.5 m Standoff*	*4 m Standoff*
10 mm	70168	255	221	0.00350	0.00440
5 mm	561344	300	247	0.00310	0.00410
2.5 mm	4490752	317	263	0.00310	0.00400
GCI_{12}		-4.07%	-12.2%	0.0900%	4.52%
GCI_{23}		-11.4%	-21.1%	1.26%	8.93%
$r^p GCI_{12}$		-10.8%	-19.8%	1.28%	0.810%
Zero Mesh		327	289	0.00310	0.00380

All experimental blast scenarios have a certain level of uncertainty, there is a corridor in which measurements and results are deemed acceptable. The GCI calculated for the fine mesh has an acceptable level of error to continue with the model using a baseline element size of 2.5 mm for the explosive center; this mesh size is also in agreement with the shock tube mesh resolution study undertaken in section 5.2.1 and gives convergent results for an ALE shock wave.

With this level of mesh resolution the spherical ALE mesh required 4619524 elements and 4667670 nodes including the shell elements in the floor. Resolving a model with this many elements is extremely computationally expensive and requires run times of up to two weeks to simulate the 6m radius model on an Intel 990X twelve core dual threaded processor.

5.2.3 Cylindrical Mesh Development

The shape of an explosive charge can drastically change the wave-dynamics in the near-field and mid-field regions of a blast incident. The trials carried out by DRDC-Valcartier were cylindrical in nature with a 1/1 Length to Diameter ratio. The blast wave propagating perpendicular to the axis of the cylindrical charge is governed by cylindrical expansion. The cylindrical model was extruded from one of the sides of the spherical model to give a cylindrically divergent mesh, diverging from the axis of symmetry of the cylindrical charge (Figure 5-12). The mesh density was very high near the explosive and is then biased with a length bias rate of 5% (Figure 5-13).

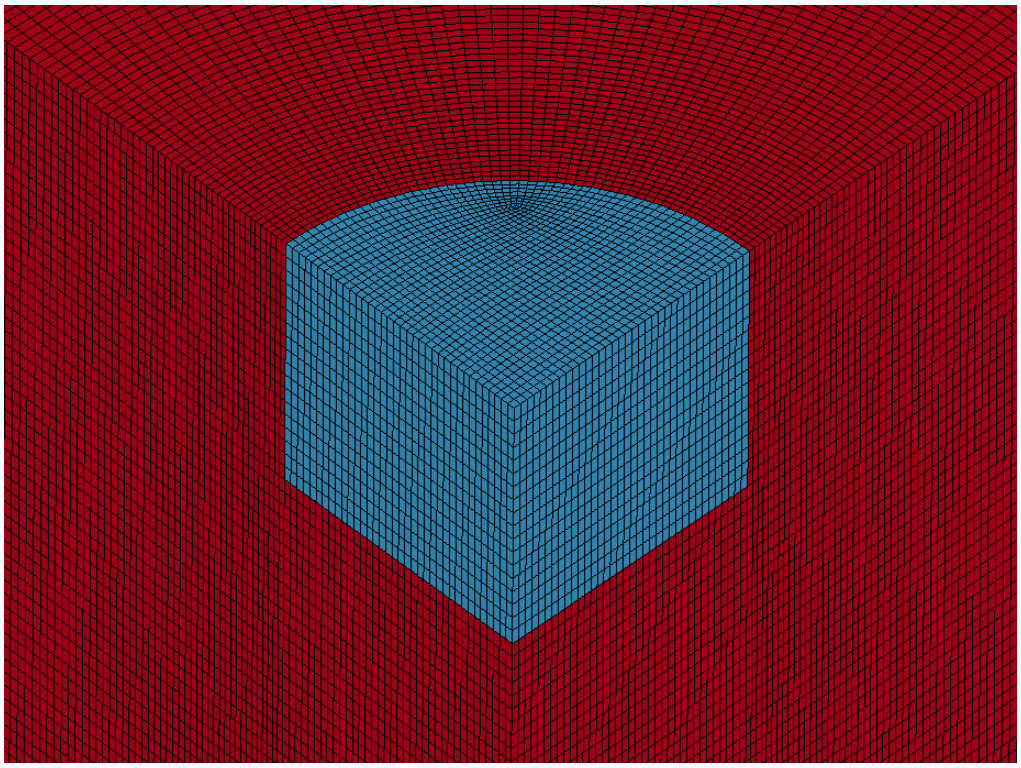

Figure 5-12 – Cylindrical mesh diverging from the axis of symmetry of the cylindrical charge.

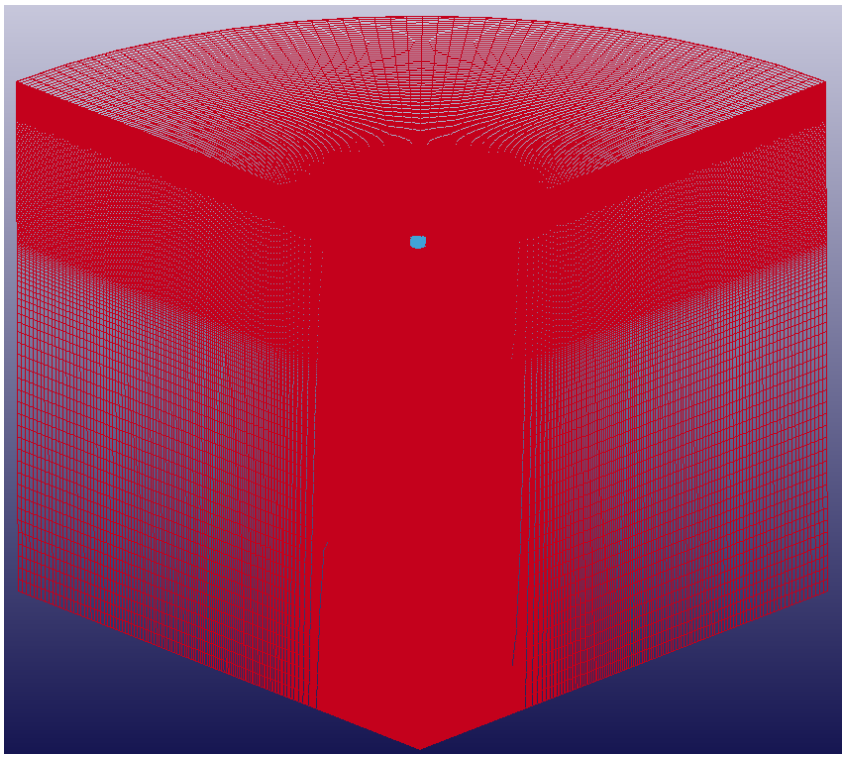

Figure 5-13 – Full view of cylindrical 1/8th model.

The mesh side that was extruded was scaled from 2.5 mm to 2.2 mm in order to give the explosive radius required for a 1/1 Length to diameter ratio for the cylindrical charge. This model required an ALE mesh of 4242336 elements and 4347515 nodes for a 1/8th symmetric model.

5.2.4 Important ALE Model Parameters

Explicit finite element programs use control cards to process model geometry, material properties, equations of state, and control the algorithms of the solver. The solver used for these models was LS-Dynas ls971_d_R6.1.1_80542_win64_p.exe, this solver uses double precision to incur less round off errors for the large number of computational cycles in the model giving a higher level of accuracy.

The air was modelled using a null material model with a linear polynomial equation of state representing the ideal gas law:

Linear Polynomial EOS $$P = C_0 + C_1\mu + C_2\mu^2 + C_3\mu^3 + E(C_4 + C_5\mu + C_6\mu^2)$$ *Equation 5-1 [Alia, 2006]*

Where:

μ= $\frac{\rho}{\rho_0} - 1$

E = *Specific internal energy (units of pressure)*

For an ideal gas the equation was reduced using the appropriate coefficients:

Ideal Gas Coefficients $$C_0 = C_1 = C_2 = C_3 = C_6 = 0 \; and \; C_4 = C_5 = \gamma - 1$$ *Equation 5-2 [Alia, 2006]*

Thus:

Linear Polynomial Ideal Gas EOS

$$P = E(C_4 + C_5\mu) = (\gamma - 1)\frac{\rho}{\rho_0}E$$

Equation 5-3

[Alia, 2006]

To give an initial ambient pressure of 101.3 kPa for air:

γ= 1.4
E0 = 2.53E5 Pa
ρ_0 = 1.293 kg/m^3

The explosive was modelled using a solid ALE material model using a high explosive burn control card to define the explosive material properties, for C4 the material properties are as follows:

Table 5-4 – Material properties for C4 explosive [Dobratz, 1981].

Density	Explosive Detonation Velocity	Chapman-Jouget Pressure
1601 kg/m^3	8193 m/s	2.81E10 Pa

The detonation of the C4 is controlled by the JWL equation of sate:

JWL EOS:

$$P = A\left(1 - \frac{\omega}{R_1 V}\right)e^{-R_1 V} + B\left(1 - \frac{\omega}{R_2 V}\right)e^{-R_2 V} + \frac{\omega}{V}E$$

Equation 5-4

[Dobratz, 1981]

The coefficients of the JWL equation are described in Chapter 2.3, for C4 the values of the JWL coefficients are:

Table 5-5 – JWL EOS coefficient values for C4 [Dobratz, 1981].

A	B	R1	R2	ω	E0	V0
6.10E+11	1.30E+10	4	1.4	0.25	0.90E+10	1

The floor and GEBOD were constrained as Lagrangian parts in an ALE mesh and initialized using initial volume fraction methods. These control cards describe the penalty coupling of the fluid structure interface and the initial conditions of the slave Lagrangian structures in the master ALE mesh.

6 Results

This chapter describes and compares the results of all the developed numerical models to experimental data provided by the Defense Research and Development Canada – Valcartier and experimental Conventional Weapons (ConWep) curves. Pressure, head kinematics, and HIC results were validated against 5 kg C4 blasts scenarios with 3.5 m, 4 m, and 5 m standoffs at differing heights of burst to provide verification of the models robustness.

6.1 Analytical Pressure Calculations

The equations described in chapter 2.3 were used to calculate the maximum pressure produced in a blast environment for 5 kg C4 charges with standoff distances of 3.5 m, 4 m, and 5 m.

Assuming a spherical charge shape, a free air blast, and an ambient pressure of 101.3 kPa:

$$\frac{C4}{TNT} Pressure\ Equivalence: 1.34, thus\ 5\ kg\ C4 = 6.7\ kg\ TNT$$

Using Equation 2-27 through Equation 2-30

$$Z = \frac{R}{W^{\frac{1}{3}}}; \qquad Z_{3.5m} = \frac{3.5m}{6.7^{\frac{1}{3}}} = 1.857; \qquad Z_{4m} = 2.122; \qquad Z_{5m} = 2.652$$

$$\Delta P_s = \frac{0.662}{Z} + \frac{4.05}{Z^2} + \frac{3.288}{Z^3}$$

$$\Delta P_{s3.5m} = \frac{0.662}{1.857} + \frac{4.05}{1.857^2} + \frac{3.288}{1.857^3} = 2.04\ Bar; \quad Total\ P = 305\ 310\ Pa$$

$$\Delta P_{s4m} = 1.556\ Bar; \qquad Total\ P = 256\ 890\ Pa$$

$$\Delta P_{s5m} = 1.002\ Bar; \qquad Total\ P = 201\ 510\ Pa$$

Positive pressure phase time duration was taken from ConWep as there is no conventional equation used for this purpose.

Table 6-1 – ConWep and analytical Results at different standoffs.

	Standoff Distance		
	3.5 m	**4 m**	**5 m**
Max Pressure Analytical (Pa) [*Equation 2-30*]	305 310	256 890	201 510
Max Pressure ConWep (Pa)	331 283	272 049	206 869
Positive Phase Duration (s)	0.0033	0.0037	0.0047

6.2 Defense Research and Development Canada Experimental Results

The Defense Research and Development Canada team at DRDC-Valcartier, Quebec provided a substantial amount of blast data to compare to and validate the numerical models against.

The following two charts are a summary of peak overpressures from a number of explosive trials. Five kilogram (Figure 6-1) and 10kg (Figure 6-2) cylindrical C4 charges were detonated at different heights of burst, with sensors positioned at various heights and standoffs. DRDC-Valcartier also provided individual pressure traces for each run used in the pressure validation section below to compare against the numerical model pressure results.

These summary charts show that there is a large scatter in the experimental peak overpressure data. For experiments with different heights of burst this difference can be expected; for example in a lower height of burst scenario the shock wave impinges on the ground earlier producing the Mach stem effect faster and giving higher pressures in the near-field and mid-field regimes. A lower pressure sensor height is also more likely to be below the triple point phenomenon and thus register a higher peak pressure reading from the Mach stem. For

identical heights of burst and sensor heights in the scatter in the data is due to: charge shape effects, non-ideal detonation, impingement of detonation products, non-uniform wave-dynamics within the early expansion of the fireball, and the gauges not being able to resolve the large change in density and temperature across the contact surface of the fireball. These tests were also performed at different times of year and as such the ambient conditions were different, introducing a small variability.

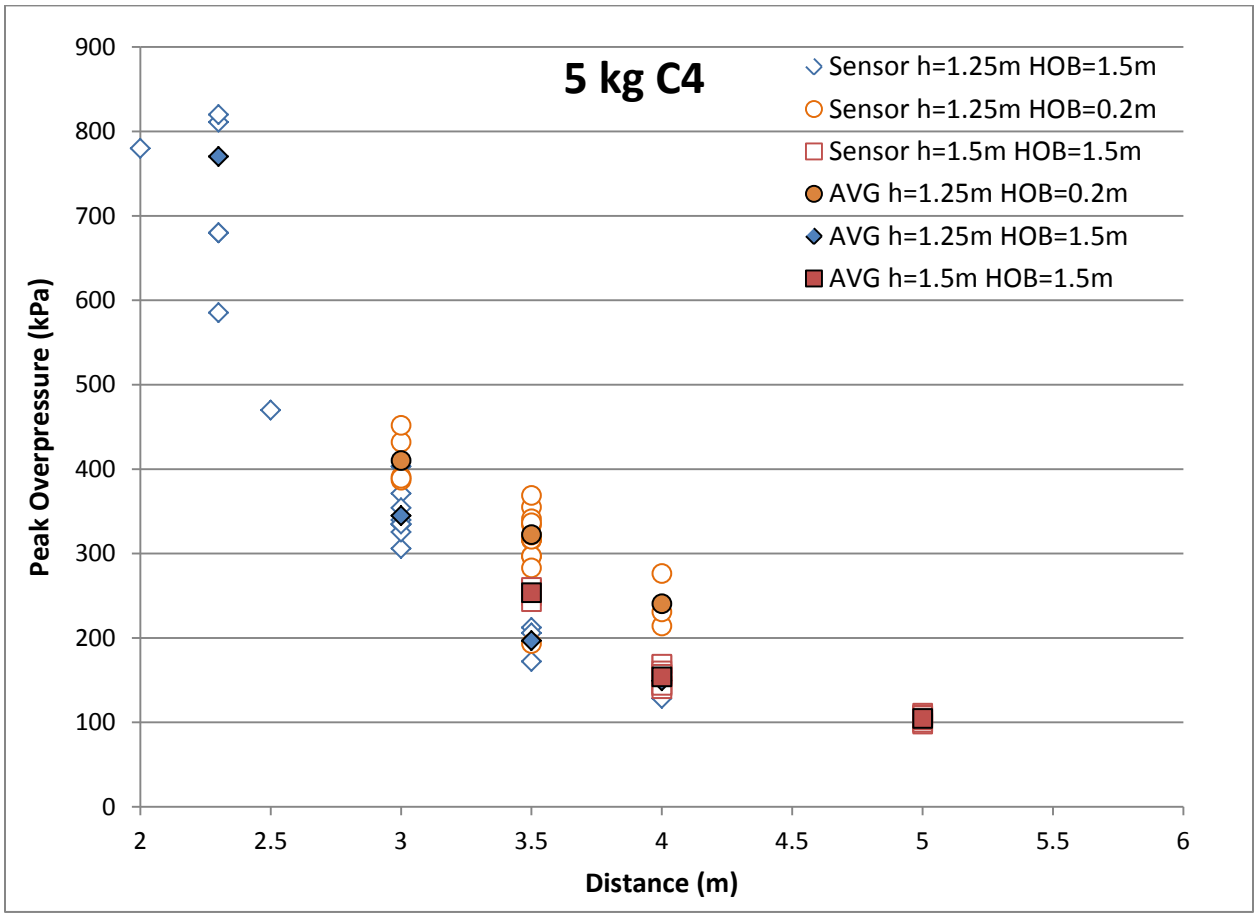

Figure 6-1 – Experimental peak overpressure vs. distance for 5 kg C4 charge [DRDC – Valcartier]

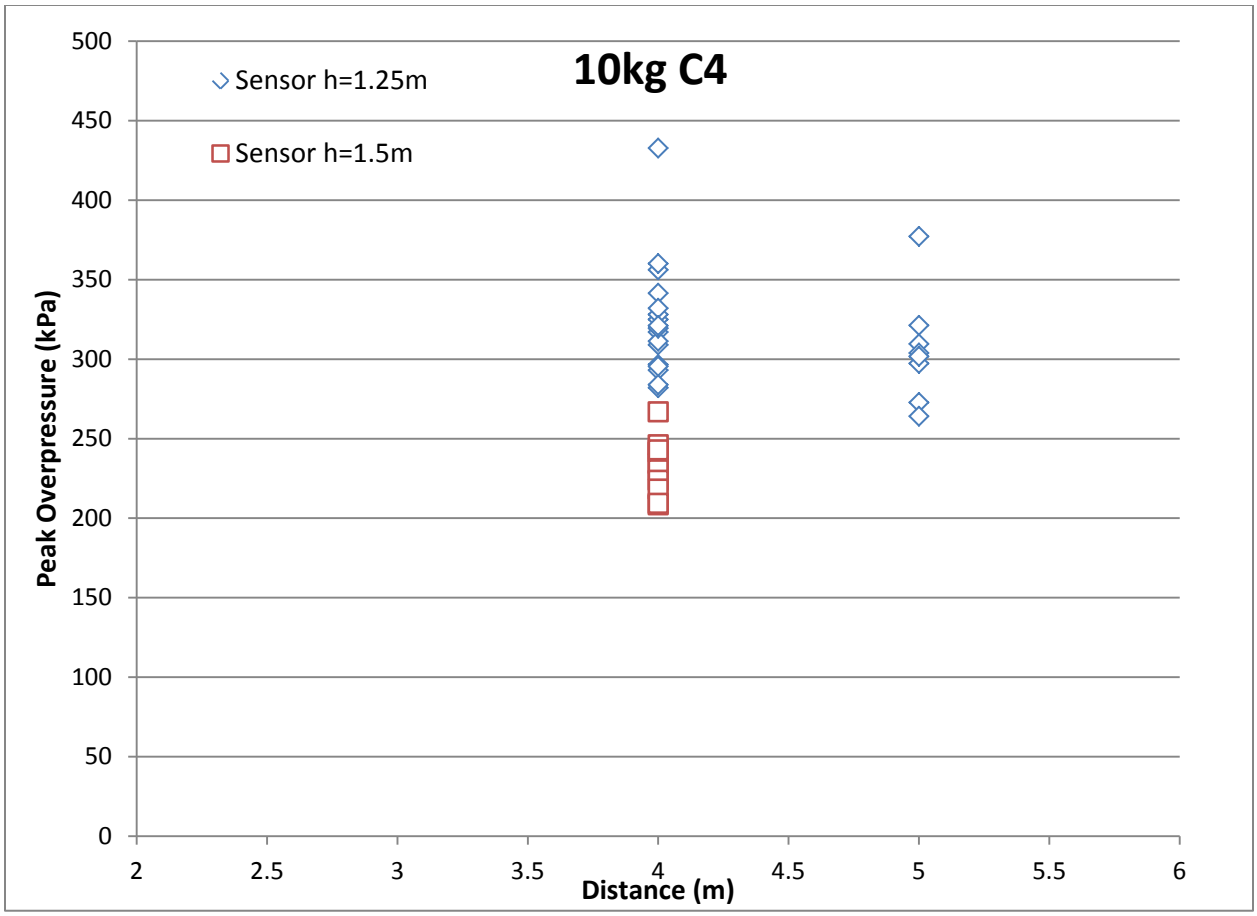

Figure 6-2 – Experimental peak overpressure vs. distance for 10 kg C4 charge [*DRDC – Valcartier]*

6.3 Model Validation: Static Pressure

The predicted pressure for each FEM model was validated against the Defense Research and Development Canada experimental pressure traces. These traces were validated quantitatively for peak pressure, impulse, and arrival time producing error percentages, and for general curve fit using a cross correlation software CORA. CORA cross-correlates two time-history signals to evaluate phase shift, curve shape correlation, and area under the curve to give an overall cross-correlation rating between 0 and 1 which can be considered a quantitative assessment of the shape of the signal [Gehre, 2009].

6.3.1 LBE Model vs. DRDC Pressure Validation

Three experimental blast tests were used to validate the incident pressure traces applied in the LBE model. The experimental tests (shots), conducted at DRDC – Valcartier, were 5 kg cylindrical C4 charges with a HOB and sensor height of 1.5 m, applied at standoff distances of 3.5 m, 4 m, and 5 m (Figure 6-3-Figure 6-5). For each distance two repeated shots were undertaken, and the static pressure was measured using side-on lollipop gauges to give two independent pressure profiles. These profiles were then compared to the simulated GEBOD blast environment using the same blast setup and orientation. The static incident pressure applied to the GEBOD model gives comparable peak pressures to that of the experimental pressure data; however, generally a higher impulse, the pressure traces were quantitatively analyzed using cross correlation (CORA) (Table 6-2).

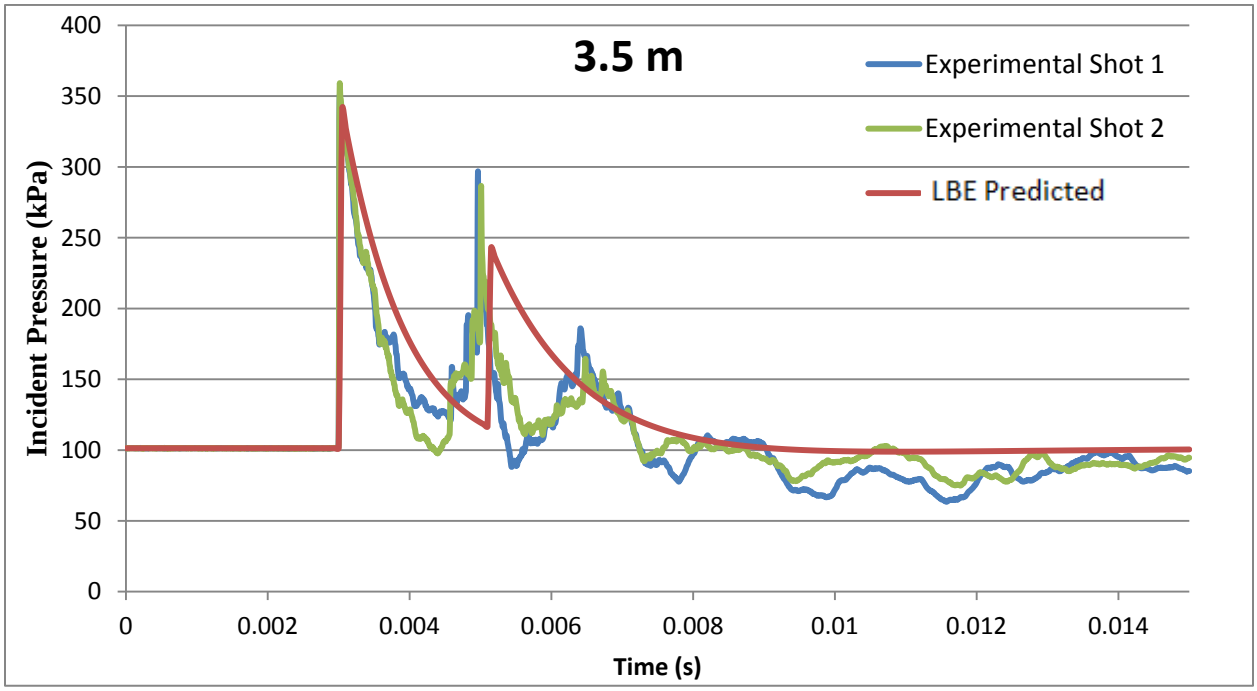

Figure 6-3 – Validation of LBE incident pressure at 3.5 m standoff from a 5 kg C4 charge with a 1.5 m HOB and a 1.5 m sensor height versus experimental data.

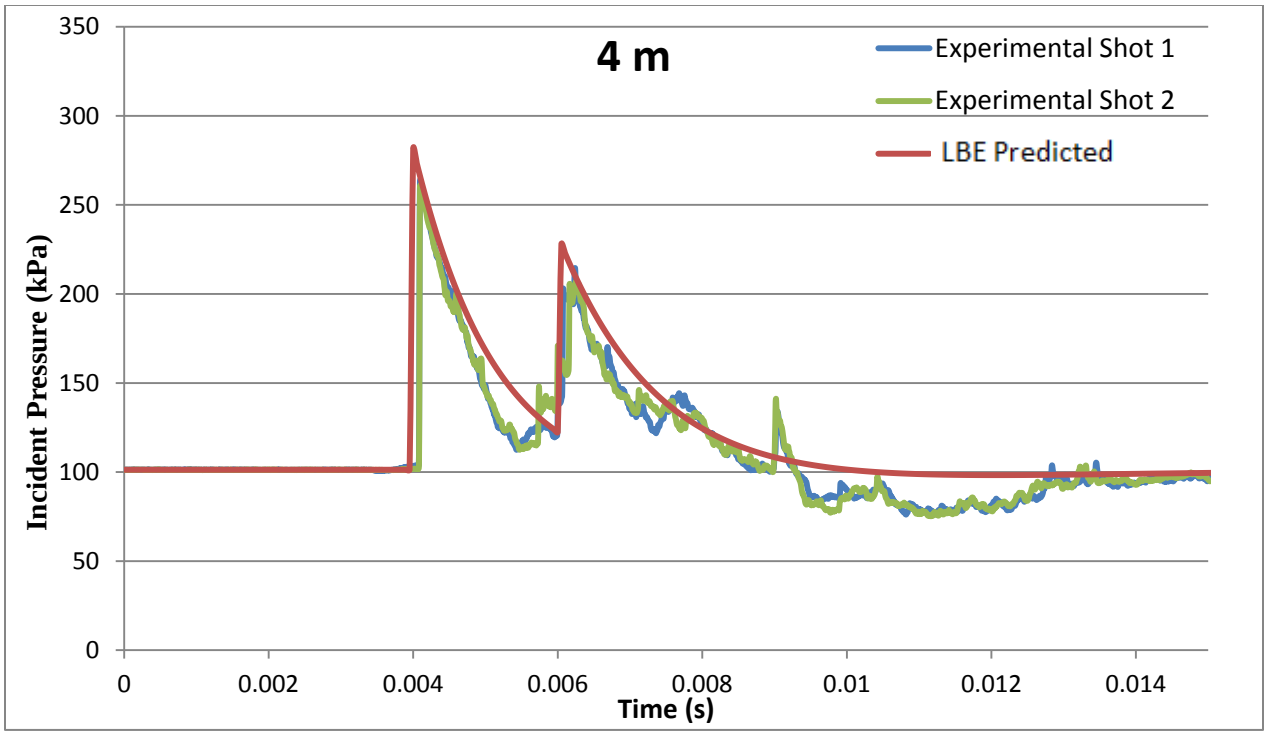

Figure 6-4 – Validation of LBE incident pressure at 4 m standoff from a 5 kg C4 charge with a 1.5 m HOB and a 1.5 m sensor height versus experimental data.

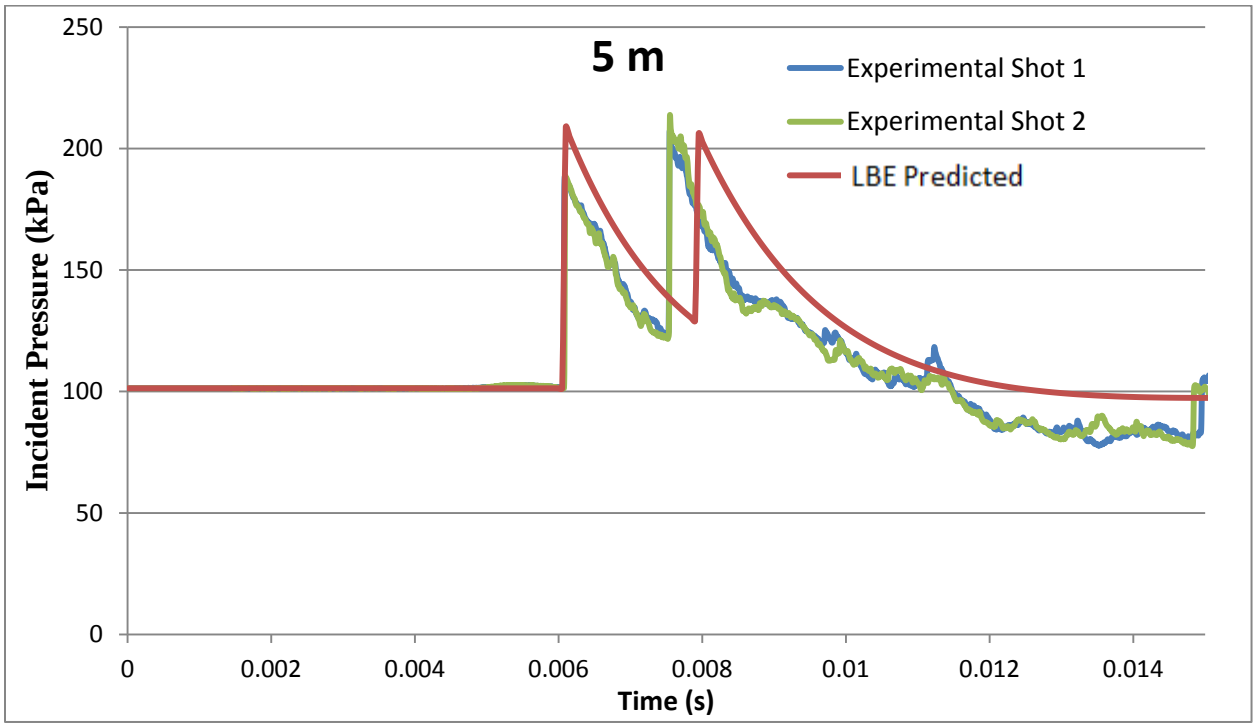

Figure 6-5 – Validation of LBE incident pressure at 5 m standoff from a 5 kg C4 charge with a 1.5 m HOB and a 1.5 m sensor height versus experimental data.

Table 6-2 – CORA quantitative cross-correlation ratings for LBE vs. DRDC experimental data.

Standoff	DRDC Pressure Curve	Size Comparison	Curve Shape Cross-Correlation	Rating of Signal Shape	Average Rating
3.5 m	DRDC Shot 1	0.821	0.986	0.903	0.903
3.5 m	DRDC Shot 2	0.815	0.990	0.902	
4 m	DRDC Shot 1	0.852	0.997	0.925	0.924
4 m	DRDC Shot 2	0.848	0.998	0.923	
5 m	DRDC Shot 1	0.992	0.998	0.996	0.994
5 m	DRDC Shot 2	0.987	0.995	0.991	
Total Average Correlation for LBE Pressure Traces					0.940

As the standoff distance increased the LBE pressure predictions had a higher level of correlation to the experimental pressure data especially in terms of size. In all three curves the impulse of the LBE was higher than that of the experimental trials, which resulted in a higher applied force thus higher acceleration. This may be due to inaccuracies in the LBE code in near-field distances or of the inherent error produced by measuring experimental data in the near-field. In the 5 m case, (Figure 6-5), the secondary pressure peak arrives later than in the experimental trial, this was due to the oblique reflection wave being modelled as travelling through uncompressed air at ambient conditions; whereas, in the actual case the reflected wave is travelling through pre-compressed, pre heated gases from the incident wave and would travel slightly faster. The ratings of all curve comparisons were of a high level of convergence thus the pressure traces predicted by the Load Blast Enhanced method had a good correlation to experimental data.

6.3.2 Cylindrical ALE Model vs. DRDC Pressure Validation

The cylindrical mesh was only validated against the incident wave, and was not validated for a ground reflection case. Further development of the cylindrical model is required to validate a fluid structure interaction model using a cylindrical mesh. The results are only reported for the

3.5 m and 4 m cases due to the required scaling and subsequent size of the model. The cylindrical model has a very high correlation to the incident wave of the DRDC data, with a similar pressure peaks, curve shape, and impulse (Table 6-3).

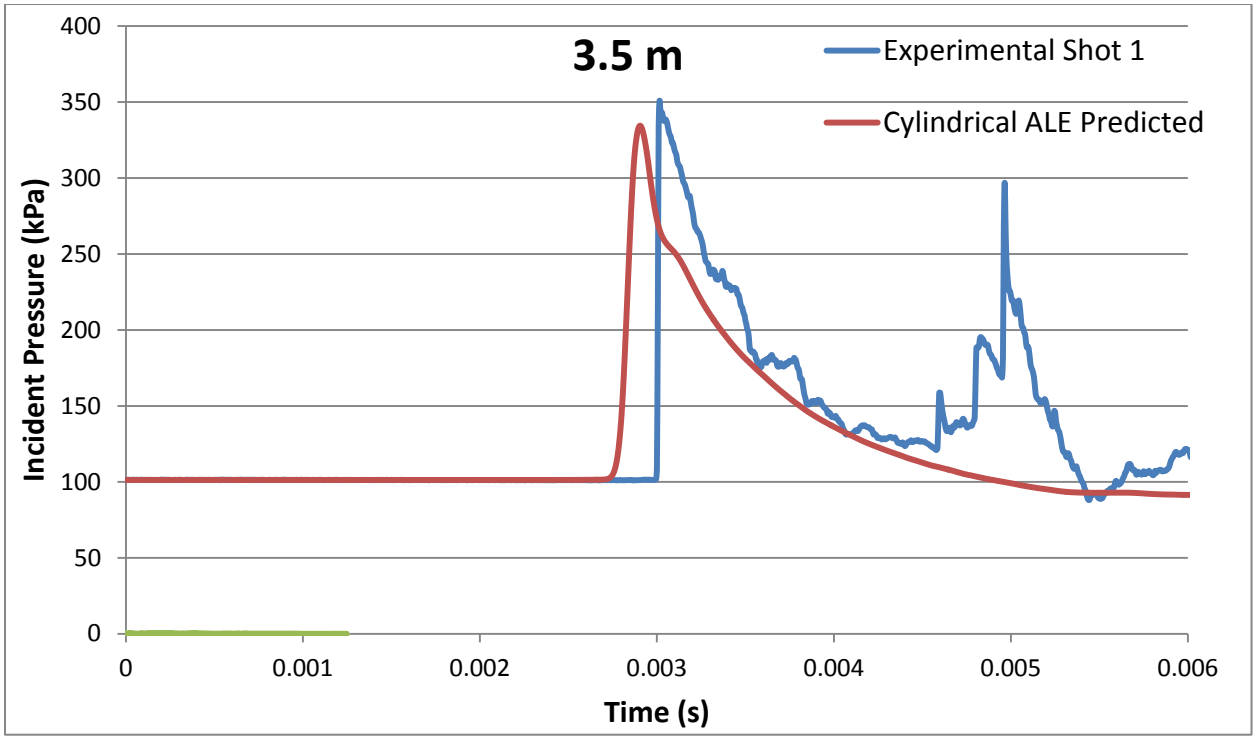

Figure 6-6 – Validation of Cylindrical ALE incident pressure with no ground reflection at 3.5 m standoff from 5 kg C4 charge, 1.5 m HOB and a 1.5 m sensor height versus experimental data.

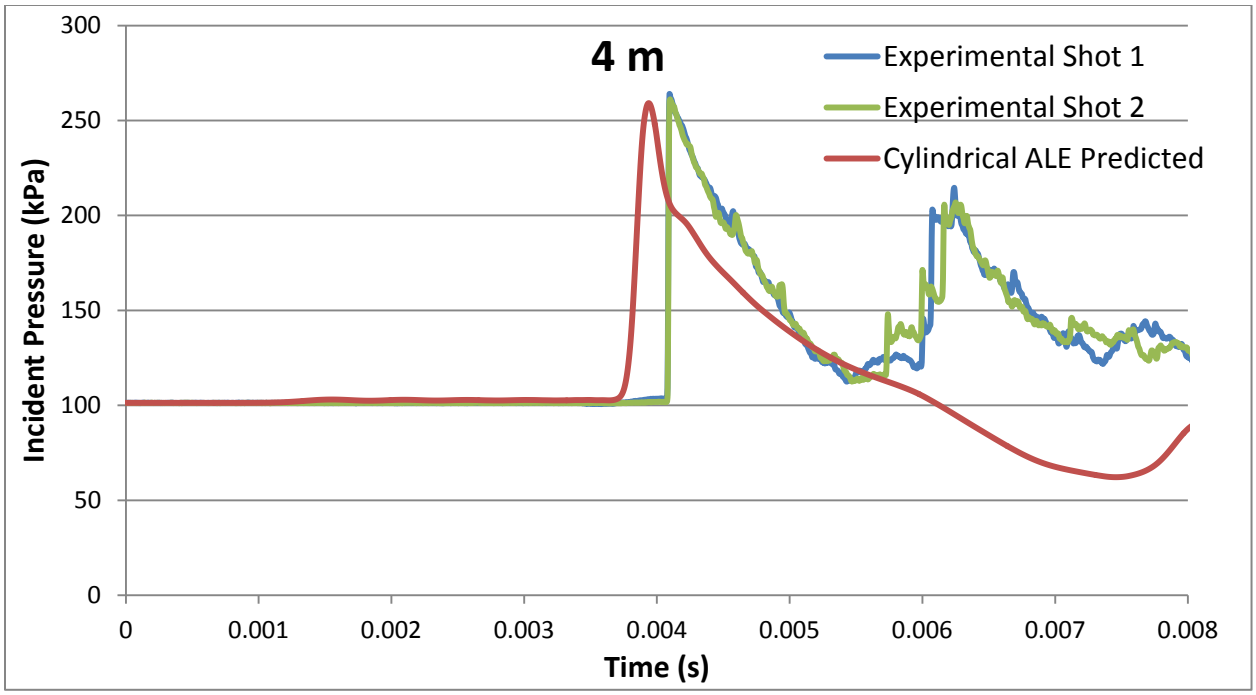

Figure 6-7 – Validation of Cylindrical ALE incident pressure with no ground reflection at 4 m standoff from 5 kg C4 charge, 1.5 m HOB and a 1.5 m sensor height versus experimental data.

Table 6-3 – CORA cross-correlation rations for Cylindrical ALE vs. DRDC Experimental data, incident wave only.

Standoff	DRDC Pressure Curve	Size Comparison	Curve Shape Cross-Correlation	Rating of Signal Shape	Average Rating
3.5 m	DRDC Shot 1	0.991	0.999	0.995	0.988
3.5 m	DRDC Shot 2	0.962	0.997	0.980	
4 m	DRDC Shot 1	0.990	0.999	0.994	0.993
4 m	DRDC Shot 2	0.985	0.999	0.992	
Total Average Correlation for LBE Pressure Traces					0.990

6.3.3 Spherical Charge Shape Incident Pressure Scaled to Cylindrical Charge Shape

The blast wave propagating perpendicular to the axis of cylindrical shaped charge is governed by the physics of cylindrical expansion determined by the Length to Diameter (L/D) ratio of the cylindrical charge. Therefore along a particular direction the blast wave may evolve from a quasi-cylindrical to a quasi-spherical expansion and the fractional ratios become meaningful in

describing the blast-wave flow. The DRDC uses a L/D ratio of 1/1 and this ratio curve, (Figure 6-8), was used to scale the peak pressure seen in a spherical numerical simulation using the material properties for C4, (Section 5.2.4).

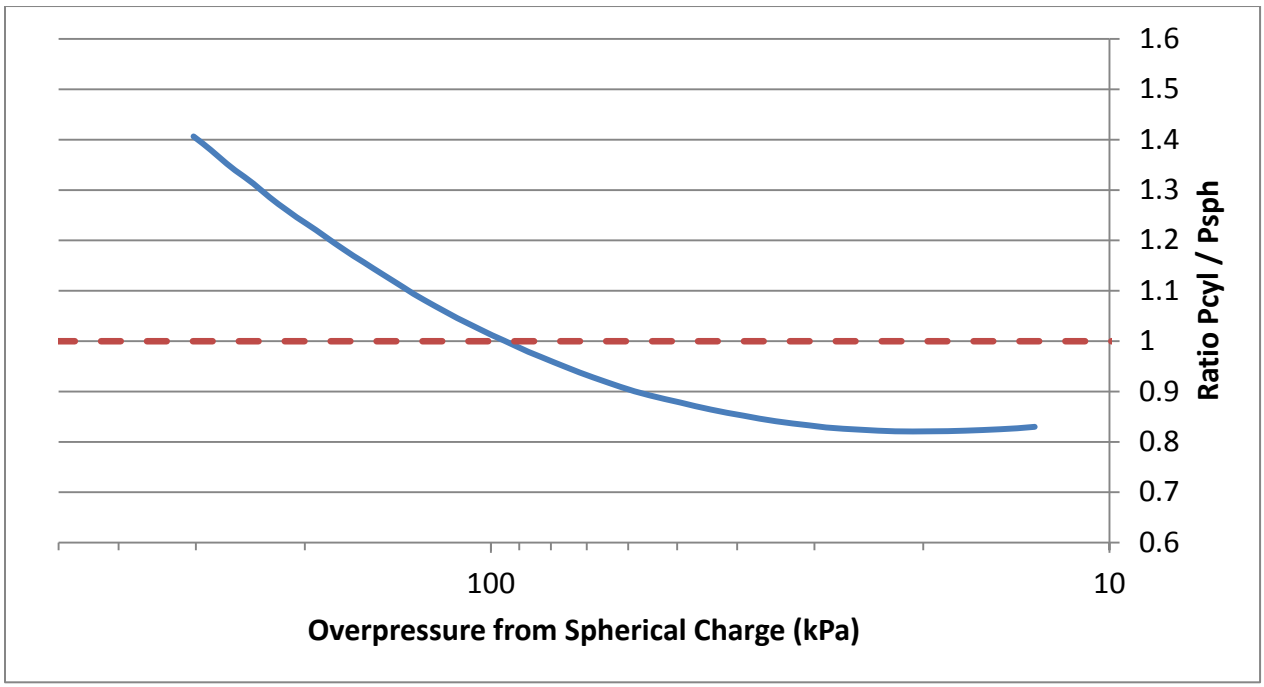

Figure 6-8 – Pressure ratio of a cylindrical charge over spherical charge vs. Overpressure from a spherical charge explosion [Adapted from Petes, 1986].

Table 6-4 – Peak Pressure comparison of spherical ALE charge with no E0 increase scaled to cylindrical charge shape vs. DRDC and ConWep.

	Peak Pressure (kPa)		
	3.5 m	***4 m***	***5 m***
DRDC Average All Trials	355	255	206
ConWep	331	272	207
No E0 Adjustment Numerical Simulation	289	239	170
Difference From ConWep	-13%	-12%	-18%
Difference From DRDC Average	-19%	-6%	-17%
Pressure Rationed Numerical Simulation (Figure 6-8)	331	255.6	167
Difference From ConWep	0%	-6%	-19%
Difference From DRDC Average	-7%	0%	-19%

It can be seen that a spherical charge drastically underestimates the peak pressure when compared to DRDC experimental data and ConWep. This underestimate is not due to the smearing of the shock wave but to the shape of the charge in the simulation, thus the impulse and insult force of the explosive wave is also underestimated. The rationed pressure results have improved correlation with both the DRDC and ConWep in the near-field regime, but do not improve the results in the far-field as the pressure ratio actually drops below one thus increasing the difference.

6.3.4 Spherical ALE Model vs. DRDC Pressure Validation

The Spherical ALE model provides a more complete simulation of a blast physics problem allowing one to view the detonation wave, expansion of the fireball, wave reflections, the Mach stem triple point and the subsequent interaction with a subject (Figure 6-9).

The DRDC trials were undertaken using cylindrical charges with a L/D ratio of 1/1; however, to obtain suitable propagation of a shock wave in ALE the mesh must expand radially from the center of mass of the explosive, thus a spherical mesh was used extensively in this study. In order to account for the cylindrical overpressure expansion ratio the E0 of the explosive in the JWL equation of state was increased to 1.5E10 for the spherical model to give a similar pressure and impulse response to that of the experimental DRDC explosive trials. By increasing the initial energy of the explosive the insult to the GEBOD could be validated against experimental cases.

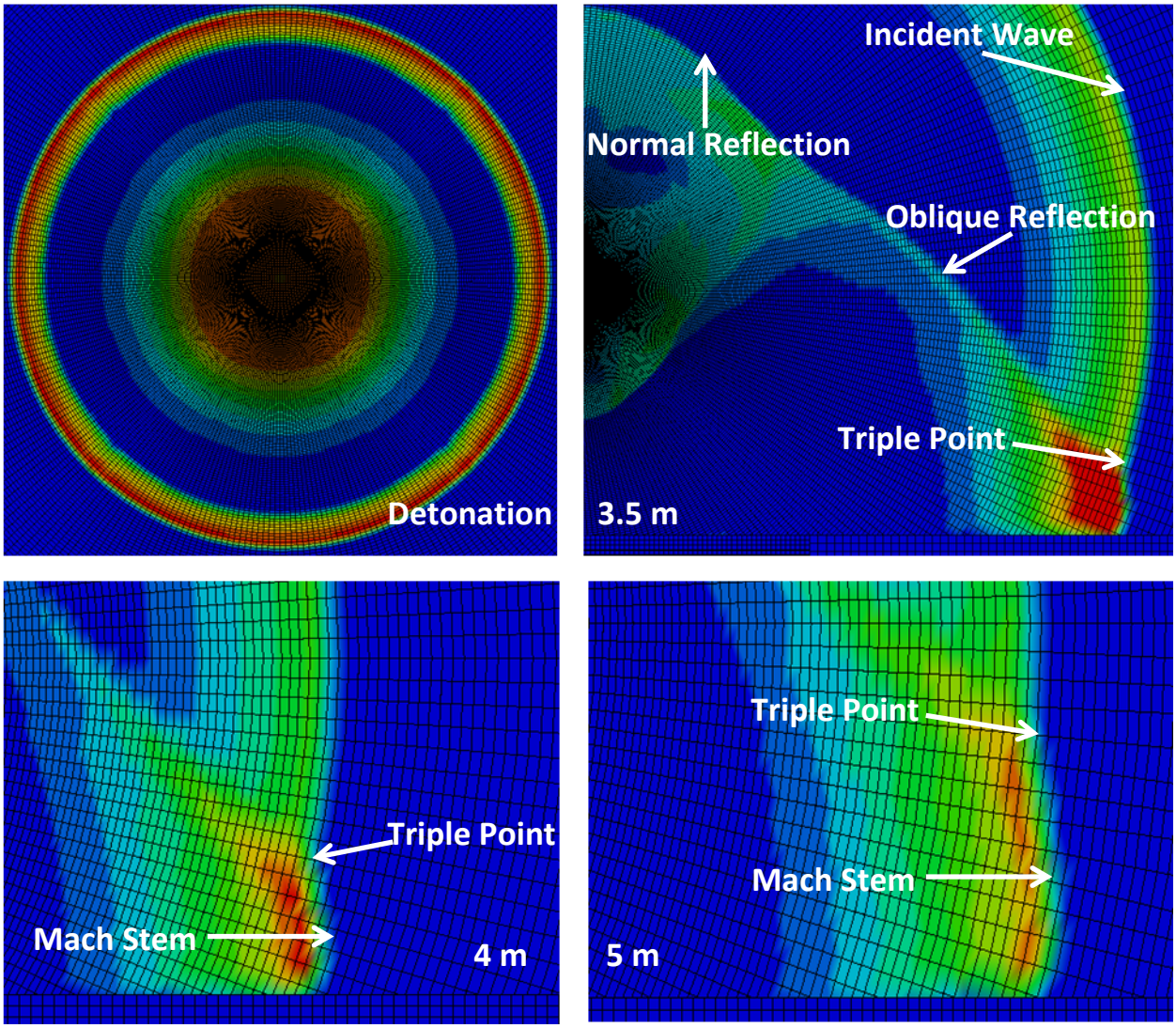

Figure 6-9 – Shock wave pressure composition of spherical ALE model at detonation, 3.5 m, 4 m and 5 m.

The same three experimental blast tests (shots) used for the LBE validation were used to validate the incident pressure traces of the spherical ALE model. The experimental shots, conducted at DRDC – Valcartier, included 5 kg cylindrical C4 charges, with a HOB and sensor height of 1.5 m, applied at standoff distances of 3.5 m, 4 m, and 5 m (Figure 6-10 - Figure 6-12). For each distance two repeated trials were undertaken, and the static pressure was measured using side-on lollipop gauges to give two independent pressure profiles. These profiles were

then compared to the spherical ALE blast environment using the same blast setup and orientation. The incident pressure applied at these standoff distances gives comparable peak pressures and impulse for each pressure trace to that of the experimental pressure data, the pressures are quantitatively analyzed using cross correlation (Table 6-5).

The smearing of the incident and reflected pressure peaks especially in the 5 m case, results in the reflected wave having a faster arrival time but a very similar impulse to the experimental results (Figure 6-12). The pressure traces had a high level of correlation to the DRDC data, with comparable peak pressures, impulse, and curve shape.

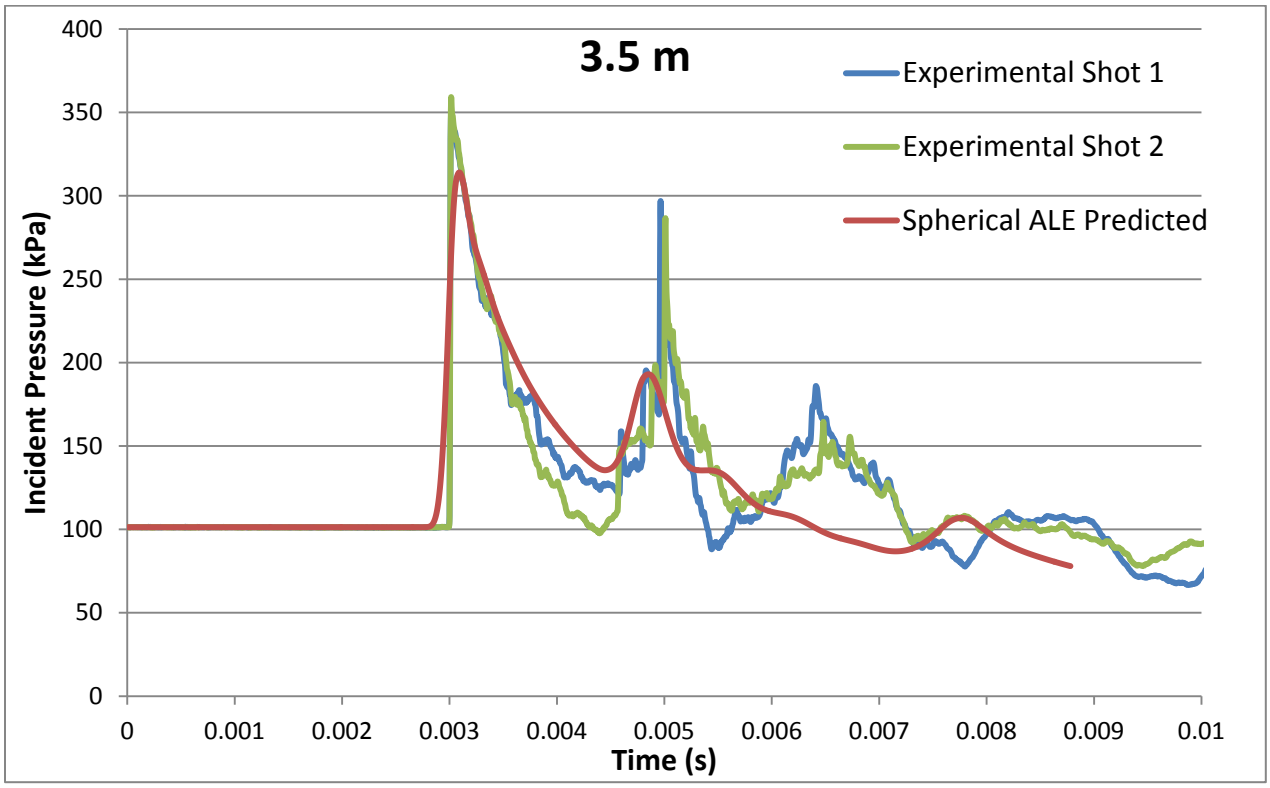

Figure 6-10 – Validation of Spherical ALE incident pressure at 3.5 m standoff from a 5 kg C4 charge with a 1.5 m HOB and a 1.5 m sensor height versus experimental data.

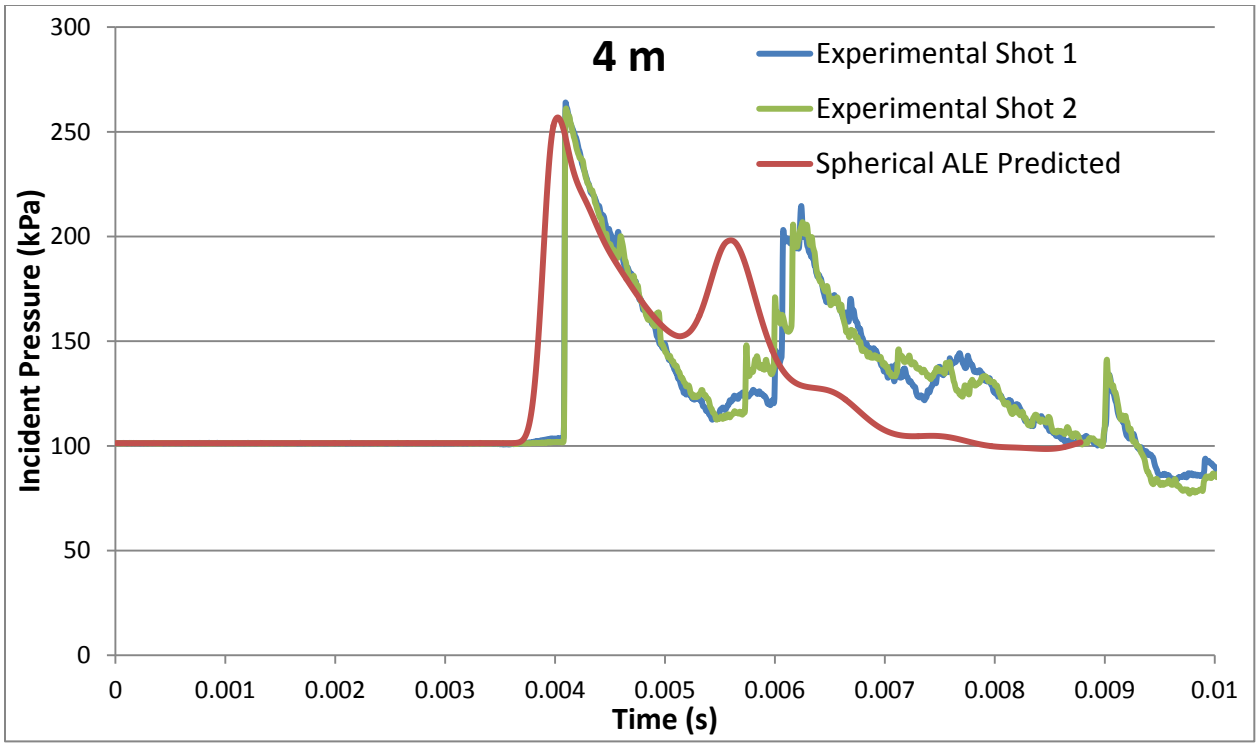

Figure 6-11 – Validation of Spherical ALE incident pressure at 4 m standoff from a 5 kg C4 charge with a 1.5 m HOB and a 1.5 m sensor height versus experimental data.

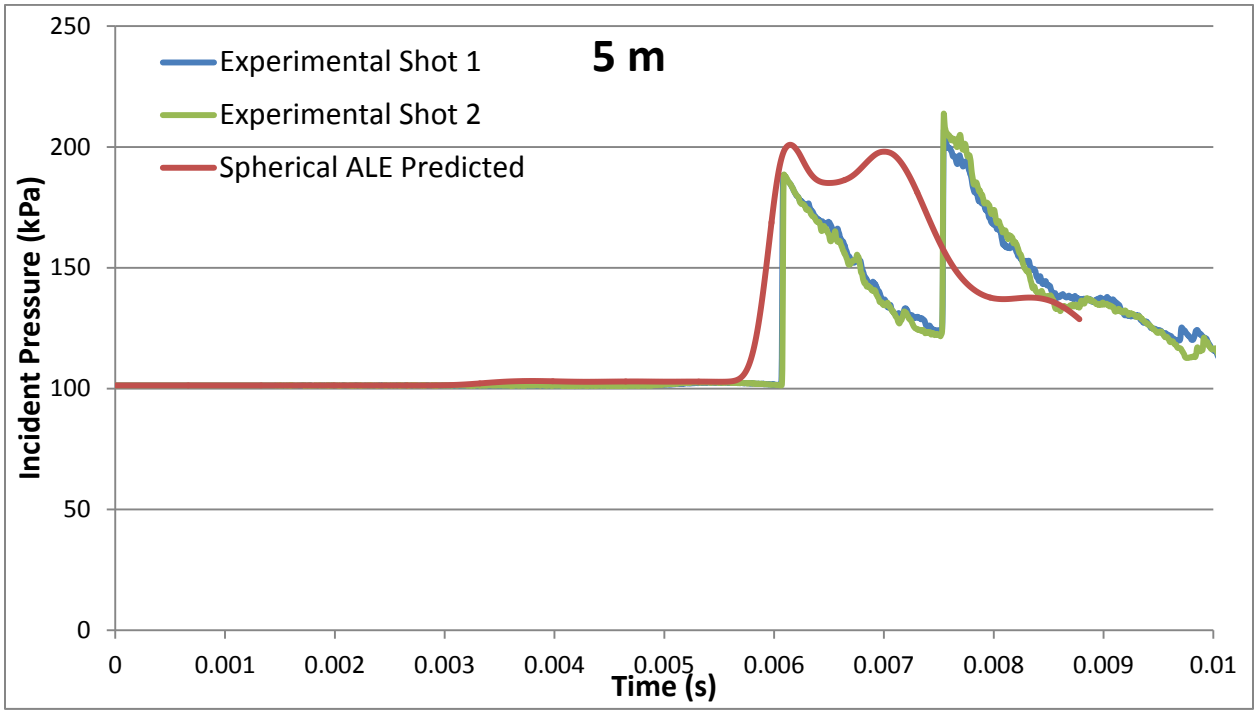

Figure 6-12 – Validation of Spherical ALE incident pressure at 5 m standoff from a 5 kg C4 charge with a 1.5 m HOB and a 1.5 m sensor height versus experimental data.

Table 6-5 – CORA cross-correlation rations for Spherical ALE vs. DRDC Experimental data.

Standoff	DRDC Pressure Curve	Size Comparison	Curve Shape Cross-Correlation	Rating of Signal Shape	Average Rating
3.5 m	DRDC Shot 1	0.961	0.992	0.976	0.978
3.5 m	DRDC Shot 2	0.968	0.992	0.980	
4 m	DRDC Shot 1	0.987	0.990	0.989	0.990
4 m	DRDC Shot 2	0.988	0.991	0.990	
5 m	DRDC Shot 1	0.994	0.993	0.953	0.953
5 m	DRDC Shot 2	0.911	0.992	0.952	
Total Average Correlation for LBE Pressure Traces					0.973

6.3.5 All Models Pressure Summary

The peak pressures, arrival times, and impulse of each model was compared to DRDC experimental results and ConWep results for 3.5 m, 4 m, and 5 m, (Table 6-6; Table 6-7; Figure 6-13). The LBE impulse correlates with the ConWep equations; however, when compared to the experimental DRDC results there is a big discrepancy. The LBE predicts a higher impulse for the total blast wave then the DRDC; this is most likely due to the perfect ground reflection inherent in its model as well as improper modelling of realistic wave losses. The spherical ALE model matches well with both ConWep incident wave impulse and the DRDC total wave impulse with errors under 11% for all stand offs. The pressure results from the Spherical ALE with adjusted E0, and the LBE model have good correlation with experimental values and each other enabling them to be used in a fluid structure interaction study for injury prediction employing the GEBOD human surrogate. Pressure trace result graphs of all models were also compared to one another for standoff distances of 3.5 m, 4 m, 5 m (Appendix B).

Table 6-6 –Peak pressure and arrival time for models compared to DRDC and ConWep.

	Peak Pressure (kPa)			Arrival Time (s)		
	3.5 m	***4 m***	***5 m***	***3.5 m***	***4 m***	***5 m***
ConWep	331	272	207	0.00319	0.00408	0.00608
DRDC Average All Trials	355	255	206			
Difference From ConWep	7%	-6%	0%			
Load Blast Enhanced	341	282	209	0.00320	0.00410	0.00610
Difference From ConWep	3%	3%	1%	0%	0%	0%
Difference From DRDC AVG	-4%	10%	1%			
No E0 Adjustment Spherical ALE Simulation	289	239	170	0.00310	0.00414	0.00610
Difference From ConWep	-13%	-12%	-18%	-3%	2%	0%
Difference From DRDC AVG	-19%	-6%	-17%			
Spherical ALE E0=1.5E10	319	264	201	0.00307	0.00397	0.00604
Difference From ConWep	-4%	-3%	-3%	-4%	-3%	-1%
Difference From DRDC AVG	-10%	4%	-2%			
Cylindrical ALE	333	266		0.00291	0.00394	
Difference From Conwep	1%	-2%		-9%	-3%	
Difference DRDC Average	-6%	4%				
Pressure Rationed Numerical Simulation (Figure 6 11)	331	256	167			
Difference From ConWep	0%	-6%	-19%			
Difference From DRDC AVG	-7%	0%	-19%			

Table 6-7 – Impulse for incident wave and blast wave including Mach stem.

	Incident Wave Impulse		Total Blast Wave Impulse (Mach Stem Included)		
	3.5 m	***4 m***	***3.5 m***	***4 m***	***5 m***
ConWep	186	165			
DRDC Average			206	216	181
Load Blast Enhanced	186	161	334	304	232
Difference From ConWep	0%	-2%			
Difference From DRDC AVG			62%	41%	28%
Spherical ALE	165	159	197	209	197
Difference From ConWep	-11%	-3%			
Difference From DRDC AVG			-4%	-3%	9%
Cylindrical ALE	138	120			
Difference From Conwep	-26%	-27%			

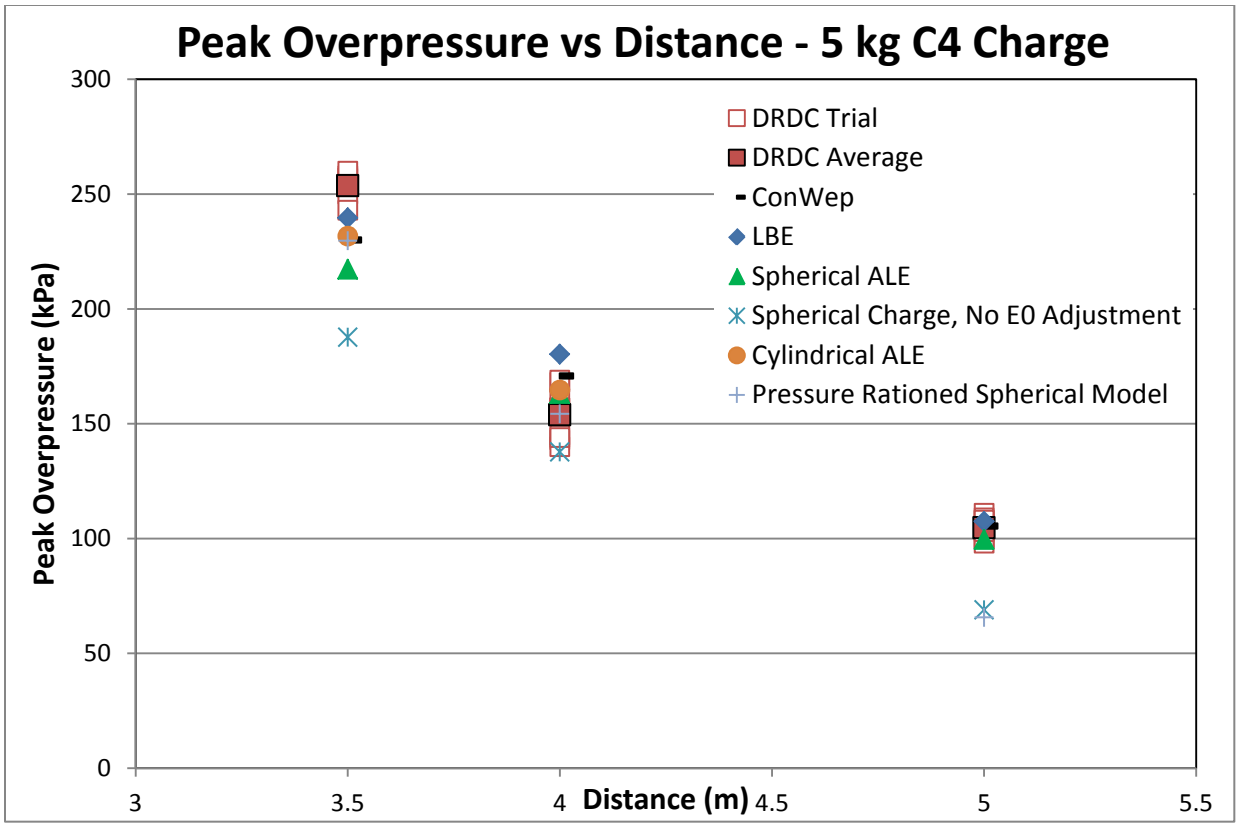

Figure 6-13 – Peak overpressure vs. distance for 5 kg C4 charge for all models compared to DRDC Results and ConWep.

6.3.6 Model Scalability

Both the LBE and spherical ALE model exhibit scalable qualities for both peak pressure and impulse (Figure 6-14). In this thesis the LBE model was used for a large parametric study of injury response from blast; however, the spherical ALE model was only used for a small number of cases due to the computational requirements of the model. This model should be further investigated parametrically for different blast scenarios to observe the effects of different explosive sizes on blast physics.

The scalability of the two models was validated against peak pressures of a multiple 10 kg C4 blasts at 4 m, and 5 m standoffs, with pressure sensors at 1.25 m, and 1.5 m. The LBE model

and ALE model pressure results fall within the variability of the DRDC data, and correctly model the difference in the pressure peaks below and above the triple point (Figure 6-14). This shows that both models are capable to be scaled to different explosive sizes while still holding a high level of precision.

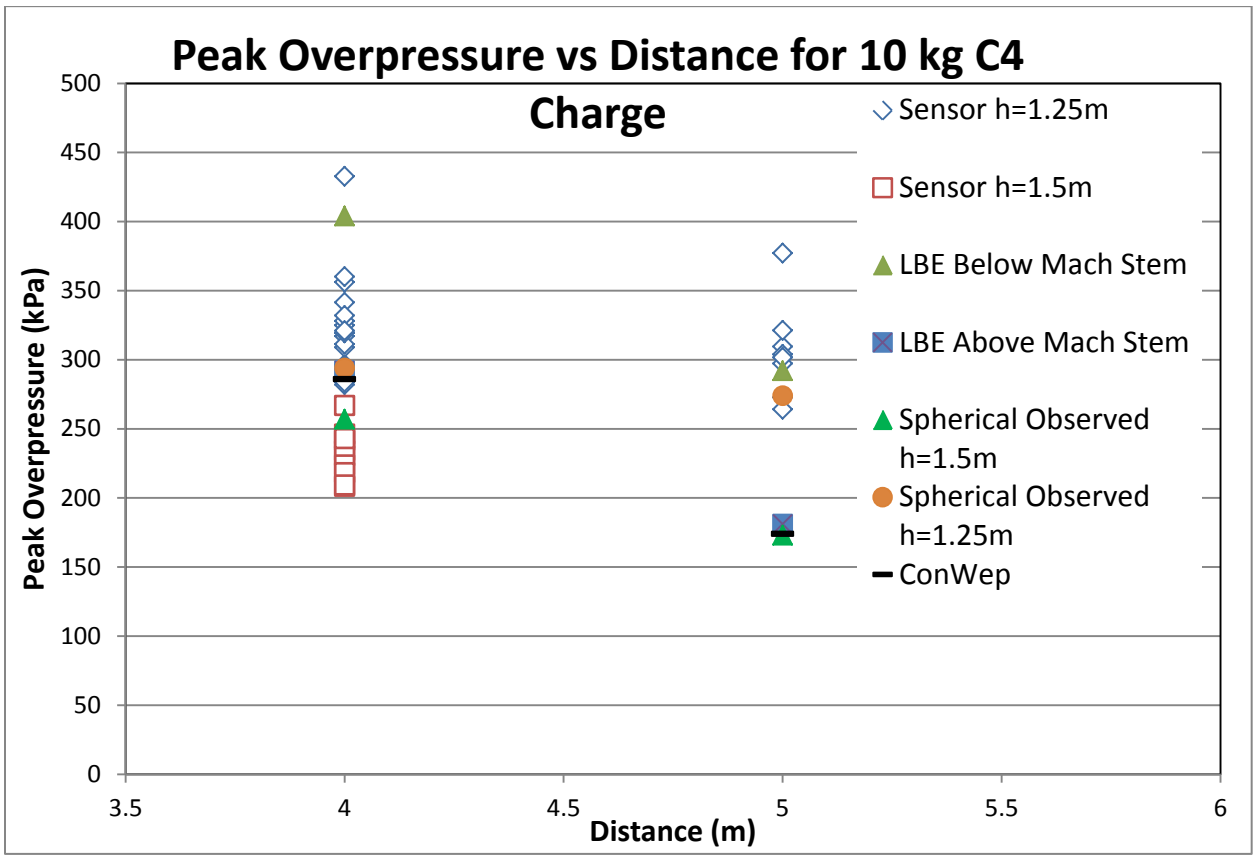

Figure 6-14 – Peak overpressure vs. distance for 10 kg C4 charge for LBE and Spherical ALE models compared to multiple DRDC tests and ConWep.

6.4 Global Head Kinematics Comparison

The GEBOD multi-body model (Figure 4-7) includes representations of body segment mass, joint location, and joint kinematics. For this thesis the 50th percentile male GEBOD was validated against several experimental blast scenarios with 5 kg C4 charges at a 1.5 m HOB with

varying standoff distances ranging from 3 m to 4 m (Figure 6-15). The experimental blasts were applied to a 50^{th} percentile male Hybrid III dummy instrumented with several head accelerometers to measure linear and rotational accelerations. These blast conditions were then numerically modelled using enhanced blast loading techniques and ALE fluid structure interaction. The kinematic response was evaluated from the center of gravity of the GEBOD head for each blast event. The acceleration versus time data was extracted for each situation, and filtered using a 4 pole Butterworth filter with a cut-off frequency of 1650 Hz which is equivalent to the CFC1000 filter used in the experimental trials, this filtering made little difference to the overall acceleration or HIC values with only major differences in the very near field where the HIC vastly exceeded the known tolerance levels, (Figure 6-16). This acceleration data was then evaluated based on the peak resultant acceleration and the HIC_{15} injury metric. A previous investigation determined that the GEBOD model head mass was lower than that of the Hybrid III dummy head by 0.3 kg [Lockhart et al., 2011], thus in this study the head mass was increased from 4.2 kg to 4.5 kg to be comparable.

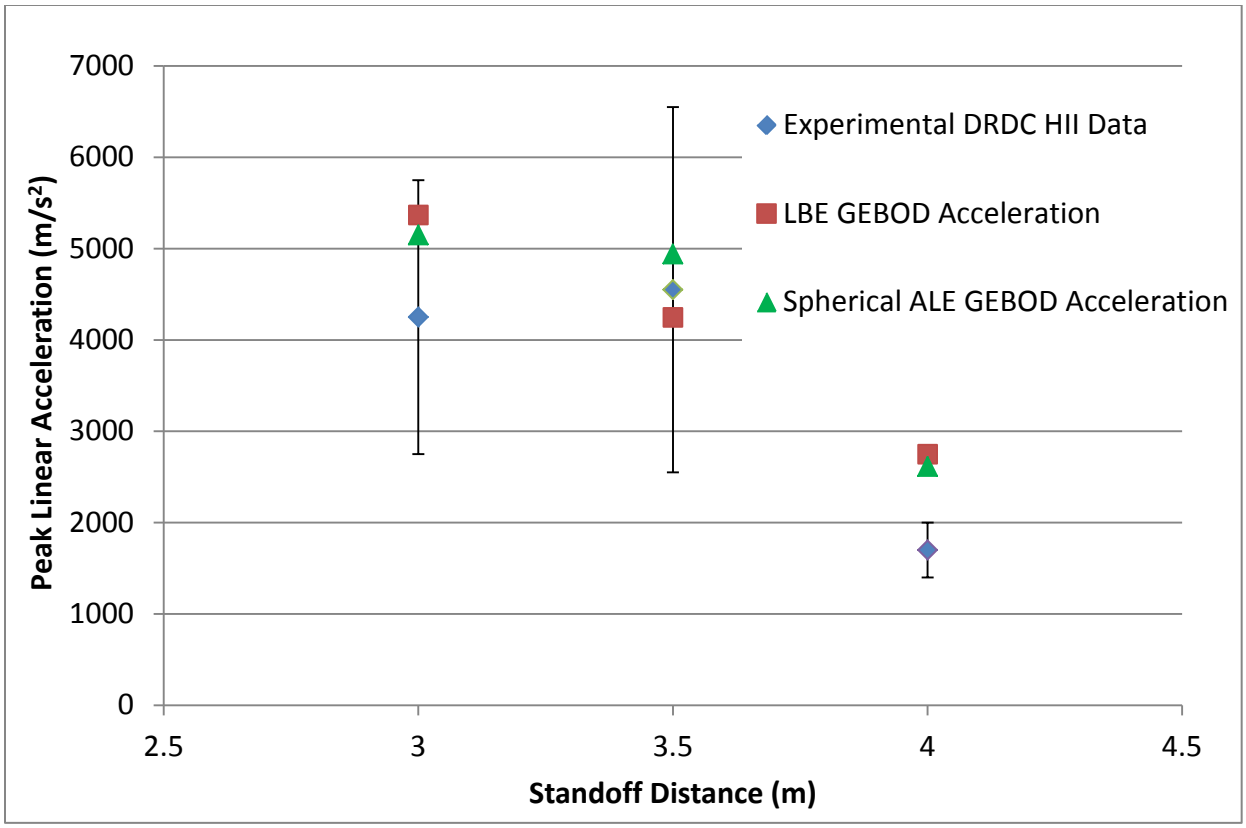

Figure 6-15 – GEBOD peak linear acceleration for LBE and Spherical ALE models against DRDC experimentally collected data at various standoff distances

There is a large scatter in the DRDC acceleration data in the near-field; this is due to charge shape effects, non-ideal detonation, impingement of detonation products, and non-uniform wave-dynamics within the early expansion of the fireball. The DRDC results also may not be exact, due to the small number of samples and differences between the GEBOD and HIII blast setups. Taking this into account it can be seen that both the LBE and spherical ALE models provide comparable peak head acceleration results at these distances, thus validating the GEBOD for use in this FEM study.

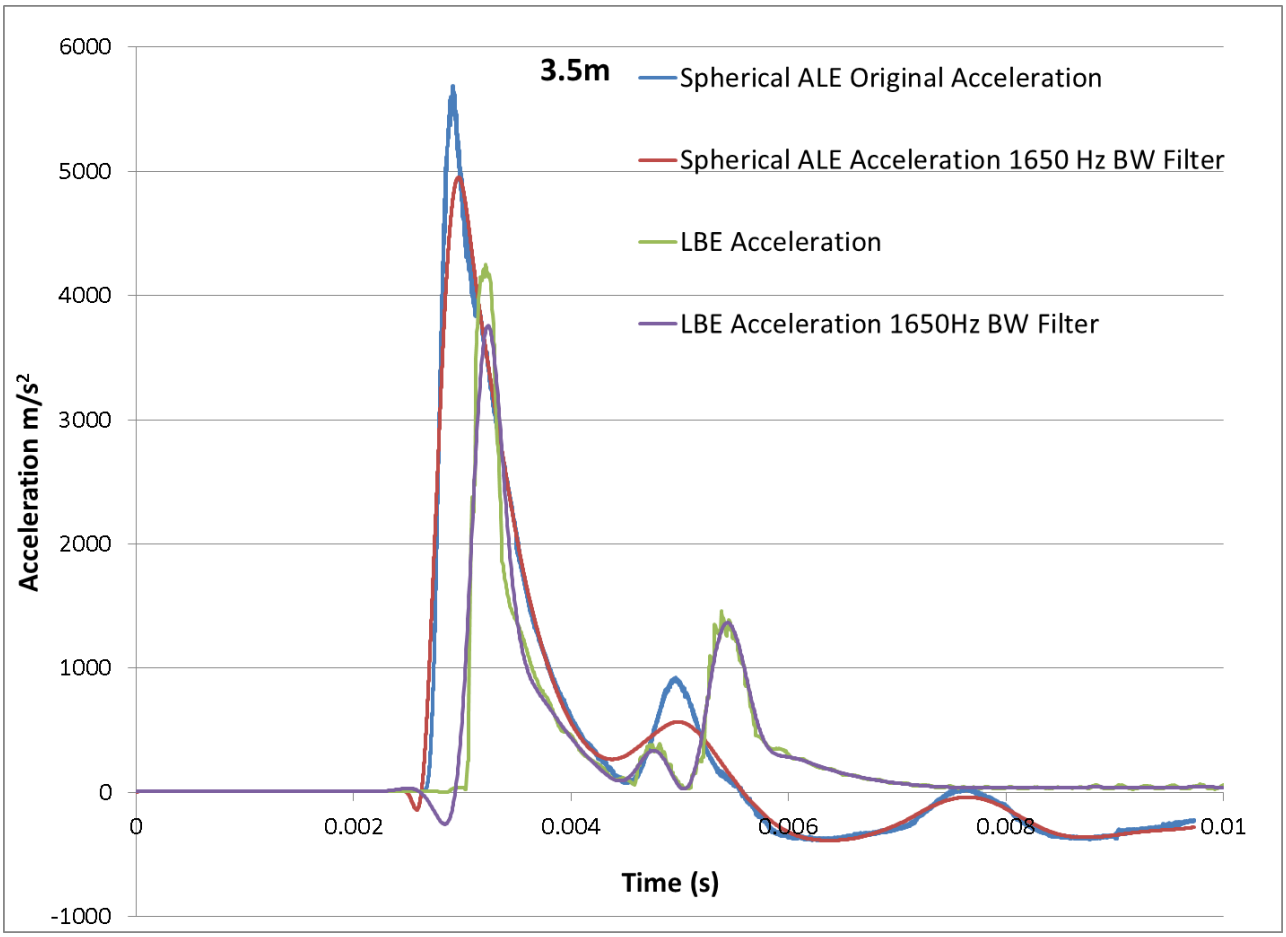

Figure 6-16 –Example of a GEBOD acceleration trace for a 5 kg explosive with a 3.5 m standoff for the Spherical ALE and LBE models, showing the effect of filtering on the data signal.

6.4.1 Parametric Study: Effect of Blast Load on Head Kinematics

A large parametric study the enhanced blast model was undertaken for this thesis as this method is relatively computationally efficient to model multiple scenarios. The standoff distance from the center of gravity of the GEBOD head to the center of the explosive charge was varied from 2 m to 7.5 m standoff and the HOB of the charge was set at 0.5 m, 1 m, and 1.5 m with no lateral offset from the target. Figure 6-17 shows the peak head acceleration of each acceleration signal as the blast wave reaches the head versus the standoff distance of the explosive charge.

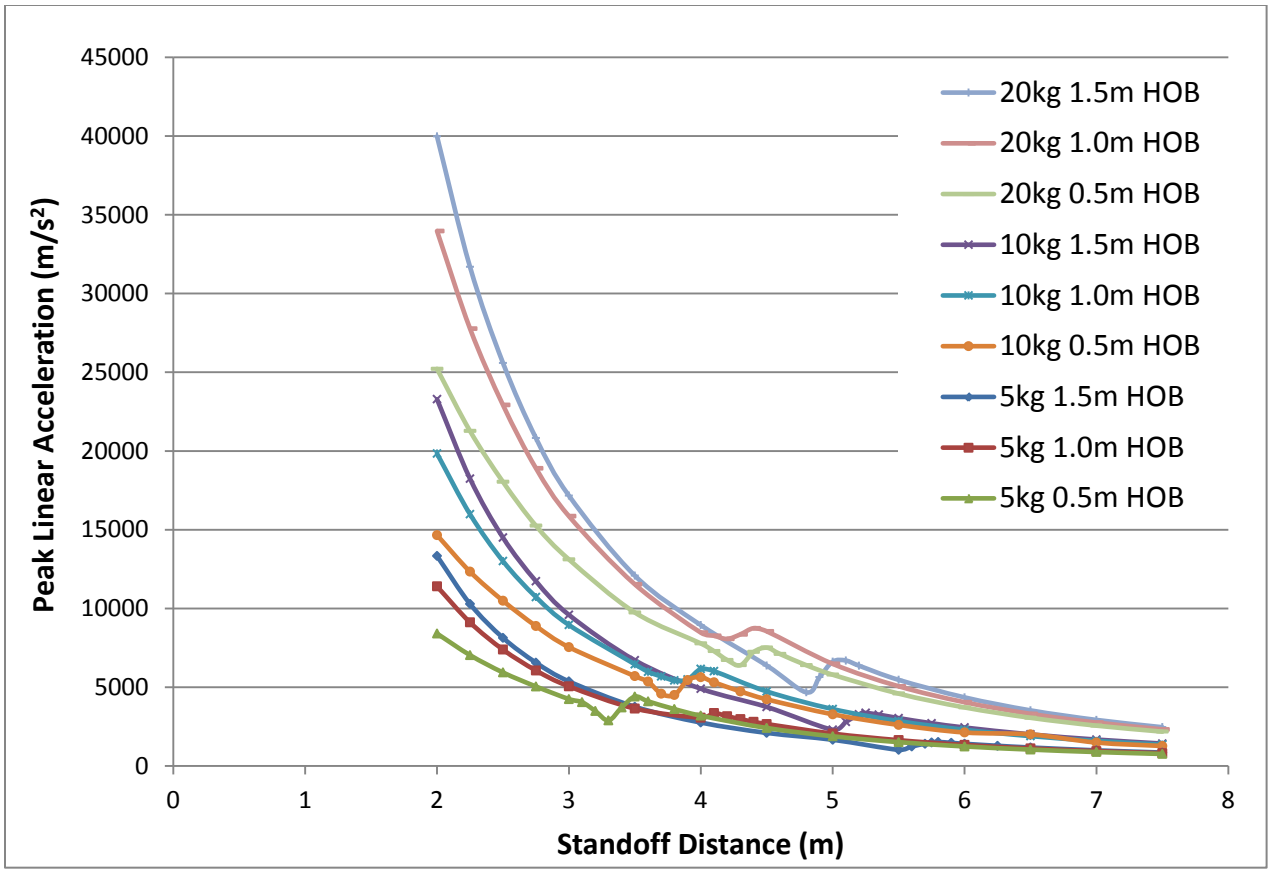

Figure 6-17 – Load Blast Enhanced parametric GEBOD study, peak acceleration vs. standoff distance for varying HOB.

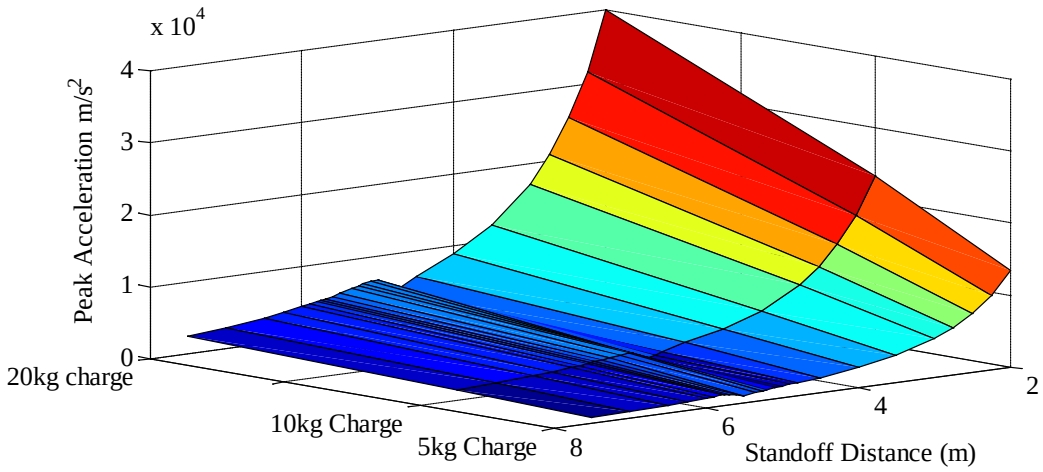

Figure 6-18 – 3D plot of peak acceleration vs. standoff for all three charges at 1.5 m HOB.

For the close proximity blast scenarios investigated, there was a rapid acceleration of the head over approximately 1 ms resulting from interaction with the blast wave. Increasing the standoff distance resulted in a reduction in peak acceleration until the Mach stem effect reached the height of the GEBOD head, which then caused an increase in acceleration. The Mach stem effect instantaneously increased the applied pressures when the triple point height reached the head height, leading to an increase in acceleration and expanding the potential injury zone surrounding a charge.

The trajectory of the triple point depends on the explosive size and HOB, with lower HOB resulting in earlier interaction of the head with the Mach stem since the incident wave reflects off the ground earlier in time. The peak acceleration values for a lower HOB are smaller (for the same ground standoff) due to the increase in true distance from the head center of gravity to the charge center.

6.4.2 Acceleration Results Spherical ALE Model Interaction with GEBOD

The spherical ALE model provides a more complete method of modelling fluid structure interaction, and can be used to monitor the wave dynamics around a structure as well as the kinematics involved in a blast event. That being said it is also computationally expensive and thus acceleration results were limited to 3 m, 3.5 m, 4 m, and 5 m standoffs. At 3.5 m the blast wave reaches the GEBOD as a spherically expanding wave with the Mach stem triple point height around mid-thigh, (Figure 6-19), whereas in the 5 m standoff case the Mach stem triple point reaches the GEBOD around the neck (Figure 6-21). The blast wave reflects off the GEBOD

and then refracts around the GEBOD accelerating the head once the incident wave reaches its standoff distance.

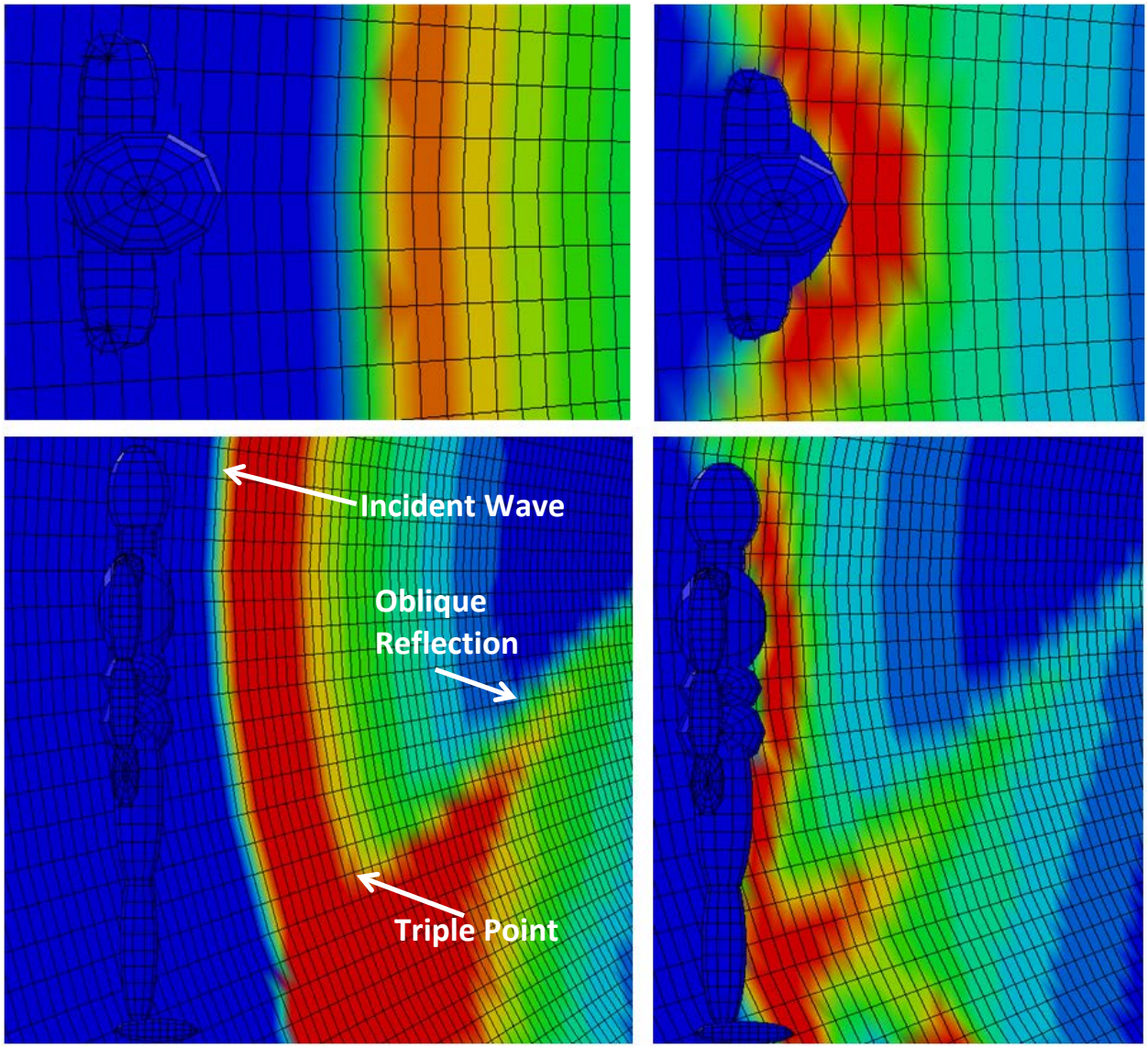

Figure 6-19 – Beginning of blast shock wave interaction with the GEBOD at 3.5 m.

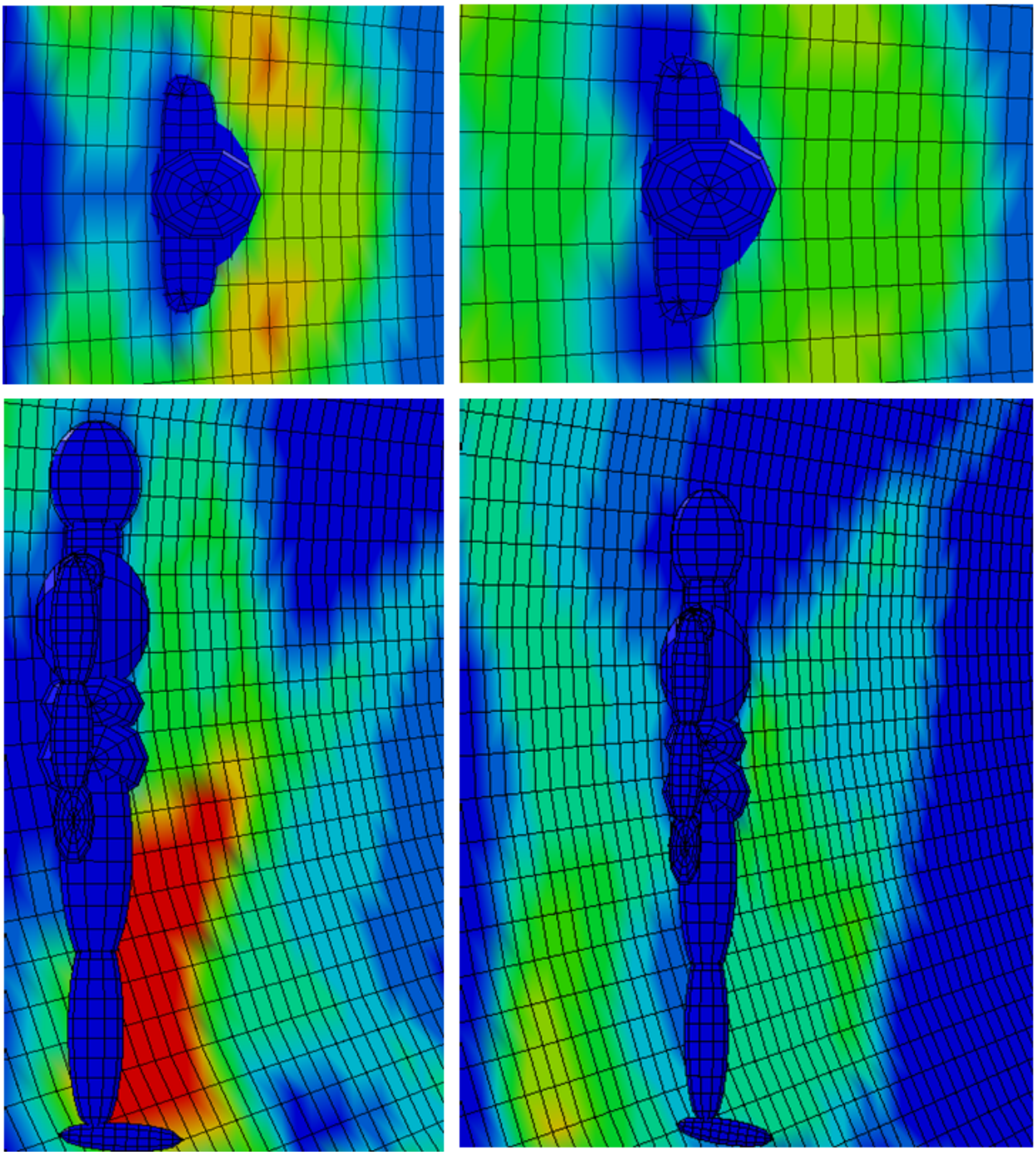

Figure 6-20 – Finish of blast shock wave interaction with the GEBOD at 3.5 m.

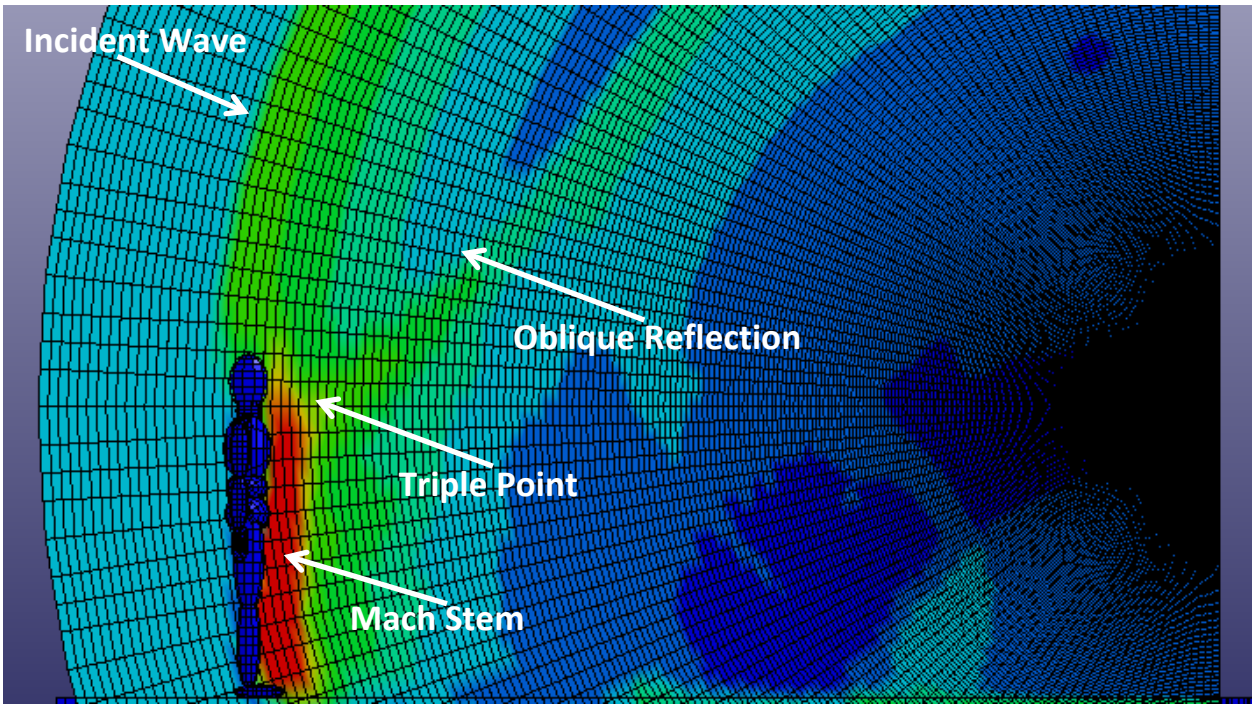

Figure 6-21 – Blast wave interaction with GEBOD at 5 m.

The blast wave causes a large acceleration peak from the incident wave and a second smaller acceleration from the oblique reflecting wave at 3.5 m, and 4 m (Figure 6-22). The GEBOD then has a single acceleration peak from the Mach stem once the triple point reaches head height at a standoff of approximately 5 m (Figure 6-22). The peak acceleration result for the spherical ALE model had good correlation with the experimental results and the LBE model, though gave slightly higher values at the 4 m and 5 m standoff distances (Figure 6-15).

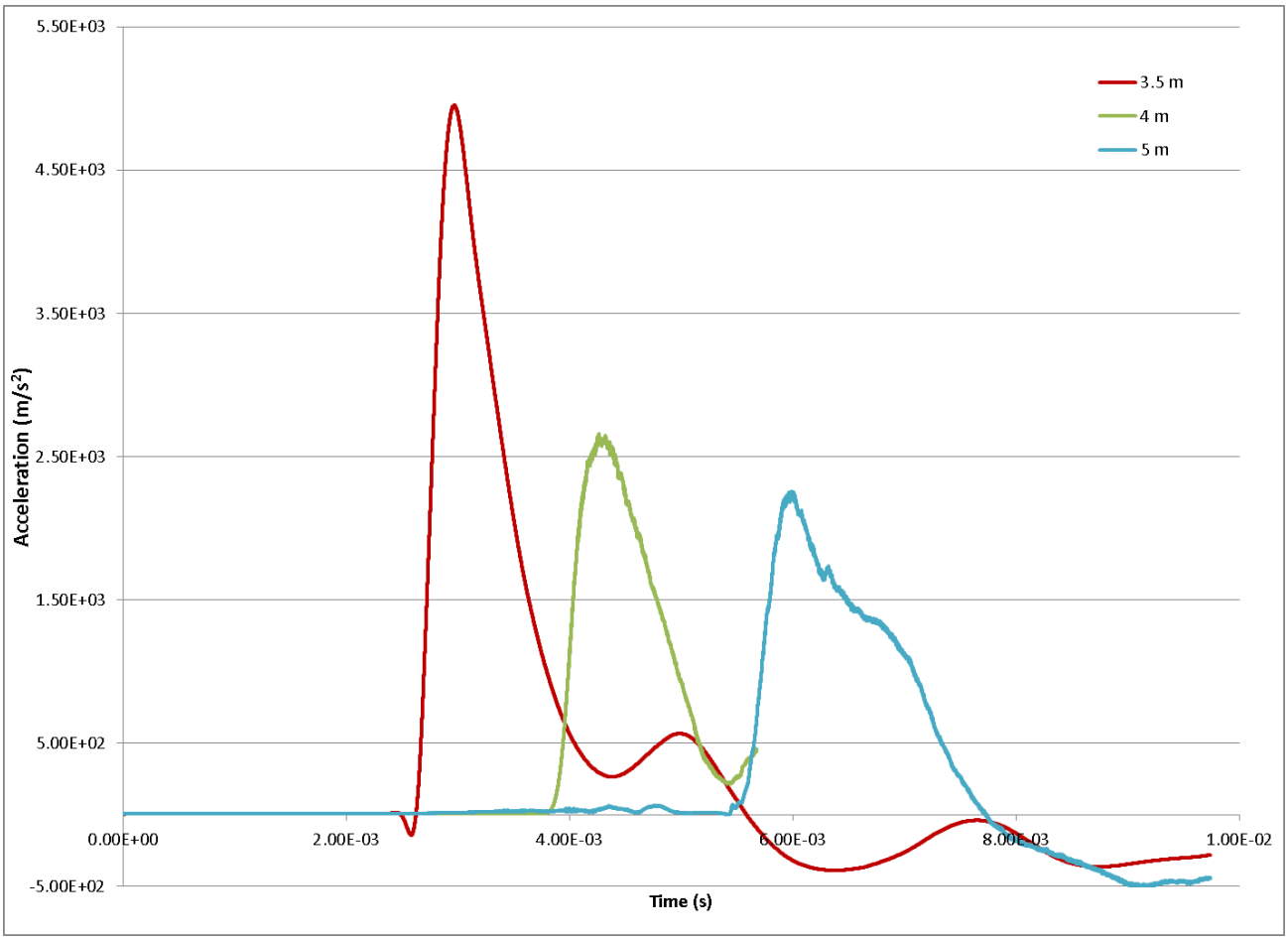

Figure 6-22 – Spherical ALE acceleration traces for 3.5 m, 4 m and 5 m standoff from 5 kg C4 explosive at 1.5 m HOB.

6.5 Head Injury Criteria

The Head Injury Criterion was developed for frontal car crashes with durations on the order of 10-100 ms, it has only been validated for those cases but was used here as an estimate for potential injury. The HIC takes into account the duration of the insult as well as the shape of the acceleration curve and results in a single value for each acceleration pulse which can be compared to tolerance levels used for auto crash.

6.5.1 LBE Model HIC Results

The predicted HIC_{15} results (Figure 6-23) followed a trend similar to the resultant acceleration with the close proximity blasts yielding HIC values greatly exceeding the tolerance level for all cases considered, followed by a quick degradation of the curve until the Mach stem effect caused an increase in the HIC values (Figure 6-23). As expected, larger explosive sizes resulted in higher acceleration values and thus a higher HIC_{15} value and potential for head injury. It is important note the drastic change from the near-field to mid-field distances. In each case the insult quickly degrades from greatly exceeding tolerance levels to a minor injury in only a few meters, this is due to the exponential decay of the pressure wave with increasing standoff.

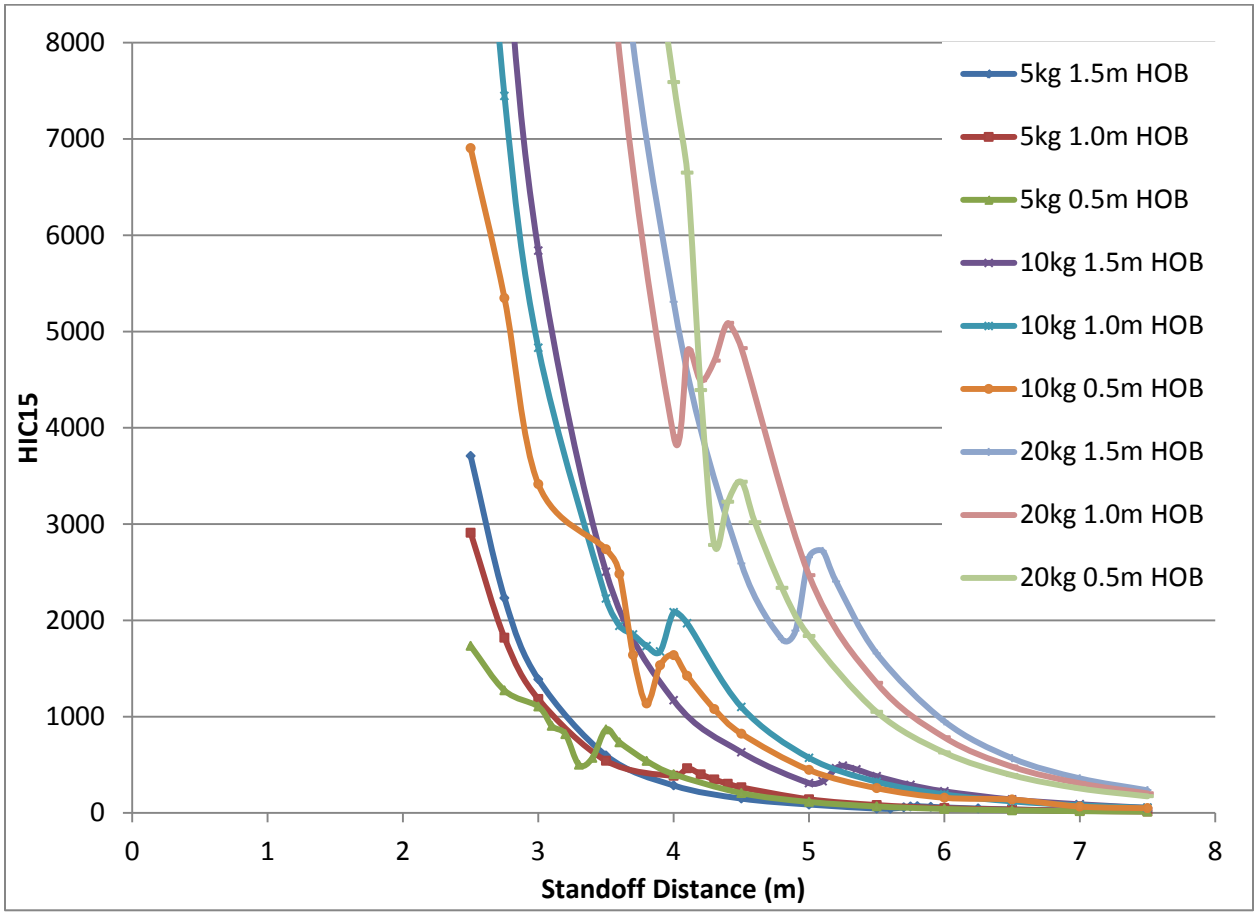

Figure 6-23 – LBE HIC_{15} versus standoff distance, for all explosive sizes and HOB.

6.5.2 HIC Comparison: Experimental vs. Spherical ALE Model and LBE Model

The HIC_{15} results calculated from the center of mass of the GEBOD for the LBE and spherical ALE models were compared to experimental tests carried out by the DRDC using a HIII dummy instrumented with accelerometers during a 5 kg C4 explosion at varying standoffs (Figure 6-24). The models were in good agreement with the overall trend of decreasing HIC with increased standoff seen in the experimental data. There is a large variation in the near-field DRDC data due to near-field blast inconsistencies. Both the LBE and ALE models overestimated the HIC_{15} in the mid-field distances and potential causes of this will be discussed in the next chapter.

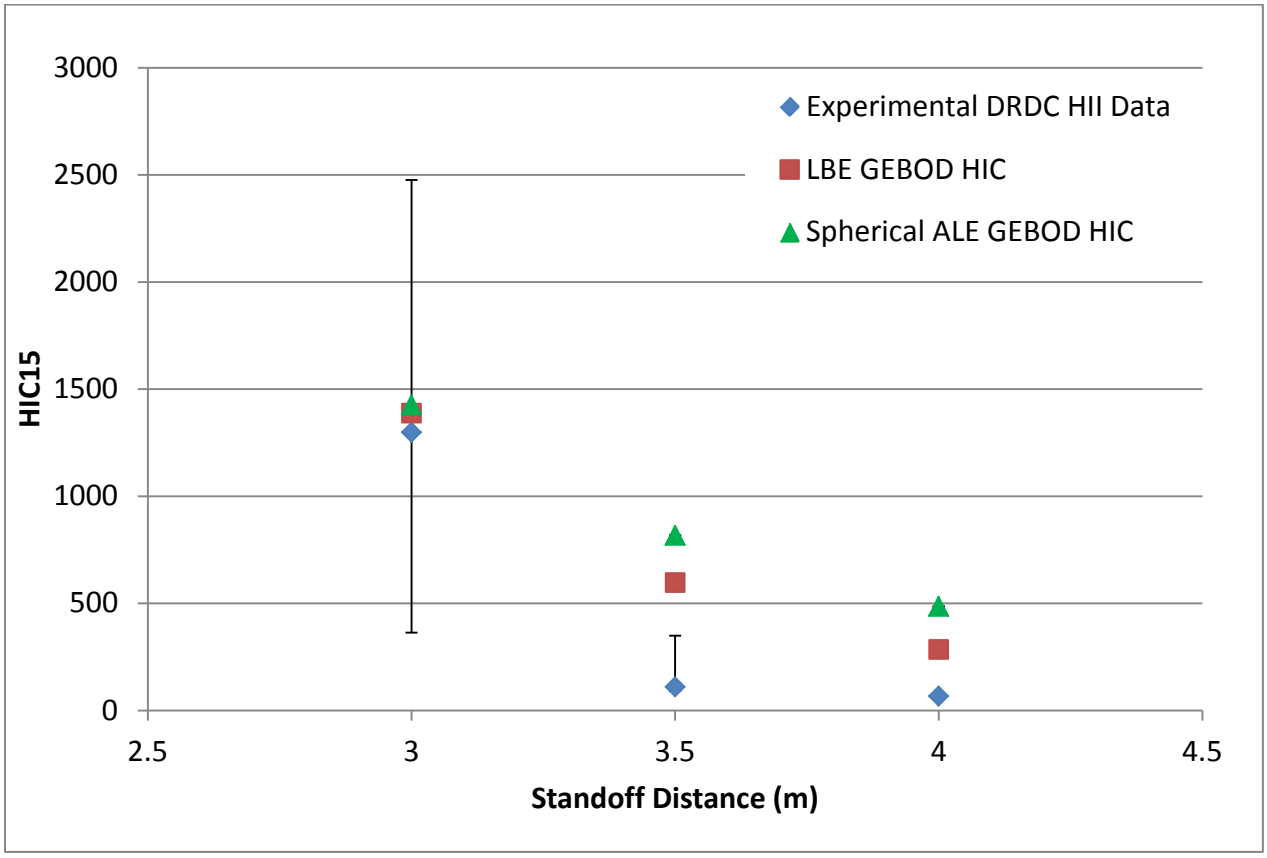

Figure 6-24 – Experimental vs. LBE and Spherical ALE HIC_{15} comparison.

6.6 Extended Prasad Mertz Curves

The extended Prasad Mertz curves are used to determine a probability percentage of a Maximum Abbreviated Injury Scale (MAIS) head acceleration injury based on a HIC_{15} value, (Equation 6-1).

Probability MAIS $$\%MAIS = \left(1 + e^{A+\frac{B}{HIC}-C*HIC}\right)^{-1}$$ *Equation 6-1*

[NHTSA, 2013]

Where: The Prasad/Mertz Parameters are:

MAIS	A	B	C
1	1.54	200	0.0065
2	2.49	200	0.00483
3	3.39	200	0.00372
4	4.9	200	0.00351
5	7.82	200	0.00429
6	12.24	200	0.00565

In order to allow for a more convenient injury prediction these separate injury probabilities can then be resolved into an average AIS level injury (Equation 6-2; Figure 6-25).

$$AIS_{avg} = \frac{\%MAIS1 * 1 + \%MAIS2 * 2 + \%MAIS3 * 3 + \%MAIS4 * 4 + \%MAIS5 * 5 + \%MAIS6 * 6}{6!} * 6$$

Equation 6-2

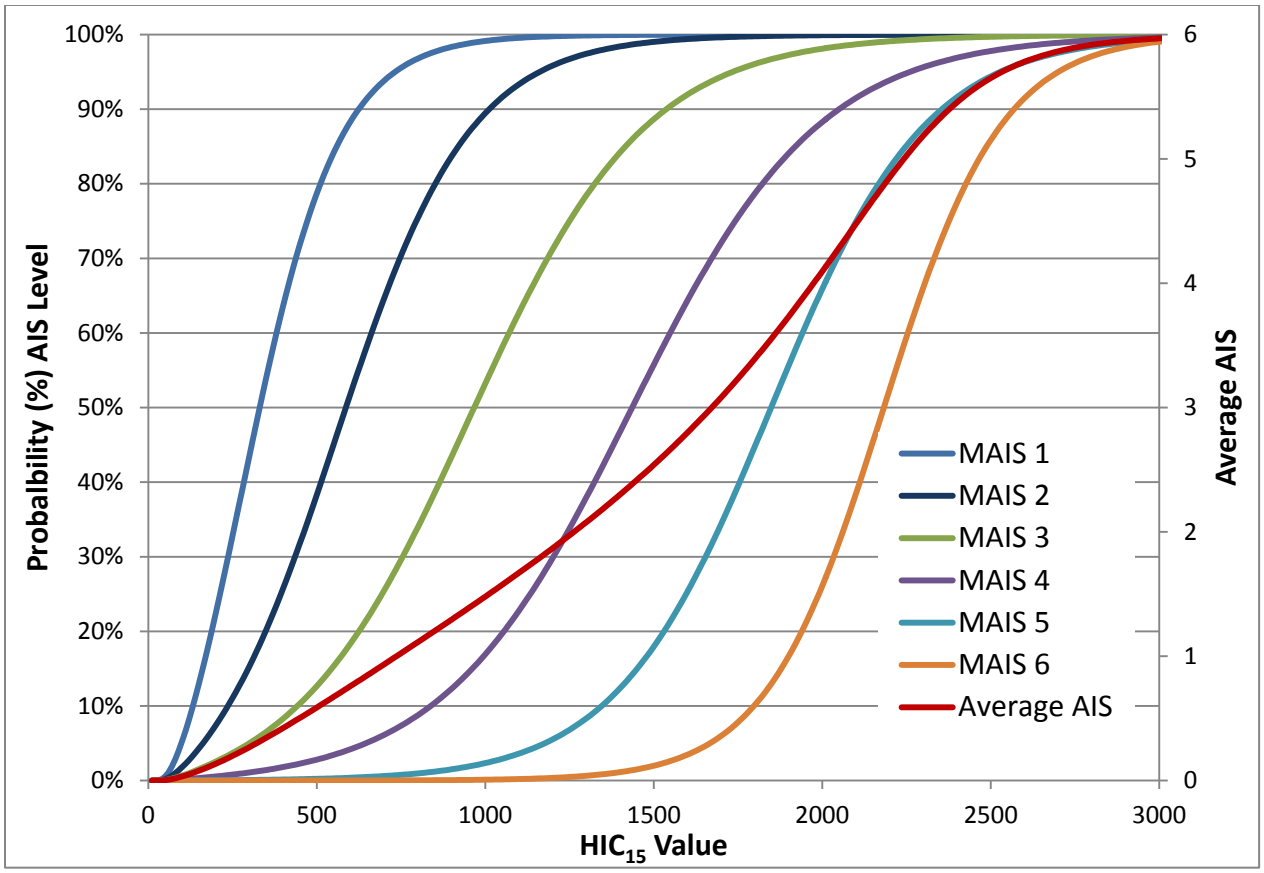

Figure 6-25 – Extended Prasad/Mertz Curves with an average AIS level injury curve vs. HIC.

6.6.1 LBE Average AIS Injury Level

There is a large probability of maximal level of injury in the near field for all cases considered, (Figure 6-26). All charges have the potential to deliver maximal injury until a scaled distance (Z: Equation 2-27), of 1.5 m/kg$^{1/3}$ has been reached, at this point there is a drastic reduction of the insult until minor or no injury is reached past 2.2 m/kg$^{1/3}$ (Figure 6-27). The 5 kg charge had potential to cause maximal injury only inside 2.5 m which is essentially inside the explosive fireball, the AIS level associated with a 5 kg charge quickly degraded until outside of 3 m there is only probability for minor or no injury caused by acceleration. For 10 kg charges there was a potential for maximal injury inside of 3.6 m, the Mach stem has a larger potential to increase

the potential injury zone here than in the 5 kg case especially in the lower heights of burst scenarios. For a probability of minor or no injury in the 10 kg case a subject would have to be approximately 4.5 m to 5 m from the blast. The 20 kg charges had potential to cause maximal injury inside a radius of 5.2 m, and the surrogate was only subject to minor or no injuries outside of 6 m. The Mach stem effect cannot be seen for the lower height of bursts as they happen above an AIS level 6 injury; however, the 20 kg 1.5 m HOB Mach stem increased the potential injury zone for maximal injury an additional 0.4 m.

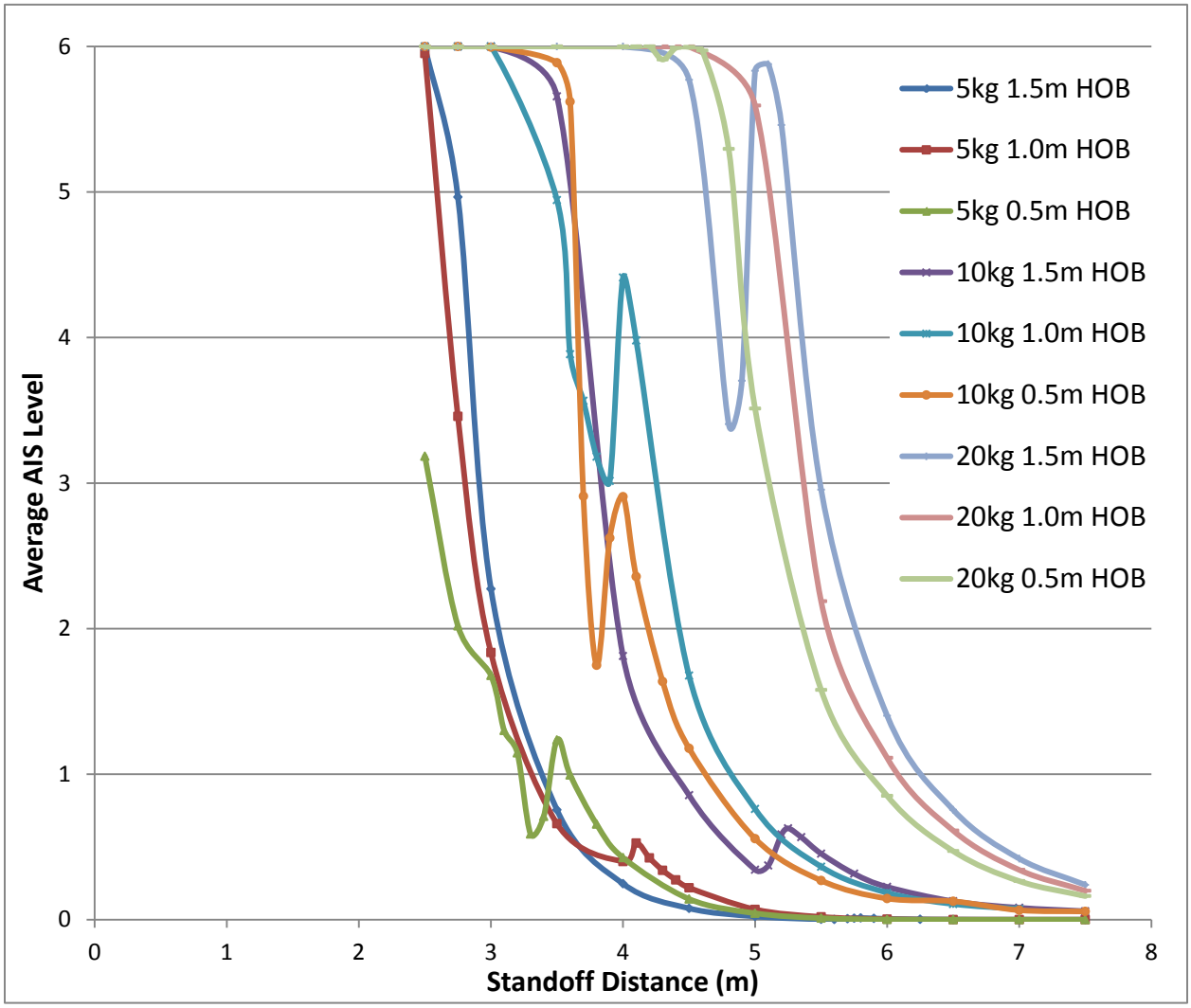

Figure 6-26 – Average AIS head acceleration injury from Load Blast Enhanced model vs. standoff distance.

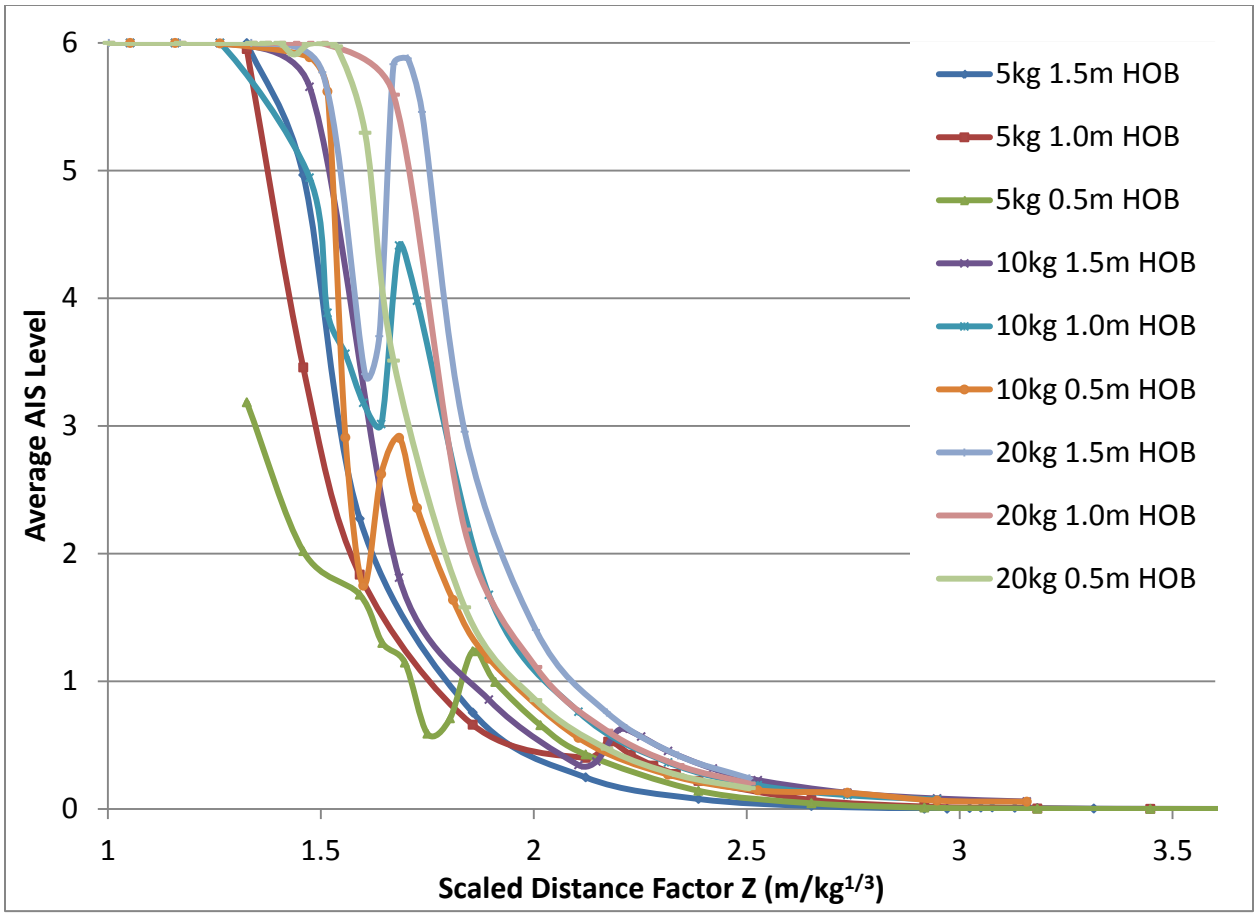

Figure 6-27 – Average AIS head acceleration injury vs. Scaled Distance Factor ($Z = m/kg^{1/3}$).

It is important to note the drastic transition in the insult from an AIS level 6 injury to level 1 or no injury over only a few meters in each case.

6.6.2 Experimental vs. LBE and Spherical ALE Probability MAIS and Average AIS

The higher acceleration values and durations observed in the LBE and ALE models give a higher HIC_{15} value and thus a higher probability of a maximum AIS injury and a higher AIS average (Table 6-8). Though the models results are of the same order of magnitude as the experimentally observed values the FEM models are overestimating the insult and injury caused in blast scenarios. The values gained from the experimental tests have a level of variability

associated with their results; the values obtained from the DRDC HIII study may not be exact in their answer due to experimental scatter and the low level of sample tests performed.

Table 6-8 – Experimental vs. LBE and spherical ALE probability of MAIS and average AIS.

	HIC_{15}	MAIS 1	MAIS 2	MAIS 3	MAIS 4	MAIS 5	MAIS 6	AIS_{AVG}
DRDC 3 m	1298	100%	98%	78%	38%	8%	1%	2.076
LBE 3 m	1388	100%	99%	84%	46%	12%	1%	2.275
ALE 3 m	1426	100%	99%	86%	49%	14%	1%	2.362
DRDC 3.5 m	110.2	7%	12%	1%	0%	0%	0%	0.09902
LBE 3.5 m	597.2	88%	60%	18%	4%	0%	0%	0.8021
ALE 3.5 m	817.1	97%	81%	36%	9%	1%	0%	1.167
DRDC 4 m	67.05	2%	10%	0%	0%	0%	0%	0.06613
LBE 4 m	285.2	40%	25%	5%	1%	0%	0%	0.3082
ALE 4 m	485.8	77%	46%	12%	3%	0%	0%	0.6211
LBE 5 m	86.91	4%	11%	0%	0%	0%	0%	0.08001
ALE 5 m	359.7	56%	32%	7%	1%	0%	0%	0.4201

7 Discussion

This study is part of a multi-scale modelling approach to predict head injury from blast, in parallel with a study to investigate blast head injury at the tissue level using detailed sagittal and transverse slice models of the human head to investigate brain blast injuries [Singh et al., 2013]. The detailed head models have demonstrated a link between overpressure insult and the head response in terms of kinematics, HIC, intracranial pressure, and brain tissue stresses. This study focused on the response of the head in large scale simulations of blast scenarios, where the 3D wave interaction with the GEBOD can be used to setup initial conditions in a multi-scale approach enabling a more accurate simulation environment. For example, the results of these analyses can be applied as boundary conditions to the detailed head models to investigate complex blast scenarios.

To numerically simulate the interaction of blast with the human body two finite element approaches were investigated: an uncoupled enhanced blast method, and a fully coupled Arbitrary Lagrangian Eularian mesh formulation. The models were assessed using experimental blast tests performed at DRDC Valcartier, and with the widely used ConWep blast effects database. Parameters compared between the models and experimental values included: peak pressure, arrival time, impulse, and pressure wave curve shape.

The LBE model is less computationally expensive than the ALE model with numerical simulation run times of eight hours compared to twelve days for the ALE model using a 36 core mpp cluster system. The short run times for the LBE model enable the completion of parametric studies for multiple blast scenarios; however, this method provides only a limited amount of

results as it only evaluates the target subject not the explosive detonation wave, shock wave propagation, reflection, or subsequent 3D wave interaction.

The Spherical ALE model allowed for a more complete evaluation of an explosive incident including the detonation wave, shock wave development and propagation, explosive material contact surface observation (fireball), blast wave reflection, as well as subsequent impact, reflection and refraction around a subject. The ability to observe the wave interactions with a subject cannot be understated as it is challenging to observe in an experimental environment and may prove useful in understanding how the wave interacts with a surrogate and the ensuing wave propagation through tissue. This model is computationally expensive with 4.6 million elements, and performing a large parametric study using this model would be prohibitive; however, if a blast scenario is of specific interest to a researcher this method provides an immense amount of data, and can provide insights that may not otherwise be measurable in experimental tests.

The numerical models were used to evaluate blast interaction with the human body in order to identify the potential for primary brain blast injury using global head kinematics. The GEBOD multi body model was used as a numerical human surrogate to evaluate the resultant acceleration of the center of mass of the head and the correlated HIC_{15} value for a multitude of standoffs and explosive sizes. The GEBOD model provided the required insight into global head kinematics. Other surrogates including the Hybrid III and full detailed body models were considered; however, they are still computationally prohibitive and the geometry of these models would present significant coupling challenges for the ALE method. It was demonstrated

that the GEBOD approach provides a good estimate of head kinematics compared to experiments and was found to be suitable for the current study.

ConWep provides data for free field blast scenarios (an incident blast wave with no ground reflection or Mach stem effects). The incident wave impulse reported by ConWep was higher than the experimental DRDC results. Comparing the two data sets, it was found that ConWep follows the Friedlander curve (Equation 2-28) and has longer positive phase duration compared to the DRDC pressure traces. The LBE model implemented in the finite element code use for this study is based on the ConWep databases and simulates an ideal reflection from a defined ground plane, thus the enhanced blast model overestimated the total impulse of a blast wave compared to DRDC experimental averages by 30-60%, due to the higher impulse reported in the incident and reflected wave. The LBE model incident wave had a better correlation to ConWep in terms of impulse, arrival time, and peak pressure. The Spherical ALE model was in good correlation for all pressure results with a maximum difference of 11% compared to ConWep data and DRDC experimental observations; this difference is within the corridor of variability of the experimental test data.

Both models predicted accelerations that were in good agreement, but overestimated the insult compared to experimental results in the mid to far field distances. In the case of the enhanced blast model the overshoot was due to the higher impulse simulated in the blast wave versus the experimental results. For the ALE spherical blast model this overshoot correlated to the smearing of the shock wave over several elements creating longer duration acceleration and thus a higher HIC_{15} value. The Head Injury Criteria has been shown to produce comparable

tolerance results to the Head Impact Power and Rotational injury metrics [Cronin et al., 2008]. Although HIC_{15} provides a useful benchmark for evaluating model response, it should be noted that the HIC was developed for the automotive industry and usually utilized for load durations longer than those applicable to blast.

Increasing the standoff distance resulted in a reduction in peak acceleration until the Mach stem effect reached the height of the GEBOD head, which caused an increase in acceleration. The Mach stem effect instantaneously increased the applied pressures when the triple point height reached the head height, leading to an increase in both duration and peak acceleration thus expanding the potential injury zone up to 0.25 $m/kg^{1/3}$ surrounding a raised charge.

An average Abbreviated Injury Scale produced from extended Prasad-Mertz curves based on automotive tolerance levels was used to estimate the injury level from various blast scenarios. The models predicted a high level injury for all cases considered in the near-field (inside a scaled distance of 1.5 $m/kg^{1/3}$), followed by a drastic reduction of the injury curve to minor or no injury outside of 2.2 $m/kg^{1/3}$. In the close proximity blast scenarios there was a rapid acceleration of the head over approximately 1 ms, and as expected the larger explosive sizes resulted in a greater insult and higher degree of injury. The 20 kg case caused an AIS 6 injury due to head acceleration until a standoff of 5.2 m was reached and AIS 1 injury was only observed from a distance of greater than 6 m. For the 5 kg case the average AIS predicted AIS 2 injury due to head acceleration for the 3 m standoff case, and minor or no injury for the 3.5 m and 4 m cases. The importance of this data is not the specific distances associated with injury but the observable drastic exponential reduction in the insult force and potential injury

received with increased standoff distance outside of the near-field region of an explosive charge.

7.1 Study Limitations

The models in this study do not cover the full regime of blast injury threats such as fragmentation (secondary blast injury), surrogate impact with surrounding structures (tertiary blast injury), or heat and other effects (quaternary blast injury).

This study used injury metrics developed for automotive crash injury as there are no validated blast injury metrics currently available, thus the predicted injury trends should be only taken as estimates of injury level.

Experimental and numerical simulation of the human body is limited to biomechanical details that are challenging to measure in a live human subject, such as intracranial pressure or specific measures of deformation for tissue damage. Thus surrogates are used to predict injury by estimating the magnitudes and directions of forces applied. These surrogate models often have a varying level of biofidelity and biofidelic frangibility (mimicking and failing as the human body would); as such, both numerical models and experimental surrogates can only be used to predict injury for the insult they were designed for. Once the test is complete the results must be analyzed against clinical data to determine the degree of accuracy. Biofidelic surrogate models for blast have yet to be validated to determine if they can predict an observed injury; however, current models can be used to define a parameters priority and estimate the insult as well as resultant injury level given a scenario.

8 Summary and Conclusions

In modern conflicts over 81% of all casualties are the result of an explosive incident [Owens et al., 2008]. This is the highest percentage of injury ever attributed to explosives in warfare, and is largely the result of the increase in size and prevalence of IEDs being used on the battlefield. In the past blast injuries were mostly attributed to pulmonary trauma, however recently blast overpressure has been linked varying levels of traumatic brain injury [Saatman et al., 2008]. This increase in prevalence of TBI is due to several factors: the increase in survivability from pulmonary injury due to more effective body armour [Wood et al., 2012], the increased size and prevalence of explosives being used, and an increased awareness in the medical field of diagnosing mild traumatic brain injury and casualties who may have been suffering from comorbid post-traumatic stress disorder.

The injury mechanism behind primary blast brain injury is not well understood at present, this difficulty stems from the inability to observe or measure intracranial phenomena in living subjects, the extreme accelerations of the head experienced in a blast scenario, and the complex interactions between the blast wave and the human body. When a blast wave reaches a human body the wave interacts with the subject creating a large acceleration as a result of the pressure differential and produces a high frequency stress wave that propagates through the tissue. Several injury criteria have been proposed to set a threshold for this insult including: global head acceleration (HIC), peak incident pressure, and dynamic intracranial pressure [Singh et al., 2013].

This study was performed using explicit finite element method to model high explosive blast incidents and their interaction with a multi-body GEnerator of BOdy Data human surrogate to predict global head kinematics and correlate to existing injury criteria. Two modelling approaches were investigated and assessed using experimental data provided by the DRDC Valcartier and each other to validate and compare their results. It was determined that the uncoupled enhanced blast method predicted reasonable peak pressures, arrival times, and duration; however, overestimated the impulse compared to experimental data leading to a higher predicted HIC_{15} value. The coupled Arbitrary Eularian Lagrangian models pressure results were in good agreement with experimental pressure observations with under an 11% difference against both ConWep and DRDC data; however, over predicted the HIC_{15} value when compared to DRDC data. The spherical models HIC_{15} overestimate is due to the smearing of the shock wave over several elements resulting in a longer duration loading and thus a larger HIC_{15} value. Both models were in good correlation to one another with a reduction in peak acceleration with increasing standoff until the Mach stem effect reached the head height of the surrogate instantaneously increasing the applied peak pressure and duration thus expanding the potential injury zone by up to 0.25 $m/kg^{1/3}$ surrounding a raised explosive. It is important to note the drastic reduction in insult from an AIS level 6 injury to an AIS level 1 injury over only a few meters. The potential injury received decreases exponentially with increasing standoff distance gained outside of the near-field regime of a blast event.

The HIC_{15} metric should only be used as an injury benchmark for evaluating the model response; it was developed for the automobile industry and usually utilized for loading durations longer than those applied in blast scenarios. Care should be taken in using numerical

and experimental surrogates in blast scenarios, they should only be used for the type and direction of impact they were designed for, with all simulated and experimental results analyzed against clinical data to determine the relative degree of accuracy.

The enhanced blast model is less computationally expensive than the Arbitrary Lagrangian Eularian model, and can be simulated to completion within eight hours; however, it allows for only the evaluation of the target and not of the whole blast incident. The Arbitrary Lagrangian Eularian method allows for a more complete picture of a blast scenario, including over 4.6 million elements where data on pressure, impulse, density, and temperature can be analyzed. This enables analysis of the detonation wave, near-field explosive fireball expansion, blast wave propagation, wave reflection, target interaction and resultant motion. This model has also provided insight to the 3D wave interaction with a human subject which could be used to enable more accurate boundary and initial conditions to 2D head slice models and eventual 3D head models. As this model is computationally expensive it is useful for research into a specific blast scenarios, and has the ability to be scaled to different explosive sizes, explosive positions or to include surrounding objects and multiple surrogates.

The major accomplishment of this study is the development of the first Arbitrary Lagrangian Eularian model to simulate full three dimensional blast scenarios capable of resolving wave dynamics, and target kinematics enabling injury prediction.

9 Recommendations for Future Work

Applying these models to a biofidelically frangible surrogate would enable thorough insight into understanding blast brain injury. Experimental biofidelic head models are currently being developed but have yet to be fully validated; for validation to be possible more research into in-vivo brain material properties and their non-linear response to high strain rate insult is necessary. A fundamental understanding of the injury mechanics of primary blast traumatic brain injury is required in order to set injury thresholds and criteria; the current thresholds set by the automotive industry are to predict injury from accelerations in crash scenarios and utilize profoundly different durations and magnitudes.

A larger parametric study involving the spherical ALE model should be undertaken at multiple heights of burst and larger standoffs to ensure further validation in different cases; this model also has the ability to include structures and or vehicles into the analysis which could expand its contributions. The cylindrical ALE model should be further developed to include a ground reflection to allow for evaluation of ground effects of a cylindrical charge. This is the primary charge shape that is used in experiments and thus this model could explain some of the disparities seen in the enhanced blast model and the spherical ALE model.

As computational ability increases these models should be further refined creating smaller elements and more accurate modeling of shock wave propagation. Also with increasing computational ability 3D biofidelically frangible head and full body models should be used in place of multi-body surrogates and 2D slice models to measure global, macro, and micro scale blast effects on the body and tissue level.

References

Alia A., Souli M. (2006). *High explosive simulation using multi-material formulations*. Applied Thermal Engineering, 26(10), 1032-1042

ASME (American Society of Mechanical Engineers). (2007). *An overview and Some Motivation Guide for Verification and Validation in Computational Solid Mechanics*. 1-15

Azevedo FAC, Carvalho LRB, Grinberg LT, Farfel JM, Ferretti REL, et al. (2009). *Equal numbers of neuronal and nonneuronal cells make the human brain an isometrically scaled-up primate brain*. The Journal of Comparative Neurology 513 (5): 532-541.

Baker W. E. (1973). *Explosions in air*. University of Texas Press.

Bhaskaran K., Roth P., *The shock tube as wave reactor for kinetic studies and material systems*, Progress in Energy and Combustion Science, Volume 28, Issue 2, 2002, Pages 151-192, ISSN 0360-1285, 10.1016/S0360-1285(01)00011-9.

Bass C.R., Rafaels K.A., and Salzar R.S. (2008). *Pulmonary injury risk assessment for short-duration blasts*. J. Trauma 65, 604–615.

Bogo V., Hutton R.A., Bruner A. (1971). *The effects of airblast on discriminate avoidance behavior in rhesus monkeys*. Lovelace Foundation for Medical Education and Research. Albuquerque, New Mexico, DASA 2659.

Bonet J., Burton A. (1998). *A simple average nodal pressure tetrahedral element for incompressible and nearly incompressible dynamic explicit applications*. Communications in Numerical Methods Eng. 14(5):437–449.

Bowen I.G., Fletcher E.R., Richmond, D.R. (1968). *Estimate of man's tolerance to the direct effects of air blast*. Lovelace Foundation for Medical Education and Research. Albuquerque, New Mexico, DASA 2113

Cernak I., Savic J., Ignjatovic D., Jevtic M. (1999). *Blast injury from explosive munitions*. The Journal of Trauma: Injury, Infection, and Critical Care 47 (1): 96-103.

Cernak. (26, April 2011). *The truth about traumatic brain injury*. Retrieved from http://www.idga.org/military-medicine/articles/the-truth-about-traumatic-brain-injury

Chafi M., Karami G., Ziejewski M. (2010). *Biomechanical assessment of brain dynamic responses due to blast pressure waves*. Annals of Biomedical Engineering 38 (2): 490-504.

Cheng H., Obergefell L., Rizer A. (1994). *Generator of Body (GEBOD) Manual*. Wright-Patterson Air Force Base, Ohio : Air Force Materiel Command.

Cheng S-Y., Hsu H-T. (2011). *Mental Fatigue Measurement Using EEG, Risk Management*

Trends, Prof. Giancarlo Nota (Ed.), ISBN: 978-953-307-314-9, InTech, DOI: 10.5772/16376.

Clemedson C.J. (1949). *An experimental study on air blast injuries*. Acta Physiol. Scand. 18, 1–200.

Cowles R. A. (2007) *MedlinePlus Medical Encyclopedia: Skull*. MedlinePlus. [Online] U.S. National Library of Medicine and the National Institutes of Health, http://www.nlm.nih.gov/medlineplus/ency/images/ency/fullsize/9057.jpg.

Cronin D., Salisbury C., Binette J.S., et al. (2008). *Numerical modeling of blast loading to the head*, Proc. Personal Armour Systems Symp., Brussels, Belgium, 84-93.

Cronin D. (2011). *Explicit Finite Element Method Applied to Impact Biomechanics Problems*. IRCOBI Keynote

Cronin D. (2012). *Mechanical Engineering 720 Impact Biomechanics Course Notes*, University of Waterloo.

Desmoulin, G. T. and Dionne, J-P. (2009). *Blast-Induced Neurotrauma: Surrogate Use, Loading Mechanisms, and Cellular Responses*. s.l. : Lippincott Williams & Wilkins, Inc. The Journal of Trauma: Injury, Infection, and Critical Care, Vol. 67(5), pp. 1113-1122.

Dionne J-P., Nerenberg, Makris A. (1997). *Reduction of Blast-Induced Concussive Injury Potential and Correlation With Predicted Blast Impulse*. Med-Eng Systems Inc..

Dobratz, B. M. (1981). *Lawrence Livermore National Laboratories Explosives Handbook - Properties of Chemical Explosives and Explosive Simulants*. Lawrence Livermore National Laboratory.

DVBIC: Defense and Veterans Brain Injury Center. (2013). *DoD numbers for Traumatic Brain Injury*; Data Provided by Defense Medical Surveillance System, recovered from http://www.dvbic.org/sites/default/files/uploads/2000-2013%20up%20to%20Q2-dod-tbi-worldwide-2000-2013-Q2-as-of-Q1-Q2-13_01-08-13RDS.pdf, October 2013

Flynn M. (2009). *State of the Insurgency - Trends, Intentions and Objectives. ISAF, Afghanistan,* (22 December 2009). Retrieved from http://www.airforce.forces.gc.ca/CFAWC/Contemporary_Studies/2009/2009-Dec/2009-12-22-State_of_the_Insurgency_Trends_Intentions_and_Objectives_e.asp

Gruss E. (2006). *A Correction for primary blast injury criteria*. Journal of Trauma. 60, 1284 – 1289.

Ganpule S., Alai A., Plougonven E., Chandra N. (2013). *Mechanics of Blast Loading on the Head Models in the Study of Traumatic Brain Injury Using Experimental and Computational Approaches*. Biomechanics and modeling in mechanobiology 12(3): 511–31.

Gehre C. (2009). *Objective Rating of Signals Using Test and Simulation Responses*, Paper Number 09-0407, 2009

Greer A. (2006). *Numerical Modeling for the Prediction of Primary Blast Injury to the Lung*. MASc Thesis. Waterloo, ON : s.n.

Goldsmith W. (1981). *Current controversies in the stipulation of head injury criteria,* Letter to the Editor. J. Biomech. 14, 883-884

Gupta R., Przekwas A. (2013). *Mathematical models of blast induced TBI: current status, challenges and prospects*, Frontiers in Neurology 4 (59)

Gurdjiian E., Roberts V., Thomas L. (1966). *Tolerance curves of acceleration and intracranial pressure and protective index in experimental head injury.* J. Trauma 6, 600-604

Haladuick T., Lockhart P., Singh D., Cronin DS. (2012).*Head kinematics resulting from simulated blast loading scenarios*. *Proc. PASS*, Nuremberg, Germany.

Hallquist J. *LS-Dyna Theory Manual*. Livermore Software Corporation, 2006

Hinricsson H. (1970). *Une Observation jamais encore relevée de D.-J. Larrey*, Revue de Corps de Santé, 11: 761-763, 1970.

Hole J. (1984). *Jr. Human Anatomy and Physiology*. 3rd Edition. Dubuque : Wm. C. Brown Publishers. ISBN 0-697-04790-3.

Hollinshead W., Rosse C. (1985). T*extbook of anatomy*, 4 ed. Harper and Row, Philadelphia, PA.

Hooker, D.R. (1924). *Physiological effects of air concussion*. Am. J. Physiol. 67, 219–274.

Humanetics Innovative Solutions, http://www.humaneticsatd.com/crash-test-dummies/frontal-impact/hybrid-iii-50th, Recovered October 2013.

Hutchinson J., Kaiser M., Lankarani H. (1998). *The Head Injury Criterion (HIC) functional*. Applied Mathematics and Computation, Vol. 96. PII: S0096-3003(97) 10106-0.

Hyde. D. (1998). F*undamentals of Protective Design for Conventional Weapons' (User's Guide)*. Microcomputer Programs ConWep and FUNPRO, Applications of TM 5-855-1, Report ADA195867. Vicksburg, MS: Department of the Army, Waterways Experiment Station, Corps of Engineers.

Kapit W. Elson L. (2001). Anatomy Coloring Book, Pearson Education

Karami G., et al., *A micromechanical hyperelastic modeling of brain white matter under large deformation*, Journal of the Mechanical Behavior of Biomedical Materials, Vol. 2, pp. 243-

254. Elsevier, 2009

Kinney, G. F. (1962). *Explosive Shocks in Air* (New York: The Macmillan Company)

Lockhart P., Cronin D., Williams K., Ouellet S. (2011). *Investigation of head response to blast loading*, J. Trauma, 70(2), E29-36.

Loth F., Yardimci M., Alperin N. (2001) *Hydrodynamic Modeling of Cerebrospinal Fluid Motion Within the Spinal Cavity s.l. :* ASME, February 2001, Journal of Biomechanical Engineering, Vol. 123, pp. 71-79.

LSTC (Livermore Software Technology Corporation). (2010). *Ls-dyna keyword user's manual*. (Version 971/Rev 5)

LSTC (Livermore Software Technology Corporation). (2008). *Enhanced Blast Loading in LS-DYNA. [LS-Dyna Theory Manual], Livermore*, CA : Livermore Software Technology Corporation, 2008.

Manseau J. et al. (2006). *Response of the Hybrid III Dummy Subjected to Free-Field Blasts – Focussing on Tertiary Blast Injuries*. s.l. : MABS.

Margulies. (2011). Keynote speech IASTED 2011

McKinley M. O'Loughlin V. (2008). *Human Anatomy 2nd Edition*. New York, NY, USA : McGraw-Hill. ISBN 978-0-07-296549-0.

Meyers, M. (1994). *Dynamic Behavior of Materials*. s.l. : Wiley-IEEE.

Mitchell S., Morehouse G., Keen Jr. (1864). *Reflex Paralysis*, Circular #6, Surgeon General's Office, Washington, DC.

Moore K., Dalley A. (1999). *Clinically Oriented Anatomy 4th Edition*. Baltimore : Lippincott Williams & Wilkins. ISBN 0-683-06141-0.

Mukherjee R. (2011) , *Advanced Gas Mechanics, National programme on technology enhanced learning*, https://www.youtube.com/watch?v=i-7IivttOjY

Nahum A., Melvin J. (2002). *Accidental injury – biomechanics and prevention*, 2nd edition, New York, NY: Springer.

National Cancer Institute. (2013). recovered from http://abc2.org/get-informed/brain-tumor-facts, October 2013.

National Highway Traffic Safety Administration
http://www.nhtsa.gov/cars/rules/rulings/80g/80gii.html

National Highway Traffic Safety Administration. (2013). http://www-

nrd.nhtsa.dot.gov/vrtc/bio/adult/adult.htm, 2013

Operation enduring freedom fatalities. (20/06/2013). Retrieved from http://icasualties.org/OEF/Fatalities.aspx

Ouellet S., Bouamoul A., Gauvin R., Binette J.S., Williams K., Martineau L., *Development of a Biofidelic Head Surrogate for Blast-Induced Traumatic Brain Injury Assessment, PASS Proceedings 2012*

Owens B., Kragh Jr J., Wenke J., Macaitis J., Wade C., et al. (2008*). Combat Wounds In Operation IraqiFfreedom And Operation Enduring Freedom*. Journal of Trauma 64 (2): 295-299.

Panzer M., Myers B., Capehart B., and Bass C. (2012). *Development of a finite element model for blast brain injury and the effects of csf cavitation*. Annals of Biomedical Engineering 40 (7): 1530-1544.

Panzer M., Myers B., and Bass C. (2013). *Mesh Considerations for Finite Element Blast Modelling in Biomechanics*. Computer methods in biomechanics and biomedical engineering 16(6): 612–21. http://www.ncbi.nlm.nih.gov/pubmed/22185582 (November 3, 2013).

Petes J. (1986), *Handbook of HE Explosion Effects*, DASIAC-TN-86-15, Defense Nuclear Agency, Washington, DC, USA.

Prasad P., Mertz H., *The position of the United States Delegates to the ISO Working Group 6 on the Use of HIC in the Automotive Environment*, SAE Paper Number 85-1246, Society of Automobile Engineers, Warrendale, PA, 1985

Reddy J.N. (2005). *An Introduction to the Finite Element Method* (Third ed.). McGraw-Hill. ISBN 9780071267618.

Richmond D., White C. (1962). *A tentative estimation of man's tolerance to overpressures from air blast*. Lovelace Foundation for Medical Education and Research. Albuquerque, New Mexico, DASA-1335

Richmond D. et al. (1985) *Biologic Response to Complex Blast Waves*. Los Alamos, New Mexico : Los Alamos National Laboratory.

Ritzel D.,Parks S. (2011). *Experimental Blast Simulation for Injury Studies.* RTO-MP-HFM-207 - A Survey of Blast Injury across the Full Landscape of Military Science.

Roache P. (1998). Verification and Validation in Computational Science and Engineering. Albuquerque, New Mexico : hermosa publishers. ISBN 0-913478-08-3.

Saatman K., Duhaime A., Bullock R., Maas A., Valadka A., Manley G. (2008); *Workshop Scientific Team and Advisory Panel Members. Classification of traumatic brain injury for*

targeted therapies.Journal of Neurotrauma. 25, 719-738

Schmitt K-U., Niederer P., Muser M., Walz F., *Trauma Biomechanics*, Third Edition, Springer, Berlin, 2010.

Schmitt K-U., Niederer P., Cronin D. Muser M., Walz F. (2014). *Trauma Biomechanics: An introduction to injury biomechanics,* Fourth Edition, Springer, Berlin.

Singh D., Cronin D., Haladuick T. (2013). *Head and brain response to blast using sagittal and transverse finite element models.* International Journal for Numerical Methods in Biomedical Engineering.

Smith P., Hetherington J. (1994). *Blast and Ballistic Loading of Structures* (Burlington, MA:Butterworth-Heinemann).

Souli M.(2004). *LS-Dyna Advanced Course in ALE and Fluid/Structure Coupling*. Livermore Software Corporation.

Stuhmiller J., Phillips Y., Richmond D. (1991). *Chapter 7 THE PHYSICS AND MECHANISMS OF PRIMARY BLAST INJURY, Conventional Warfare: Ballistic, Blast, and Burn Injuries*; Office of the Surgeon General.

TM5-1300. (1991). *Design of Structures to Resist the Effects of Accidental Explosives*. Departments of the Army, The Navy, and The Airforce. (1990), 1991

Warden D., Ryan L., Helmick K., Schwab K., French L., Lu W.C. (2005). *War neurotrauma: The Defense and Veterans Brain Injury Center (DVBIC) experience at Walter Reed Army Medical Center (WRAMC)*. J. Neurotrauma 22, 1178.

Wightman J., Gladish S. (2001). *Explosions and blast injuries*. Ann Emerg Med. 37(6):664-78

Wood G., Panzer M., Shridharani J., Matthews K., Capehart B. et al. (2012). *Attenuation of blast overpressure behind ballistic protective vest*. Injury Prevention.

Yang K. (2001). *Review of mathematical human models for incorporation into vehicle safety design*, International Journal of Vehicle Design 26: 430–441.

Appendix A – The American Society of Mechanical Engineers (ASME) Design Process

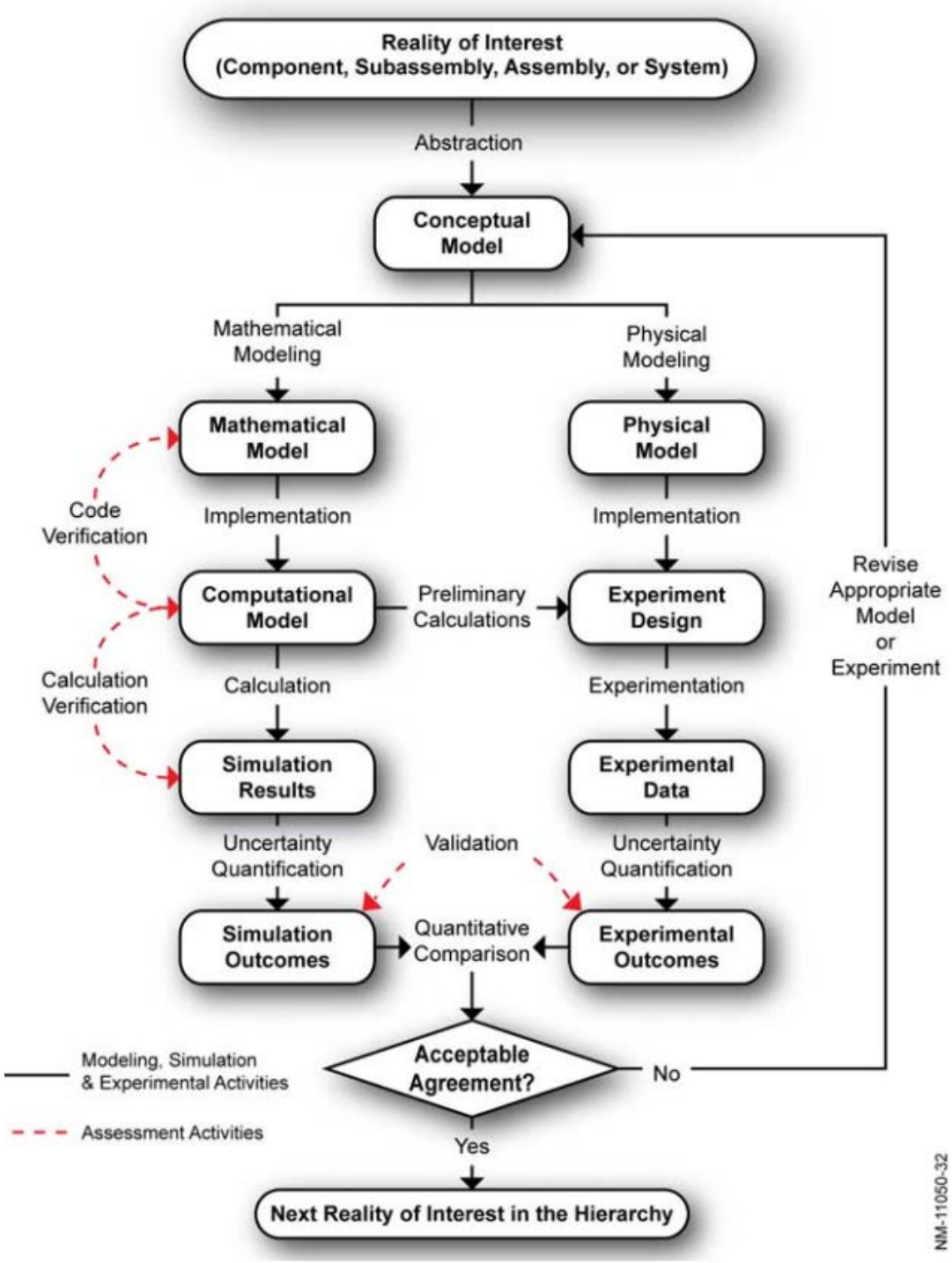

Figure A-0-1 – Verification and Validation activities and outcome [ASME, 2007].

Appendix B – Pressure Comparison 5 kg C4: 3.5 m, 4 m, 5 m Standoff

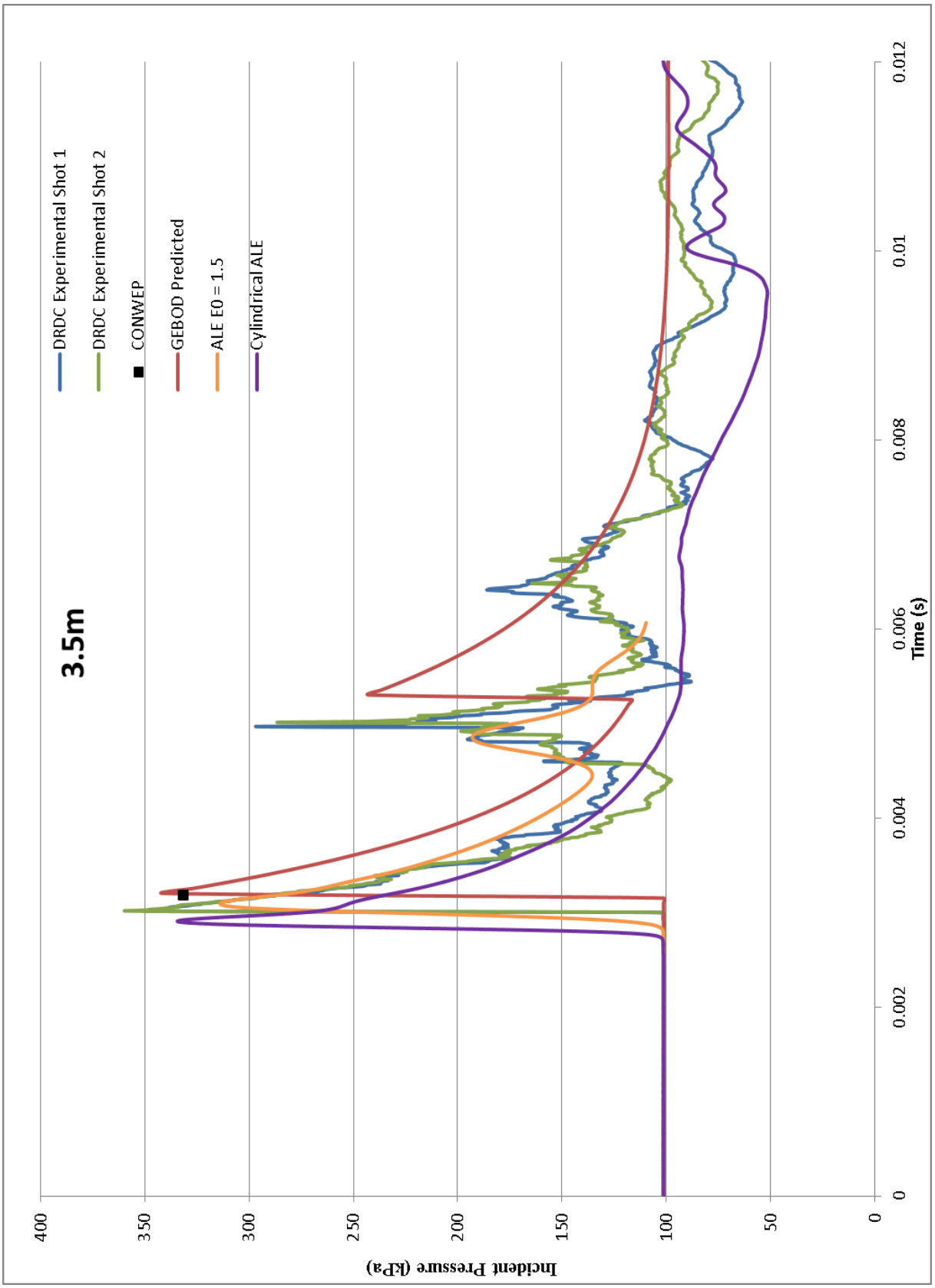

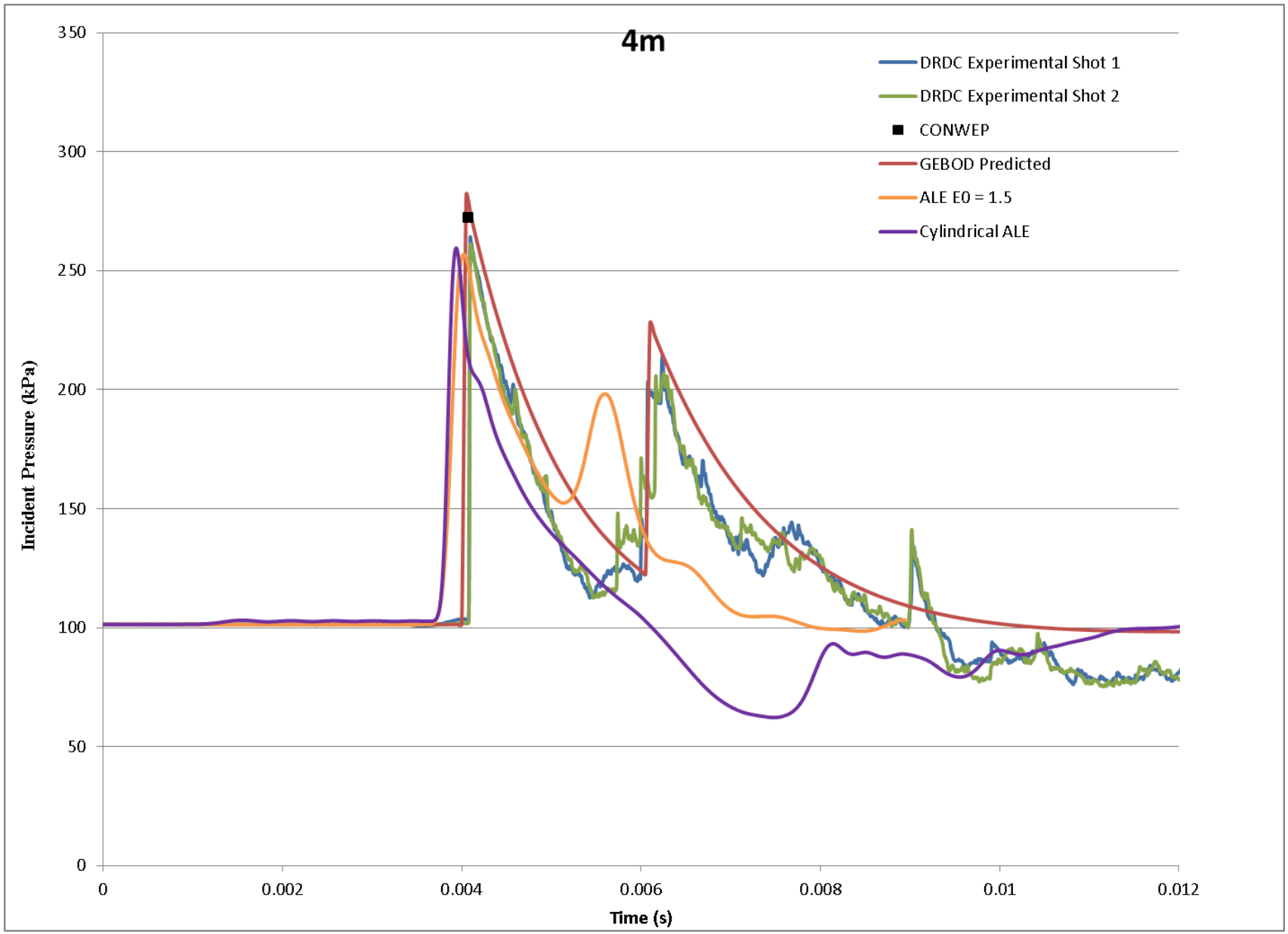
4m
DRDC Experimental Shot 1
DRDC Experimental Shot 2
CONWEP
GEBOD Predicted
ALE E0 = 1.5
Cylindrical ALE
Incident Pressure (kPa)
Time (s)
350
300
250
200
150
100
50
0
0
0.002
0.004
0.006
0.008
0.01
0.012

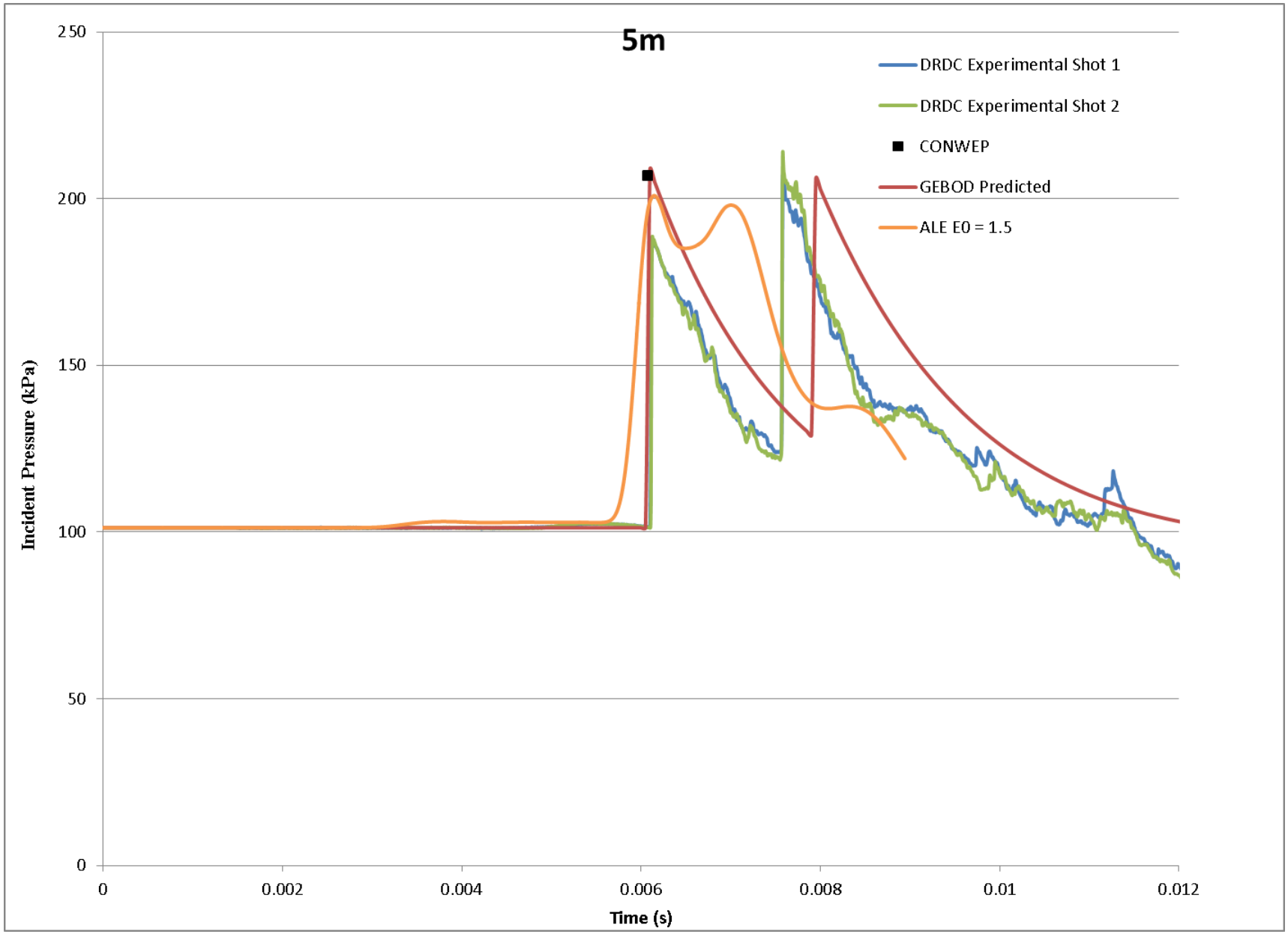
5m
DRDC Experimental Shot 1
DRDC Experimental Shot 2
CONWEP
GEBOD Predicted
ALE E0 = 1.5
Incident Pressure (kPa)
250
200
150
100
50
0
0
0.002
0.004
0.006
0.008
0.01
0.012
Time (s)